



Aramco
Journal
of Technology

FALL
20
19

page 2 /

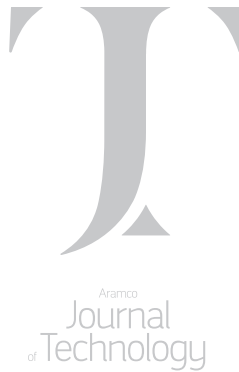
The Future of Nonmetallic Composite Materials in Upstream Applications

Wael O. Badeghaish, Dr. Mohamed N. Noui-Mehidi, and Oscar D. Salazar

page 33 /

Forward Integration of Dynamic Data into 3D Static Modeling Significantly Improves Reservoir Characterization

Babatope O. Kayode, Otto E. Meza Carmargo, Nerio Quintero Tudares, and Shaikha S. Al-Dossary



The *Aramco Journal of Technology* is published quarterly by the Saudi Arabian Oil Company, Dhahran, Saudi Arabia, to provide the company's scientific and engineering communities a forum for the exchange of ideas through the presentation of technical information aimed at advancing knowledge in the hydrocarbon industry.

Management

Amin Nasser

President & CEO, Saudi Aramco

Nabeel A. Al-Jama'

Vice President, Corporate Affairs

Fuad F. Al-Therman

General Manager, Public Affairs

Editorial Advisors

Ahmad O. Al-Khwaiter

Vice President, Technology Oversight and Coordination

Abdullah M. Al-Ghamdi

Vice President, Gas Operations

Abdul Hameed A. Al-Rushaid

Vice President, Drilling and Workover

Khalid A. Al Abdulgader

Chief Drilling Engineer

Khalid M. Al-Abdulqader

General Manager, Unconventional Resources

Omar S. Al-Husaini

General Manager, Drilling and Workover Operations

Jamil J. Al-Bagawi

Chief Engineer

Waleed A. Al Mulhim

Chief Petroleum Engineer

Ammar A. Al-Nahwi

Manager, Research and Development Center

Ashraf M. Al-Tahini

Manager, EXPEC ARC

Editor

William E. Bradshaw

william.bradshaw.1@aramco.com.sa

tel: +966-013-876-0498

Production Coordination

Richard E. Doughty

Design

Graphic Engine Design Studio

Austin, Texas, U.S.A.

No articles, including art and illustrations, in the *Aramco Journal of Technology* except those from copyrighted sources, may be reproduced or printed without the written permission of Saudi Aramco. Please submit requests for permission to reproduce items to the editor.

The *Aramco Journal of Technology* gratefully acknowledges the assistance, contribution and cooperation of numerous operating organizations throughout the company.

ISSN 1319-2388

© Copyright 2019 Aramco Services Company,
all rights reserved.

Contents

p. **2** **The Future of Nonmetallic Composite Materials in Upstream Applications**

Wael O. Badeghaish, Dr. Mohamed N. Noui-Mehidi, and Oscar D. Salazar

p. **13** **Improving Transport of Nanoparticles in Carbonate Media by pH Alteration**

Jesus M. Felix Servin and Hala A. AlSadeg

p. **19** **Efficient CO₂ Multistage Acid Stimulation in Deep Hot-Gas Reservoirs**

Dmitrii Gromakovskii, Maharaja Palanivel, Alfredo Lopez, and Vladimir Mikaelyan

p. **26** **Measuring Oil-Water Mixture Densities for Downhole Oil Field Operations Using Inclination Angle Method**

Dr. Chidirim E. Ejim and Dr. Jinjiang Xiao

p. **33** **Forward Integration of Dynamic Data into 3D Static Modeling Significantly Improves Reservoir Characterization**

Babatope O. Kayode, Otto E. Meza Carmargo, Nerio Quintero Tudares, and Shaikha S. Al-Dossary

p. **42** **In Situ Pore Plugging Using Nanosilica-based Fluid System for Gas Shut-off**

Prasad B. Karadkar, Dr. Ayman M. Al-Mohsin, Dr. Mohammed A. Bataweel, and Dr. Jin Huang

p. **52** **Integrated NMR Fluid Characterization Guides Stimulation in Tight Sand Reservoirs**

Endurance Oziegbe Ighodalo, Dr. Gabor G. Hursan, John McCrossan, and Ali R. Al-Balawi

p. **64** **Experimental Investigation into the Interactions between Three Types of Aqueous-based Fluids and Tight Organic-rich Carbonate Source Rocks**

Dr. Feng Liang, Jilin Zhang, Dr. Hui-Hai Liu, and Kirk M. Bartko

The Future of Nonmetallic Composite Materials in Upstream Applications

Wael O. Badeghaish, Dr. Mohamed N. Noui-Mehidi, and Oscar D. Salazar

Abstract /

Corrosion in oil and gas operations is generally caused by water, carbon dioxide (CO₂) and hydrogen sulfide (H₂S), and can be aggravated in downhole applications where high temperatures, combined with H₂S, introduce other challenges related to corrosion and iron sulfide scale formation. The repair costs from corrosion attacks are very high and associated failures affect on plant production rates and process integrity. To overcome this existing problem in upstream, nonmetallic composite materials were introduced for drilling, tubular, and completions in high risk, corrosive environments — the goal being to increase the well's life cycle and minimize the effect of corrosion, scale, and friction in carbon steel tubulars. The new proposed materials are lightweight, have high strength, and have superior fatigue resistance, in addition to an outstanding corrosion resistance, which is able to surpass many metallic materials.

The economic analysis shows that utilization of nonmetallic tubulars and linings will yield substantial life cycle cost savings per well, mainly due to the elimination of workover operations. Subsequently, with these advantages, composite materials pose several challenges such as single source provision, high initial cost of raw materials, the manufacturing process, and the limitation of nonmetallic standards.

As a result, the polymer and composite solutions for upstream oil and gas use are still very limited, even in targeting low risk applications such as low temperature and pressure scenarios. Therefore, research and development (R&D) efforts are ongoing to increase the operation envelope and introduce cost-effective raw materials for high-pressure, high temperature (HPHT) subsurface applications.

This article highlights practical examples of nonmetallic materials selection and qualification for upstream water injector/producer and hydrocarbon wells. Several future nonmetallic applications in upstream will be summarized. Challenges and R&D forward strategies are presented to expand the operation envelope of current materials and increase nonmetallic deployment to more complex wells, i.e., extended reach drilling.

Introduction

Carbon steel is the preferred material of choice for downhole applications. Carbon steel has distinct advantages over other materials in terms of material cost, temperature and pressure ratings, and field construction support services. One downside of a carbon steel flow line is a limited “lifetime” due to corrosion, but also includes repair cost, maintenance costs, and corrosion monitoring. The corrosion rate is also gradually increasing, which is attributed to the presence of hydrogen sulfide (H₂S), carbon dioxide (CO₂), and high cuts of highly saline waters. Corrosive fluids are generally handled by chemically inhibited carbon steel and corrosion resistant alloys (CRAs). The CRAs significantly increase the project cost and complexity. Currently, the oil and gas industry is considering different techniques to combat corrosion and one of these techniques is the utilization of nonmetallic products. The nonmetallic composite materials help to reduce capital and operational expenses without ignoring the safety, reliability, and long-term performance.

Nonmetallic composite materials have been widely used in onshore and offshore applications, including line pipe systems, flow lines, and topside applications (grates, ladders, and tanks). For instance, rigid reinforced thermosetting resin (RTR) pipes and reinforced thermoplastic pipes (RTP) were utilized for a number of years in a variety of onshore and offshore hydrocarbon service applications, and have proven to be successful to control corrosion and enhance the system reliability, Fig. 1¹.

The successful experience of the deployment of nonmetallic materials downstream in onshore and offshore applications has paved the way to increase the deployment in downhole applications. The main business drivers to increase the utilization of nonmetallic materials in upstream oil and gas applications, include¹:

- Reduce the cost of the well by using lower horsepower capacity drilling rigs.
- Improve well integrity through the utilization of noncorroding materials, and accordingly, increase the well's life cycle.

Fig. 1 Onshore field deployment of RTR (left), and RTP (right)¹.



- Reduce operational time and risk through the handling of lighter tubulars, and minimizing the potential lockup/buckling in downhole due to less friction.
- Promoting the conversion of oil to petrochemicals (boosting the feedstock for nonmetallic products would increase demand for oil).
- The fiber optic sensing can be easily embedded in the composite system and this will help to optimize the upstream operation by collecting downhole real-time data.

In fact, the deployment of nonmetallic materials upstream is strategic and aligns with industry trends. Subsequently, in upstream applications, specifically downhole environments, the conditions and standards applicable to the common flow line no longer applies. The material is subjected to a more complex set of dynamic stress conditions under variable multiphase fluids — internal and external — and temperatures. Several forces such as internal pressure (burst), external pressure (collapse), tension, and axial compression play a significant role in the nonmetallic downhole tubular performance.

These materials offer lightweight, high strength, superior fatigue resistance, and outstanding corrosion resistance that is able to surpass many metallic materials. In many cases of downhole deep well operations, the service tools are required to perform at a temperature of 150 °C to 232 °C, and under a pressure ranging from 5,000 psi to 15,000 psi — most of the time in a wet environment². As a result, the applications of nonmetallic composite downhole are still very limited, which requires an intensive research effort with service companies and academic.

Currently, the industry has explored the opportunity to deploy nonmetallic materials in upstream with low hanging fruit applications, and at the same time, working on research and development (R&D) supports the expanding operating envelope targeting high-pressure, high temperature (HPHT) applications. This application

is seen by the industry as significant and strategic for upstream operations.

Composite Materials and Design Selections

Composite materials are made from combining two or more materials, which provides the new material with unique properties, over and above the original materials. Nonmetallic composite materials are divided in two groups as fiber reinforced plastics and fiber reinforced resins. The matrix materials are classified into three categories: (1) thermoplastic, (2) thermosetting, and (3) elastomeric. A diverse array of reinforcements are used, which includes glass, carbon, and aramid. The fiber reinforcement has different grades, and it can be used as a tape or in the form of braided fibers. The role of the fiber is to carry the overall load and the role of the matrix is to transfer the stress within the fiber, and protect the system from mechanical damage.

The proper material selection of fiber and matrix for downhole completion equipment — essential in considering functional requirements, temperature, pressure, chemical and abrasion resistance — is key to a safe, reliable, fit-for-purpose and cost-effective operation over the design life of the well. In piping, the combination of these raw materials is used to make final composite products such as the RTR pipe and RTP, and the most recent technology use is the thermoplastic composite pipe (TCP).

Each composite has a different design and manufacturing process. The RTP structure is composed of three layers not fully bonded: (1) an inner layer that acts as a bladder and contains the process stream, (2) an intermediate layer that reinforces the pipe, and (3) an outer sheath that protects the pipe from wear, impact, and weathering effect. Figure 2³ shows the configuration of the RTP.

Fig. 2 The configuration of the RTP³.



Consequently, the TCP is made from three layers: (1) a liner, (2) a composite, and (3) a protective layer, forming a fully bonded solid wall pipe⁴. The TCP structure is made from either tape carbon or aramid fibers, which are designed for high-pressure applications. The TCP concept is increasingly gaining the attention of the oil and gas industry⁴. The RTR or fiberglass pipe is manufactured by a helical filament winding process. The fiber is embedded in an epoxy matrix and laid in an axial and hoop direction.

Depending on the applications and downhole conditions, fibers and polymer materials are defined, such as glass or carbon/aramid fibers and high performance engineering thermoplastic polymers such as polyphenylene sulfide (PPS), polyetheretherketone (PEEK), and polyvinylidene fluoride (PVDF) as a promising material for downhole applications. This is because of the superior properties of the semi-crystalline resin that has good chemical resistance at high operating temperatures². Table 1 shows key mechanical and physical properties for assessing the suitability of polymers and fibers for

downhole applications.

The selection of materials for downhole use, such as tubular, completion and drilling equipment, shall be evaluated based on international standards in line with the International Organization for Standardization and the National Association of Corrosion Engineers. This helps in selecting the proper nonmetallic materials for the downhole environment. In general, there are several key properties that need to be evaluated during material selection. These properties include:

- Compatibility with the service environment.
- Withstanding downhole stress (burst and collapse pressure).
- Thermal expansion.
- Tensile, strength, elongation at break, modulus of elasticity at minimum and maximum temperatures.
- Swelling and shrinking (mass and/or volume) by gas and by liquid absorption.
- Gas and liquid permeation.
- Resistance to gas decompression.
- Creep resistance at HPHT.
- Resistance to thermal cycling and dynamic movement.
- Chemical resistance to stimulation treatment.
- Erosion and abrasion resistance.

The numerical simulation is a very essential tool, which helps in selecting the proper materials, fiber orientations, and the thickness of composites, which suits certain applications. The simulation work is a key element to optimize the selections and decide the most economical solution based on the operating conditions.

Table 2 summarizes the proper fiber and matrix materials selection based on the different operating conditions and well service. A multilayer fiber needs to be considered in case of high pressure in downhole applications.

Future Nonmetallic Applications

Various composite applications, including drilling and completion, have been evaluated by actual field

Table 1 Key mechanical and physical properties for assessing the suitability of polymers and fibers for downhole applications.

Composite Materials	Name	Strength (MPa)	Young's Modulus (GPa)	Tg (°C)	Tm (°C)	Continuous use Temp (°C)
Fibers	Glass	1,800	70	—	—	—
	Carbon HS	3,200	230 – 350	—	—	—
	Carbon HM	2,500	> 400	—	—	—
	Aramid	3,000	65 – 130	—	—	—
Polymers	PEEK	80	—	143	334	190 – 210
	PPS	70 – 135	—	85 – 250	285	170
	PVDF	40 – 60	—	-60	170	150

Table 2 Proper selection of fiber and matrix composite materials for different operating conditions and well service.

Well Service	Downhole Conditions	Reinforcement	Matrix
Water	Low to Moderate Pressure and Temperature	Glass	Epoxy
Oil	Moderate to High Pressure and Temperature	Carbon, Aramid	Epoxy, PVDF, PPS
Gas	HPHT	Carbon, Aramid	PVDF, PPS, PEEK

deployment. These applications are still limited because of the materials' cost, and the limiting number of available industrial guidelines and standards supporting downhole applications. The existing applications of nonmetallic use downhole, such as a casing centralizer, drillpipe protector, and glass reinforced epoxy (GRE) liner, have been guided and deployed by engineering experience on a case-by-case basis. Figure 3 explains several downhole applications that have been replaced or are expected to be replaced over the next few years.

There are many future deployment opportunities to utilize nonmetallic composites as a cost-effective solution for upstream. Some of these technologies are at low technology readiness levels, which require more R&D efforts. Other materials need thorough technical evaluations to meet field proponent acceptance and make them feasible for downhole applications.

Currently, there is a well-developed process in the

industry to align nonmetallic deployment and development among different proponents, technical organizations, and R&D entities, to expand the operating envelope and resolve potential challenges based on field trials. The following are several promising upstream applications where the composite can be utilized and tested over the next few years, Fig. 4.

Nonmetallic Tubular

The full nonmetallic composite tubular (tubing/casing) and velocity string provide an alternative solution to the conventional carbon steel. It provides internal and external corrosion resistance when the tubular is exposed to a severe corrosive environment. Another advantage of composite is high ductility, and lighter weight — around six times — compared to steel tubular⁵. The use of the GRE tubular has increased significantly during the last few years in shallow water applications.

Currently available composites on the market are able

Fig. 3 Nonmetallic development roadmap for the current and future downhole applications.

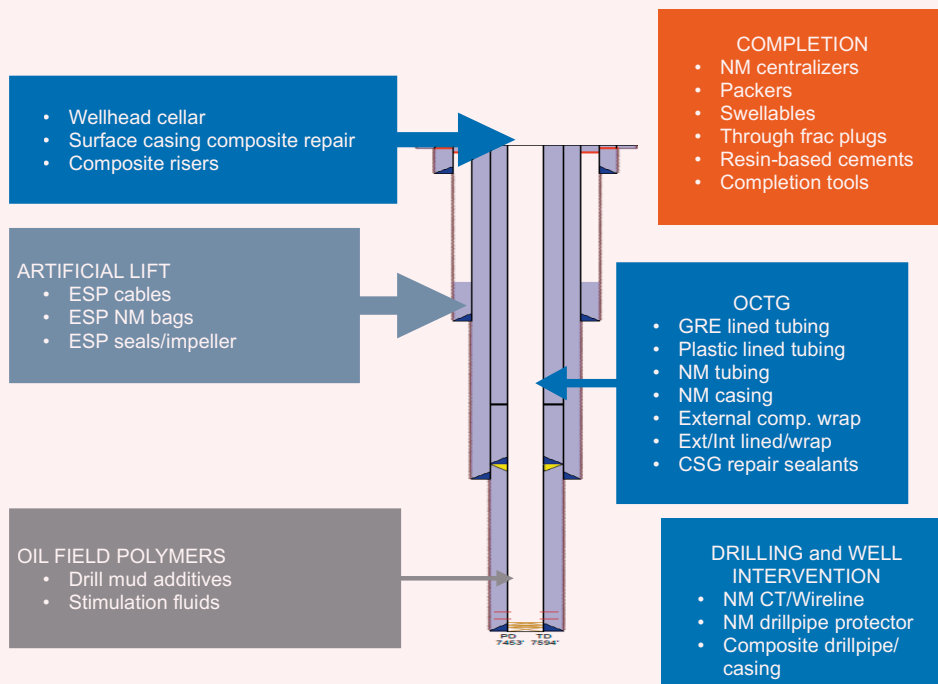
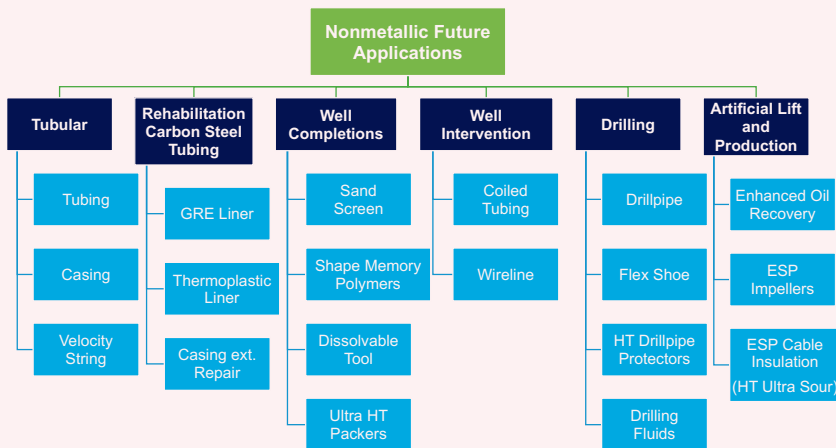


Fig. 4 A summary of the future potential applications of nonmetallic composites in downhole use.



to operate at a downhole temperature not exceeding 100 °C, however, research is underway to use composite materials for working temperatures from 150 °C to 170 °C in geothermal wells deeper than 3,500 m³. The industry has started to realize the high impact of expanding the operating envelope of current composite tubulars. In the future, the development of composite materials capable of operating in high borehole temperatures and/or pressure are being investigated to cover seawater injection, disposal, and supply, along with hydrocarbon wells. As a result, the complexity vs. time matrix is being developed to support the development plan promoting the composite utilization in upstream oil and gas operations, Fig. 5.

The selection of proper composite materials — fiber and matrix — and the understanding of downhole stress (burst, collapse, and tensile), are important factors to select the right composite tubular design that suits specific downhole conditions. In the case of tubing, composite

designs include flexible (RTP and TCP) and rigid (RTR), which are all currently under technical consideration. In the case of casing, designs considering a rigid composite (RTR), are under technical consideration as well. Based on the available composite design products in the market, Table 3 explains the optimal target requirements of pressure and temperature envelopes that need some extra effort from the industry to develop cost-effective composite solutions meeting the following downhole conditions.

Currently, the main industry focus is in water applications, including supply, injection, and disposal wells, since they present less associated risk and are cost-effective solutions compared to carbon steel. For instance, the full nonmetallic composite tubular composed of GRE, Fig. 6, has been tried worldwide in shallow water supply and observation wells⁶. The use of fiberglass casing in an observation well is becoming an area of interest, because

Fig. 5 Matrix development plan of composite tubulars.

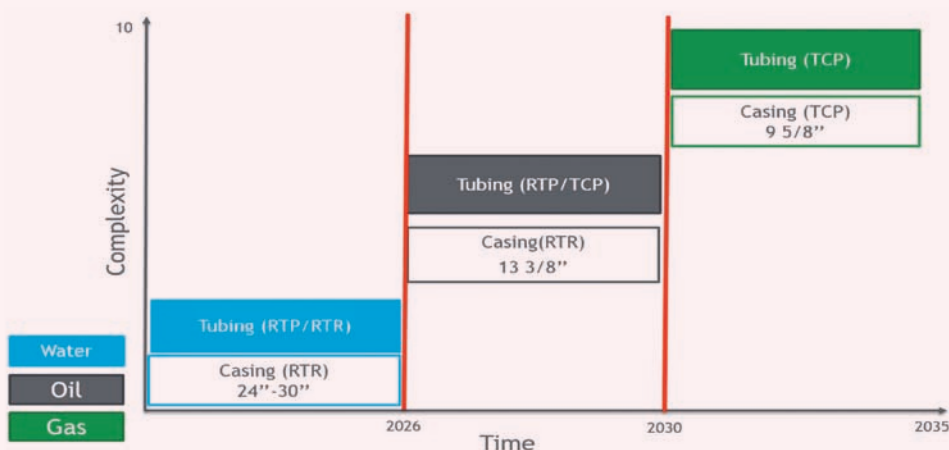


Table 3 Proposed R&D target requirement of nonmetallic composite tubular development.

Application	Casing			Tubing		
	Most Wells	Water	Oil	Gas		
Outside Diameter	30"	13³/₈"	9⁵/₈"	4¹/₂"	4¹/₂"	4¹/₂"
Burst pressure (psi)	2,000	4,000 to 7,000	12,000	4,000 to 5,000	7,000 to 10,000	10,000 to 15,000
Collapse pressure (psi)	1,500	2,500 to 6,500	11,000	4,000 to 5,000	7,000 to 10,000	10,000 to 15,000
Temperature (°F)	150 °F	260 °F	320 °F	200 °F	260 °F	320 °F

Fig. 6 Full RTR/GRE tubing design for a water supply well.



economic factors need to be evaluated as part of the feasibility studies.

As a result, the right decisions need to be made based on the following important factors:

- The life cycle of metallic pipes — frequent failure.
- Upgrading metallic materials (CRA) vs. composite cost.
- Workover cost.
- Production loss cost.
- Location, either offshore or onshore.

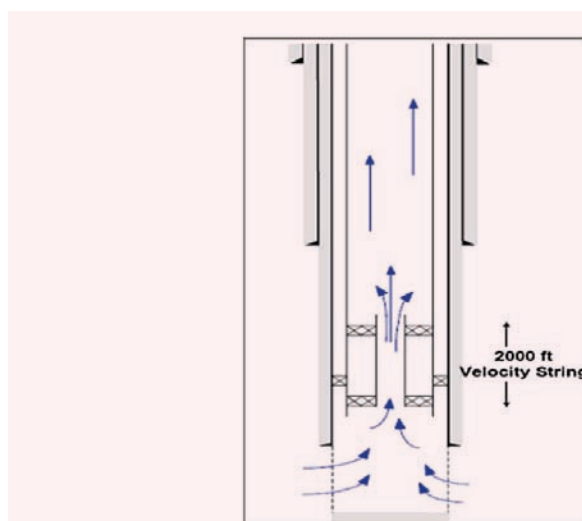
Besides the tubular, the velocity string is a low hanging fruit application to utilize the RTP or TCP composite design replacing a conventional steel string. Installing a velocity string reduces the flow area and increases the flow velocity to enable liquids to be carried from the wellbore. Velocity strings are commonly run using coiled tubing (CT) as production means. Figure 7 shows a schematic of this technique⁹. The industry has realized the high impact of the composite velocity string, due to its ability to run riglessly, the ease of installation and

it allows for the use of some deep induction open hole logging tools for measuring the changes in formation properties behind the casing⁷.

Enhancing the performance of current GRE casings and tubings above a rated pressure of 5,000 psi is feasible, by using high glass transition temperature point epoxies coupled with seamless manufacturing techniques, such as the rotational casting manufacturing process, strives to minimize composite body porosity and enhance the mechanical integrity at high temperatures. In fact, some manufacturers have developed prototypes that have been initially pilot tested⁸. On the other hand, one of the most challenging aspects is related to the leakage at the tube joints. Therefore, parallel research and validation should be done at the same time in this area.

The development of nonmetallic composite tubulars for oil and gas operations are quite challenging, due to the high initial costs of raw materials, special manufacturing processes, and the complexity of the downhole operating conditions. Therefore, several technical and

Fig. 7 A schematic of the velocity string equipment⁹.



the ability to eliminate the premature corrosion with metallic strings. The main target is to deploy the composite velocity string in the shallower vertical/deviated unconventional gas, oil, and water wells, and then the composite operating envelope will be improved, targeting extended reach applications.

Increasing the reliability of the nonmetallic composite tubular covering many applications in downhole is a significant milestone. To achieve this target, several associated challenges were identified that need to be addressed as part of the development plan. Those challenges are related to well completion and intervention operation, such as the packer setting, perforation, cementing, completion installation, and joint connection.

Thermoplastic Lined Carbon Steel Tubing

The internal lining technology with conventional GRE material has been widely used in the industry as a method for corrosion protection of downhole carbon steel tubing, Fig. 8. Thermoplastic liners or poly liners are another technology for downhole tubing products, which have presented a significant impact for reducing corrosion failures, with abrasive resistance in injection, disposal, and hydrocarbon wells. The thermoplastic liner is a thin layer of plastic, which is mechanically inserted inside new or used carbon steel tubing, and may offer a competitive advantage over CRAs in term of cost and life cycle. The cost savings were realized with fewer workovers and increased tubing life¹⁰.

There are four commercially available thermoplastic liner materials, and each has a limited temperature envelope of operating in wells up to 260 °C. For instance, the most commonly used thermoplastic liners in oil and gas production services are largely extruded from polyolefin for installation in environments up to 99 °C; yet, for more demanding environments, engineering thermoplastics such as PPS are available to handle temperatures as high as 175 °C. In the most extreme production environments with temperatures up to 260 °C, liners made of PEEK are utilized¹⁰. All of these plastic materials are

significantly more flexible with high impact resistance compared to traditional GRE liners. The installation process of those internal liner technologies should be done in the shop, as they cannot be done in the field. Therefore, an in situ lining system for downhole tubing is a most needed area of research to minimize the logistics and save operation time.

Downhole Completions

Most downhole completion systems were developed based on the use of metallics. For instance, metallic sand screen systems offer a simple and economic method for controlling sand. These systems have been subject to erosion/corrosion issues, and accordingly limit the life expectancy of the metallic screen. Therefore, ceramic sand screens were developed and proven to deliver high performance sand control in a variety of applications, Fig. 9¹¹. Consequently, the polymer composite sand screen is being investigated as an alternative, cost-effective, attractive technology to metallic and ceramic screens. For example, GRE sand screens are an attractive alternative to metallic screens. Although, they are still limited to low temperature wells — below 93 °C. Ongoing efforts are being made to expand the operation envelope of composite sand screen systems, by evaluating alternative advanced plastic materials that withstand high temperatures in oil and gas wells. This would be a breakthrough technology that can resist corrosion/erosion issues faced by conventional sand screens, and it will pave the way for other applications in downhole completion systems, such as inflow control devices and inflow control valves.

The dissolvable and drillable composite tools were designed to provide zonal isolation in the wellbore between multistage stimulation treatments. For instance, the composite frac plugs help to mitigate the risk during drill out, while decreasing time on location and costs to complete unconventional wells. These plugs provide faster mill times than a traditional plug. The R&D efforts are very promising in the area of dissolvable materials that can hold high pressures during the completion operations and retrieval operations².

The elastomer materials have found a niche downhole application in the form of seal elements. Typical elastomer downhole applications include blow out preventers, seals, packers, O-rings and seals for valves, and power sections for downhole motors. It is well-known that the popular use of elastomers in packers for well completion and zonal isolation sealing mechanisms perform a very critical function — either for short-term or long-term performance.

For example, swellable packer technology has been steadily gaining momentum. This technology relies on the physical swelling process characteristic of elastomers. The elastomer can be specifically formulated to achieve a controlled swelling when exposed to hydrocarbons, water, or a combination of both — hybrid swelling packers. The more demanding applications in ultra HPHT with very high H₂S and CO₂ levels are pushing the boundaries of elastomers. Although intensive research and development, as well as qualification, is moving in this area where a combination of elastomers like perfluoro elastomers and

Fig. 8 GRE lining of carbon steel production tubing.



Fig. 9 Ceramic sand screen design¹¹.



engineering plastics such as PEEK and polyamides are gaining momentum. More research is required to keep up with the demands of the ultra HPHT environment.

The utilization of composites in downhole completions is a most needed area of research through the joint efforts between academia, operators, and service companies to improve well integrity, and reduce the weight of the overall completion systems.

Well Intervention Tools

Conventional well intervention tools, such as steel CT and wirelines, have shown several issues with pitting corrosion¹². In addition, they are being subjected to high friction within the formation, which limits the ability of the CT to reach down to the target depth. To address potential premature failures, a composite CT was recently introduced in the well intervention business as a

low fatigue and corrosion resistant alternative to steel CT, however, due to the inherent limitation of material properties and the product's capabilities to comply with an extended reach requirement, applications of the basic design of composite CT were not found successful. As a result, with the advent of new composite design materials, the CT based on thermoplastic composites are still under development¹³.

The spoolable composite CT may have a structure similar to a TCP with a well bonded structure, or a RTP with an unbonded structure. In these new structure designs, carbon and aramid fiber reinforcement were used in a multilayer configuration that optimized the axial performance and fatigue life of the material, while keeping spoolability and use in a horizontal extended reach well feasible.

On the other hand, the composite wireline is also under proof of concept studies, to replace conventional metallic lines. This would be a breakthrough technology in the oil and gas industry. Although, the initial cost of thermoplastic composite well intervention technology is high, there are many advantages that may help in the reduction of the operational cost by increasing resistance to corrosion, ease of handling in a severe dogleg, providing less friction, it is lightweight, and has better mechanical properties.

Casing Flex Shoe

A composite flexible shoe can be a good solution when running casing with a high build rate and inclination, to minimize the risk of getting stuck off bottom, Fig. 10¹⁴. The flexible casing shoe reduces the side loads at the bottom of the drill string when running into the hole. Due to the flexibility of nonmetallic composites, as compared to steel, it minimizes the high loads resulting from the inherent stiffness of the metallic casing, as it is bent through doglegs downhole.

The product provides many advantages in tackling wellbore challenges, including:

- The ability to guide large diameter casings with inclinations above 40°.
- Use with any size casing when running through severe doglegs.

Fig. 10 Composite casing flex shoe¹⁴.



- Use with deep-water wells, which require the use of stiff, large diameter casings.
- Use in extended reach drilling or horizontal wells to prevent buckling or hanging up casing in the build and lateral sections, to increase run efficiency.

Impeller Pump

A conventional metallic impeller/diffuser for downhole electric submersible pumps (ESP) is subjected to frequent failure due to high corrosive environments. For ESP impellers in oil and gas applications, particle erosion/corrosion is the main cause of the component failures in the process lines. Engineered composite pumps have proven to outlast metallic parts by many years, because composite pumps better resist cavitation, and they are not subject to corrosion or electrolysis attack. Composite pumps have become a solution for longer pump life, Fig. 11¹⁵.

The structure of composite pump materials includes graphite composite made of 3D graphite interwoven fibers with a hybrid phenolic resin system. The composite impeller pumps are capable of continuous operation at 150 °C, and have excellent mechanical properties and chemical resistance¹⁵. Currently, there is a business need in deploying this technology to resolve the premature erosion/corrosion effects. As result, a feasibility study is in process to ensure that the full composite impeller is a reliable technology, able to withstand downhole well conditions.

Shape Memory Polymer (SMP)

The shape memory polymer (SMP) is a smart material that changes its properties in response to external stimulus. There are different triggering mechanisms that the SMP responds to, such as temperature and chemical reactions. For instance, the SMP polyurethane (SMPU) foam has several potential applications in downhole zonal isolations, including water shut off for downhole fracture operations.

The activation of the SMP expansion occurs if the surrounding temperature is higher than the high glass transition temperature of the SMP. Otherwise, no activation

occurs. Recently, the SMPU has been used as a reactive sand control media to control the sand in open hole applications, replacing the conventional open hole gravel packing. The SMP was designed to be run in the hole as part of the completion in a compressed state with an outer diameter smaller than that of the wellbore when activated. The SMP material then expands and fills the entire annulus, applying residual stress to the sandface while acting as a filtration medium¹⁶. This application has proven the effectiveness of SMP foam to eliminate the concerns of plugging and erosion associated with a stand-alone screen¹⁶. The sand management was selected as an initial application, which will pave the way for several applications for SMPs in downhole use.

Path Forward

Nonmetallic composites have many advantages in terms of corrosion resistance and extension of the well's life cycle; however, the high initial cost and limitation of technical skills present substantial challenges. The worldwide oil industry has observed the business need for allocating the necessary investment needed in R&D to support utilizing nonmetallics in downhole applications. Otherwise, the investment and localization of nonmetallics are other important pillars that would help to reduce the initial cost and improve local technical skills. The path forward is clearly articulated around the role of the end user, R&D entities, and service companies to serve the industry. The following are some initiatives toward optimizing nonmetallic composite expertise in downhole applications:

- Support for the R&D is needed to replace the conventional tubing/casing with nonmetallic composite materials in water application wells, which includes supply, disposal, injection, and observation wells.
- Expand the operating envelope of current composite materials.
- Explore organic and natural materials that would help reduce the cost of the carbon fiber.
- Optimize the cost of composite raw material and the manufacturing process.
- Introduce 3D printing technology in the composite manufacturing process.
- Develop a nondestructive evaluation for online inspection of the composite structure and induced defects.
- Study the mechanical behavior of composites and material degradation based on high temperature and loading/deformation.
- Develop the numerical models supporting composite material selection and life prediction based on downhole conditions.
- Develop nonmetallic standards supporting downhole applications.
- Expand the applications of spoolable composites, i.e., RTP concept, to be used for downhole tubing.
- Explore alternative applications beyond tubulars, including completion, well intervention, and ESP applications.

Fig. 11 Nonmetallic composite pump impeller¹⁵.



- Address different associated challenges related to packer setting, cementing, perforation, and completion installation with full nonmetallic tubulars.
- Support the research and validation of new materials for swellable packers in ultra-HPHT wells.
- Develop a reliable threaded connection for metal composite joints that withstand high pressures.
- Develop smart materials such as SMP for downhole zonal isolations.
- Support the localization and an investment plan in the composite business.
- Develop the intelligent composite tubing, where fiber optic sensing and the power cable can be embedded for downhole real-time measurements.

Conclusions

Nonmetallic composite-based materials have been introduced in oil and gas applications, including onshore, offshore, and downhole. As clearly stated in this article, the deployment of nonmetallic materials in downhole applications has allowed us to overcome corrosion challenges, minimize frequent workover, and extend the life cycle of critical downhole products, including tubular, drilling, and well completions. As a result, much effort by the industry has placed a heavy emphasis on robust deployment and development methodologies in alignment with the field application trends to qualify cost-effective composite materials covering many downhole applications.

The path forward, which already started in R&D, is focused toward improving the composite business to serve the oil and gas industry. This involves the development of specific roadmaps for different products to accelerate the mass deployment, support localization and investment in research studies. This effort requires joint work with different entities that sets the basis for increasing the deployment of cost-effective materials for more demanding HPHT applications.

Acknowledgments

The authors would like to thank the management of Saudi Aramco for their support and permission to publish this article.

This article has been accepted for presentation at the Gas and Oil Technology Showcase and Conference, Abu Dhabi, UAE, October 21-23, 2019.

References

1. Parvez, M.A., Asiri, A.Y., Badghaish, A., Al-Dossary, A.K., et al.: "Saudi Aramco Details Nonmetallic Products Deployment in Oil, Gas," *Oil & Gas Journal*, Vol. 116, Issue 1, January 2018, pp. 51-60.
2. Yuan, Y. and Goodson, J.E.: "Advanced Composite Downhole Applications and HPHT Environmental Challenges," NACE paper 04616, presented at the CORROSION 2004 Conference and Exhibition, New Orleans, Louisiana, March 28-April 1, 2004.
3. Conley, J., Weller, B. and Slingerland, E.: "The Use of Reinforced Thermoplastic Pipe in Oil and Gas Gathering and Produced Water Pipelines," SPE paper 113718, presented at the CIPC/SPE Gas Technology Symposium Joint Conference, Calgary, Alberta, Canada, June 16-19, 2008.
4. Wilkins, J.: "Qualification of Composite Pipe," *Journal of Petroleum Technology*, Vol. 68, Issue 12, November 2016.
5. Kruszewski, M.: "The Potential Application of Composite Pipes in Geothermal Drilling," GEOENERGY Marketing Services, February 2019, retrieved from <https://www.geoenergymarketing.com/energy-blog/the-potential-application-of-composite-pipes-in-geothermal-drilling/>.
6. Amani, M.K. and AbdulRauf, A.: "An Update on the Use of Fiberglass Casing and Tubing in Oil and Gas Wells," *International Journal of Petroleum and Petrochemical Engineering*, Vol. 3, Issue 4, 2017, pp. 43-53.
7. Al-Oqab, M., Kaushik, P., Ahmad, A.T. and Kumar, S.: "Fiber Glass Casing Design, Planning and Installation Experience in Observation Wells," SPE paper 189430, presented at the SPE/IADC Middle East Drilling Technology Conference and Exhibition, Abu Dhabi, UAE, January 29-31, 2018.
8. Akiet: "Downhole Composite Tubulars," retrieved from <https://akiet.com/industry/oil-gas-industry/>, 2017.
9. Khamehchi, E., Khishvand, M. and Abdolhosseini, H.: "A Case Study to Optimum Selection of Deliquification Method for Gas Condensate Well Design: South Pars Gas Field," *Ain Shams Engineering Journal*, Vol. 7, Issue 2, June 2016, pp. 847-853.
10. Western Falcon: "Successful Oil and Gas Production Well Applications of Thermoplastic Lined Downhole Tubing: A Compilation of Case Histories Dating Back to 1996," retrieved from <https://westernfalcon.com/paper-production/>, 2019.
11. Sidek, S., Lian, K.G.H., Ching, Y.B., Trjanganung, K., et al.: "First Successful Application of Ceramic Sand Screen in Maturing Oil Field, Offshore East Malaysia," SPE paper 188537, presented at the Abu Dhabi International Petroleum Exhibition and Conference, Abu Dhabi, UAE, November 13-16, 2017.
12. Van Arnam, W.D., McCoy, T., Cassidy, J. and Rosine, R.: "The Effect of Corrosion in Coiled Tubing and Its Prevention," SPE paper 60744, presented at the SPE/ICoTA Coiled Tubing Roundtable, Houston, Texas, April 5-6, 2000.
13. Sas-Jaworsky, A. and Williams, J.G.: "Development of Composite Coiled Tubing for Oil Field Services," SPE paper 26536, presented at the SPE Annual Technical Conference and Exhibition, Houston, Texas, October 3-6, 1993.
14. WWT International: "WWT FlexShoe™," retrieved from <https://www.wwtco.com/products/performance-casing-flex-guide-shoes/wwt-flexshoe>, 2019.
15. SIMSITE: "Simsite Impeller and Rings," retrieved from <https://www.simsite.com/impellers-rings>, 2017.
16. Wang, X. and Osunjaye, G.: "Advancement in Open Hole Sand Control Applications Using Shape Memory Polymer," SPE paper 181361, presented at the SPE Annual Technical Conference and Exhibition, Dubai, UAE, September 26-28, 2016.

About the Authors

Wael O. Badeghaish

M.S. in Materials Science Engineering and in Project Management, Catholic University of America

Wael O. Badeghaish is a Petroleum Scientist working with the Production Technology Team of Saudi Aramco's Exploration and Petroleum Engineering Center – Advanced Research Center (EXPEC ARC). He joined Saudi Aramco in early 2015 after previously working for the Sabic Plastic Application Development Center in Riyadh. Wael's work experience has mainly been in the area of well completion and intervention. Recently, he has been working to support the research and development of nonmetallic composites in

downhole applications.

Wael is a member of Society of Petroleum Engineers (SPE) and National Association of Corrosion Engineers (NACE).

In 2009, he received his B.S. degree in Electrical Engineering from King Fahd University of Petroleum and Minerals (KFUPM), Dhahran, Saudi Arabia. In 2014, Wael received his M.S. degree in Materials Science Engineering and in Project Management from the Catholic University of America, Washington, D.C.

Dr. Mohamed N. Noui-Mehidi

Ph.D. in Resource & Energy Science, University of Kobe

Dr. Mohamed N. Noui-Mehidi is Senior Petroleum Engineer Consultant at Saudi Aramco's Exploration and Petroleum Engineering Center – Advanced Research Center (EXPEC ARC). He is the Advanced Well Systems focus area champion for the Production Technology Team. Mohamed joined Saudi Aramco in late 2008 after previously working for the Commonwealth Scientific and Industrial Research Organization, Australia. He has more than 29 years of experience in the area of multiphase flow dynamics, flow metering, and flow modeling.

Mohamed's research activities are in the development of new technologies in well control and monitoring for upstream oil and gas production, well intervention tools, and flow sensors. He has published more than 100 journal articles and conference papers on the different aspects of fundamental and applied fluid dynamics as well as authored 39 company granted patents and several patent applications.

Mohamed received his Ph.D. degree in Resource & Energy Science from the University of Kobe, Kobe, Japan.

Oscar D. Salazar

M.S. degree in Polymer Science, University of Akron

Oscar D. Salazar is a Nonmetallic Engineering Specialist working in the Nonmetallic Engineering Division of Saudi Aramco's Consulting Services Department. Prior to joining Saudi Aramco, he worked in Weatherford International where he was in charge of research, product development, and lab qualification of nonmetallic materials for downhole applications, including composites, elastomers, and coatings. Oscar also worked as an independent consultant in nonmetallic materials in several projects for Total and

Conoco.

His work experience extends to 25 years in nonmetallic and coatings, covering a broad spectrum of activities such as design of experiments, failure analysis, development of engineering standards, materials selection and research and development.

Oscar received his M.S. degree in Polymer Science from the University of Akron, Akron, Ohio. In addition, he has academic experience in root cause analysis through courses at the university level.

Improving Transport of Nanoparticles in Carbonate Media by pH Alteration

Jesus M. Felix Servin and Hala A. AlSadeg

Abstract /

Improving long-term stability and reducing retention are active areas of research for nanoparticle-based technologies for the oil and gas industry. A common strategy to improve nanoparticle stability and reduce retention is the use of polymer and/or surfactant coatings. This manuscript describes a method to improve the transport properties of fluorescein isothiocyanate dextran (FITC-dextran) through carbonate media. The proposed method is based on the observation that during alkaline-polymer-surfactant flooding, polymer retention reduces as pH increases, likely as a consequence of transitioning through the point of zero charge for the porous media. Multiple alkali agents have been identified in the past, but most of them are incompatible with brines containing a high concentration of divalent cations, such as calcium (Ca^{2+}) and magnesium (Mg^{2+}), and are therefore incompatible with carbonate reservoirs. Sodium metaborate (BNaO_2), however, has been reported as being compatible with hard brines and carbonate reservoirs. This study evaluates the effectiveness of BNaO_2 as an alkali agent to reduce FITC-dextran retention through carbonate matrices as a proxy for dextran coated nanoparticles.

A series of transport experiments were conducted using chromatography columns packed with fine marble powder to evaluate the impact of pH on FITC-dextran retention. The columns were initially saturated with treated saline water and let rest for three weeks followed by the injection of three pore volumes (PVs) of treated saline water for washing purposes. Next, 5 PVs of a solution of FITC-dextran dissolved in treated saline water (with or without sodium metaborate tetrahydrate (BH_8NaO_6)) was injected through the columns. Finally, 5 PVs of treated saline water (with or without BH_8NaO_6) were used to displace the injectant. Effluent samples were collected during each phase of the experiment and analyzed using a fluorescent spectrometer. Fluorescence intensity data was converted to concentration and plotted as a function of injected volume to create a breakthrough curve and to estimate FITC-dextran recovery.

The results show a slight decrease in retention when using BNaO_2 to increase the solution's pH. FITC-dextran recovery was estimated to be 47% for the injectant without BH_8NaO_6 , and 49% for the injectant with it. This trend is in agreement with previous studies looking at polymer retention and FITC-dextran retention. The experiments suggest that pH plays a significant role during the flushing phase.

The ability to transport nanoparticles through oil reservoirs can lead to a whole new range of applications, including smart tracers, contrast agents and improved enhanced oil recovery (EOR) agents, along with other technologies for reservoir characterization.

Introduction

Nanoparticles with novel biochemical, catalytic, mechanical, and optical properties have contributed significantly to technological advances in many industries. Aside from their renowned uses in the fields of drug delivery¹, coatings², and electronics³, nanomaterials are also investigated for many applications in the oil and gas industry, including enhanced oil recovery (EOR), corrosion inhibition, water control, and improved reservoir monitoring⁴⁻⁷. Long-term stability, mobility and retention are active areas of research associated with these upstream applications because the nanoparticles are required to travel long distances within porous media, without generating aggregates, to a desired reservoir zone. The use of polymer and/or surfactant coatings is a common strategy to improve stability, to reduce retention and to provide functionality. Many different nanoparticle coatings have been described in the literature, and some stable nanoparticles have been reported and are commercially available⁸⁻¹⁰. Consequently, even if long-term stability is achieved, accomplishing long distance propagation within the reservoir is a requirement that must be met for reservoir applications.

It has been shown that nanoparticle retention in oil reservoirs occurs mainly in the form of adsorption to the rock grains. The classical DLVO theory is the most common theory used to explain particle attachment to the rock surface. It assumes that the rock nanoparticle interactions are controlled by the sum of two forces: the London-van der Waals and the electrostatic double layer. The first one arises due to the electromagnetic effects of the molecules in the nanoparticles and/or rock surface, while the second one is the result of the overlap of the double layer of

each nanoparticle and the rock surface. Subsequently, it is now clear that additional forces exist, including elastic-steric repulsion, bridging attraction, osmotic repulsion, hydrophobic force, and magnetic attraction. To be able to propagate deep in the reservoir, the attractive forces must be countered, resulting in a net repulsive force. Studies showed that at high salinity, limestone rocks exhibit greater nanoparticle retention when compared to sandstone and dolomite counterparts¹¹.

The challenge of retention is not exclusive to nanoparticles, and is also faced in surfactant and polymer flooding operations. It has been shown that increasing the pH lowers surfactant adsorption in sandstone and carbonate reservoirs¹²⁻¹⁴ — a technique known as alkaline-surfactant-polymer flooding. This is due to the fact that at typical reservoir conditions, rock surfaces have a positive charge, whereas most oil field surfactants are negatively charged; the polar charges trigger an electrostatic attraction that hinders the propagation of injected material in the reservoir. By altering the pH using alkali agents, the positive surface charge of the rock transitions through a point of zero charge and becomes negative afterwards¹². Once the surface charge is negative, the surfactant does not readily attach to the rock surface. Multiple alkalis have been tested, including sodium carbonate, sodium hydroxide and sodium metaborate (BNaO_2). The first two are intolerant to high divalent cation concentrations, such as calcium (Ca^{2+}) and magnesium (Mg^{2+}), and are therefore incompatible with carbonate reservoirs. BNaO_2 has been proposed as an alternative alkali for such reservoirs¹³⁻¹⁵.

Polysaccharides, such as dextran, are compounds chemically similar to polymer surfactants used for EOR and have been considered as a potential nanoparticle coating to improve long-term stability, and transport properties. Due to its chemical similarity to polymer surfactants, it is hypothesized that increasing the pH should reduce retention of dextran coated nanoparticles. A fluorescently labeled version of dextran, fluorescein isothiocyanate dextran (FITC-dextran), is commercially available, allowing for retention quantification through fluorescence spectroscopy.

This study investigates the effect of BNaO_2 as an alkali agent on the transport of FITC-dextran through carbonate matrices. It is assumed that FITC has no impact on the transport properties of dextran, and that the behavior of FITC-dextran will be similar to that of dextran coated nanoparticles.

Experimental Materials and Methods

Materials

Porous Medium. Fine marble powder was used to pack three chromatography columns made of borosilicate glass, each measuring 1 cm in diameter and 30 cm in length, for a total volume of 23.6 ml. The porosity of each column was approximately 42% (control experiment), 42% (injectant 1 experiment) and 34% (injectant 2 experiment). The ends of the columns were fitted with 20 μm porosity high-density polyethylene (HDPE) bed supports to prevent migration of the marble powder. A

1/16" outer diameter fluorinated ethylene propylene polytetrafluoroethylene tubing was used for the inlet and outlet.

Polysaccharide. FITC-dextran ($M_w = 10,000$ Da), manufactured by Tokyo Chemical Industry, was used for both injectant 1 and 2. The excitation maximum is at 490 nm and the emission maximum is at 520 nm, as per the manufacturer.

Alkali agent. Extra pure sodium metaborate tetrahydrate (BH_8NaO_6) ($M_w = 137.86$ g/mol) manufactured by Acros Organics was used as an alkali agent to increase the pH of injectant 2.

Injectant 1. A solution of 1 mg/l of FITC-dextran dissolved in treated saline water (~56,000 ppm total dissolved solids (TDS)). The pH of the solution was 7.3.

Injectant 2. A solution of 1 g/l BH_8NaO_6 and 1 mg/l of FITC-dextran dissolved in treated saline water (~56,000 ppm TDS). The pH of the solution was 9.1.

Column Experiments for Transport Study

Experimental setup. The transport experiments were conducted using a 60 ml plastic syringe mounted on a syringe pump, a packed column and a manual fraction collector. For each experiment, the column was initially saturated with treated saline water and let rest for three weeks. Next, three pore volumes (PVs) of treated saline water were pumped through the column at a rate of 0.5 ml/min for washing purposes.

Previous experiments using similar marble powder have shown that the washing phase is important to remove fluorescent components from the column¹⁴. Samples of the effluents were manually collected at each 0.2 PV during the washing phase. Then, 5 PVs of injectant 1 or 2 were flowed at 0.5 ml/min. Samples of the effluents were manually collected for the first PV at every 0.05 PV and every 0.1 PV for the remaining 4 PVs. Finally, the injectant was pushed with 5 PVs of treated saline water (for injectant 1 experiment) or treated saline water with 1 g/l of BH_8NaO_6 (for injectant 2 experiment) at a rate of 0.5 ml/min. A total of 20 samples of the effluents were collected for the first PV, and 10 samples per PV for the remaining 4 PVs. The experiments were performed at room temperature and atmospheric pressure.

Fluorescence spectrometer. A multi-mode microplate reader was used to measure fluorescence intensity of the effluents. The samples were excited at 490 nm — excitation maximum for the FITC — and emission intensity at 520 nm — emission maximum for the FITC — was measured using the endpoint mode of the device, which is suitable for quantitative sample comparison.

Calibration curves. To convert the fluorescence intensity to a FITC-dextran concentration, calibration curves were developed for both injectants. A total of eight different FITC-dextran concentrations were used to create each curve. The samples were analyzed using a microplate reader with an excitation wavelength of 490 nm, and the fluorescence emission at 520 nm was measured. The results were plotted and a linear trendline was fitted for each data set, Figs. 1 and 2.

Fig. 1 Fluorescence intensity calibration curve for injectant 1.

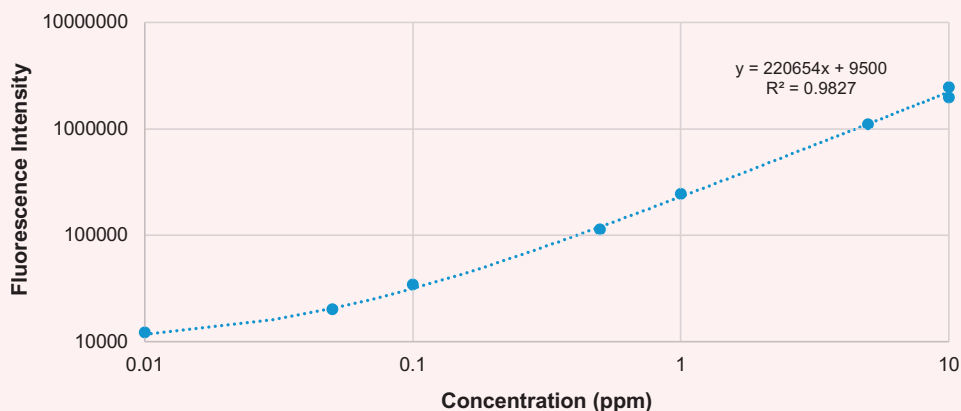
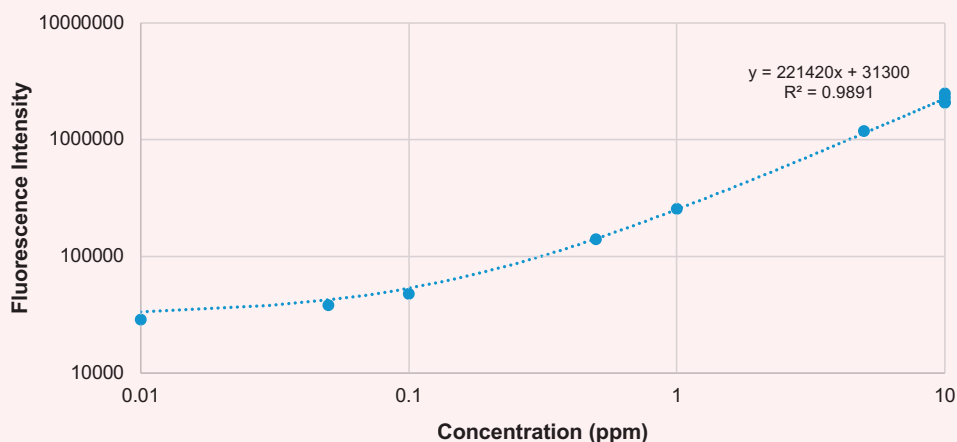


Fig. 2 Fluorescence intensity calibration curve for injectant 2.



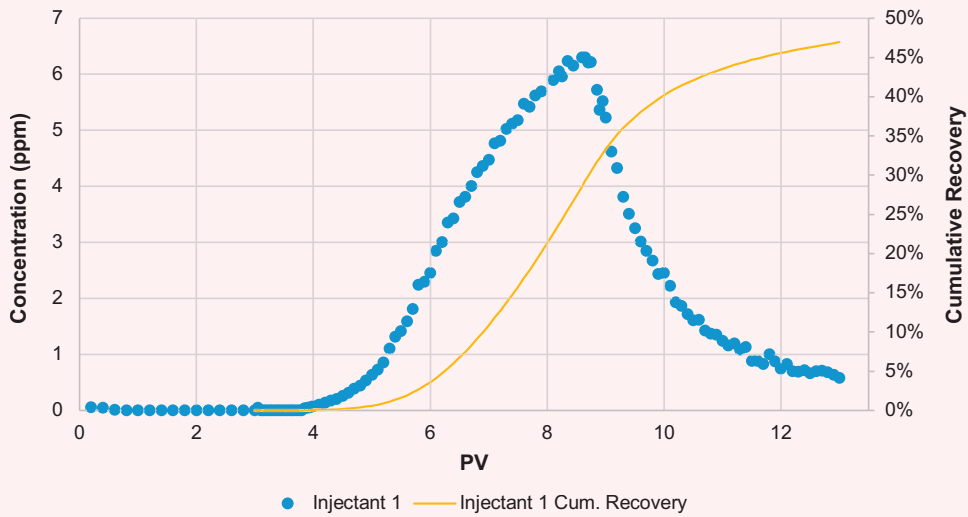
Control experiment. A total of 13 PVs of treated saline water were pumped through a column at a rate of 0.5 ml/min. Samples of the effluents were collected every 0.25 PV. A decrease in fluorescence is observed during the washing phase. This is consistent with previous experiments using marble powder and suggest that some components of the marble powder are fluorescent when excited at 490 nm. The background fluorescence stops changing after 3 PVs of injected saline water.

Injectant 1 experiment. The column was initially washed with 3 PVs of treated saline water at a rate of 0.5 ml/min. A total of 15 effluent samples were collected during the washing phase. Next, 5 PVs of injectant 1 were pumped through the column at the same rate, and a total of 60 effluent samples were collected. Finally, injectant 1 was displaced with 5 PVs of treated saline water injected at 0.5 ml/min, and 60 effluent samples were collected.

The samples were analyzed with a fluorescence

spectrometer. The fluorescence intensity was converted to concentration using the relationship found through the calibration curve for injectant 1. The concentration, as a function of volume injected, was plotted to create a breakthrough curve, Fig. 3. The results show that FITC-dextran breakthrough occurs approximately after injecting 0.75 PVs of injectant 1. The delay is probably caused by dispersion and dextran interaction with the rock surface resulting in reversible retention. The maximum concentration — 63% of injectant 1 — is observed after 0.65 PVs of treated saline water have been injected to displace injectant 1. FITC-dextran recovery after the injection of 5 PVs of treated saline water was estimated at 47% by calculating the integral of the breakthrough curve. The effect of reversible retention is clearly observed during the flushing phase, resulting in a delayed reduction of the fluorescence intensity of the effluents. The concentration equilibrium was not achieved during this experiment, and therefore, the adsorption

Fig. 3 Breakthrough curve and cumulative recovery for injectant 1.

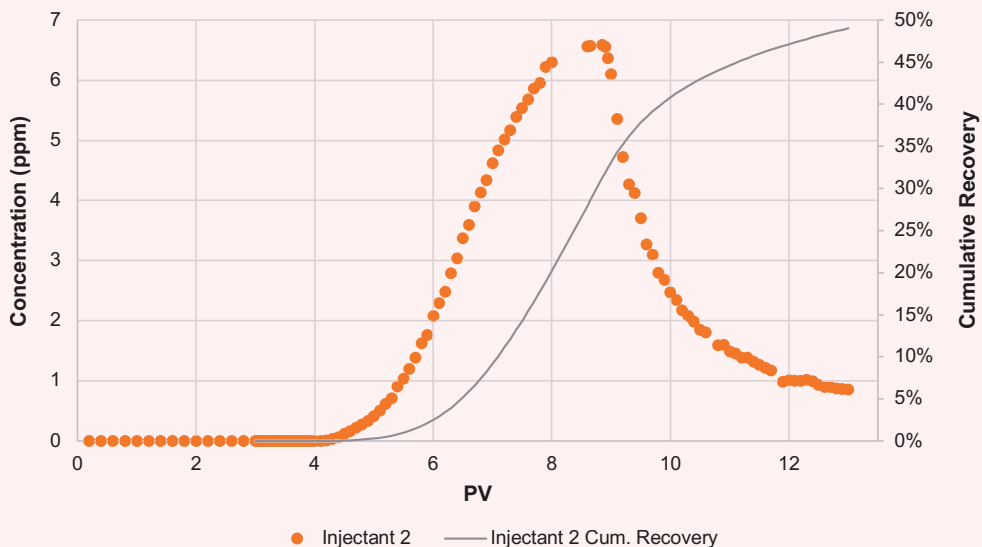


capacity of the marble powder was not calculated.

Injectant 2 experiment. The column was washed by flowing 3 PVs of treated saline water at a rate of 0.5 ml/min. A sample of the effluents was collected at every 0.2 PV. Washing was followed by the injection of 5 PVs of injectant 2 pumped at the same rate. A total of 20 effluent samples were collected for the first PV, and 10 samples for each of the remaining 4 PVs. Injectant 2 was flushed with 5 PVs of a solution of 1 g/l BH_3NaO_6 dissolved in treated saline water injected at 0.5 ml/min, and 60 effluent samples were collected.

The fluorescence intensity of the samples was measured and converted to a FITC-dextran concentration using the calibration curve developed for injectant 2. The fluorescence intensity data was converted to a concentration and plotted as a function of injected volume to create a breakthrough curve, Fig. 4. FITC-dextran breakthrough occurs after flowing approximately 1.1 PVs of injectant 2. As with injectant 1, the delay in breakthrough is likely the consequence of dispersion and the interaction of dextran with the rock surface. The maximum effluent fluorescent intensity is ~66% of the intensity of injectant 2, and occurs after 0.85 PVs

Fig. 4 Breakthrough curve and cumulative recovery for injectant 2.



of treated saline water with 1 g/l of BH_8NaO_6 having been injected to flush injectant 2.

Recovery of the FITC-dextran after 5 PVs of treated saline water with BH_8NaO_6 was estimated to be 49% from the breakthrough curve. As in the previous experiment, reversible retention is observed during the flushing phase, resulting in delayed intensity decay of the effluents. After 5 PVs of injectant 2, a fluorescence intensity equilibrium was not achieved, and therefore, rock adsorption capacity was not estimated.

Results and Discussion

The amount of FITC-dextran recovered after flushing the column with 5 PVs of treated saline water, 47% and 49% for injectant 1 and 2, respectively, is relatively low. Subsequently, a decrease in retention is observed when using BH_8NaO_6 as an alkali agent to increase the pH of the solution. This trend is in agreement with previous studies looking at the effect of alkali agents on polymer and dextran retention in carbonate and sandstone media.

Our results show a reduction of two percentage points in FITC-dextran retention when BH_8NaO_6 is added to the injectant. The difference is smaller than what was expected from previous experiments¹⁴ but the experimental conditions, such as flow rate, FITC-dextran molecular weight and alkali agent, are also different from previous experiments and may be the cause for the reduced impact on retention. The results suggest that increasing pH has a positive impact on the transport properties of FITC-dextran during the washing phase, but has a slightly negative impact during the injection phase.

Previous experiments suggested the opposite¹⁴, but experimental conditions were not the same. For instance, BH_8NaO_6 was used as the alkali agent for this work, as opposed to BNaO_2 , although both agents resulted in a solution with a pH of 9. Also, finer marble powder was used to pack the columns used for this work. Finally, the molecular weight of the FITC-dextran used in the latest experiments was 10,000 Da as opposed to 70,000 Da. Additional experiments are therefore required to investigate the effect of flow rate, alkaline agent, FITC-dextran molecular weight, and marble powder grain size on retention.

Conclusions and Recommendations

Two transport experiments were conducted using chromatography columns packed with fine marble powder to investigate the feasibility of using BH_8NaO_6 as an alkali agent to reduce the retention of FITC-dextran flowing through carbonate matrices. The following conclusions can be made from our transport experiments:

- A reduction of two percentage points in retention (47% vs. 49% recovery) is observed when using BH_8NaO_6 to increase the pH of the injectant solution. The observed trend is in agreement with previous studies but the effect is lower than expected.
- BH_8NaO_6 seems to have a negative impact on the transport of FITC-dextran during the injection phase, but a positive impact during the flushing

phase. Overall, increasing pH results in higher FITC-dextran recovery.

- Five PVs of injectant were not enough to reach rock adsorption saturation. Therefore, we were unable to calculate the adsorption capacity of the marble powder.
- The recovery trends observed in our transport experiments are consistent with previous studies evaluating the possibility of using alkali agents to reduce polymer and dextran retention in carbonate and sandstone media.

The following is a list of recommendations for the design of future experimental work:

- Injection at multiple flow rates, and polymer and alkali agent concentrations should be considered to investigate the effect on retention.
- Alternative alkali agents should be evaluated to determine if the effect in retention is only controlled by the pH of the solution.
- The effect of temperature must be investigated.

Overall, the results are encouraging and pave the way for more sophisticated experiments to evaluate the feasibility of improving nanoparticle transport through porous media by altering the pH with alkali agents. It should be noted that real reservoirs are far more complex than the porous media used for these experiments, and therefore, the results may be different when tested in real reservoir rock at reservoir conditions.

Acknowledgments

The authors would like to thank the management of Saudi Aramco for their support and permission to publish this article.

This article was presented at the SPE Abu Dhabi International Petroleum Exhibition and Conference, Abu Dhabi, UAE, November 12-15, 2018.

References

1. He, L., Huang, Y., Zhu, H., Pang, G., et al.: "Drug Delivery: Cancer-Targeted Monodisperse Mesoporous Silica Nanoparticles as Carrier of Ruthenium Polypyridyl Complexes to Enhance Theranostic Effects," *Advanced Functional Materials*, Vol. 24, Issue 19, May 2014, p. 2737.
2. Zeng, R., Liu, L., Li, S., Zou, Y., et al.: "Self-Assembled Silane Film and Silver Nanoparticles Coating on Magnesium Alloys for Corrosion Resistance and Antibacterial Applications," *Acta Metallurgica Sinica*, Vol. 26, Issue 6, December 2013, pp. 681-686.
3. Kang, M., Baeg, K.-J., Khim, D., Noh, Y.-Y., et al.: "Organic Electronics: Printed, Flexible, Organic Nano-Floating-Gate Memory: Effects of Metal Nanoparticles and Blocking Dielectrics on Memory Characteristics," *Advanced Functional Materials*, Vol. 23, Issue 28, July 2013, p. 3482.
4. Fakoya, M.F. and Shah, S.N.: "Emergence of Nanotechnology in the Oil and Gas Industry: Emphasis on the Application of Silica Nanoparticles," *Petroleum*, Vol. 3, Issue 4, December 2017, pp. 391-405.
5. Negin, C., Saedi, A. and Xie, Q.: "Application of Nanotechnology for Enhancing Oil Recovery — A Review," *Petroleum*, Vol. 2, Issue 4, December 2016, pp. 324-333.

6. ShamsiJazeyi, H., Miller, C.A., Wong, M.S., Tour, J.M., et al.: "Polymer Coated Nanoparticles for Enhanced Oil Recovery," *Journal of Applied Polymer Science*, Vol. 131, Issue 15, August 2014, pp. 40576-40588.
7. Prodanovic, M., Ryoo, S., Rahmani, A.R., Kuranov, R.V., et al.: "Effects of Magnetic Field on the Motion of Multiphase Fluids Containing Paramagnetic Nanoparticles in Porous Media," SPE paper 129850, presented at the SPE Improved Oil Recovery Symposium, Tulsa, Oklahoma, April 24-28, 2010.
8. Lu, A-H., Salabas, E.L. and Schüth, F.: "Magnetic Nanoparticles: Synthesis, Protection, Functionalization, and Application," *Angewandte Chemie, International Edition*, Vol. 46, Issue 8, February 2007, pp. 1222-1244.
9. Lan, Q., Liu, C., Yang, F., Liu, S., et al.: "Synthesis of Bilayer Oleic Acid-Coated Fe₃O₄ Nanoparticles and their Application in pH-Responsive Pickering Emulsions," *Journal of Colloid and Interface Science*, Vol. 310, Issue 1, June 2007, pp. 260-269.
10. Zhang, T., Murphy, M.J., Yu, H., Bagaria, H.G., et al.: "Investigation of Nanoparticle Adsorption during Transport in Porous Media," *SPE Journal*, Vol. 20, Issue 4, August 2015, pp. 667-677.
11. Yu, J., An, C., Mo, D., Liu, N., et al.: "Study of Adsorption and Transportation Behavior of Nanoparticles in Three Different Porous Media," SPE paper 153337, presented at the SPE Improved Oil Recovery Symposium, Tulsa, Oklahoma, April 14-18, 2012.
12. Gupta, R. and Mohanty, K.: "Temperature Effects on Surfactant-Aided Imbibition into Fractured Carbonates," *SPE Journal*, Vol. 15, Issue 3, September 2010, pp. 588-597.
13. Mohan, K.: "Alkaline Surfactant Flooding for Tight Carbonate Reservoirs," SPE paper 129516, presented at the SPE Annual Technical Conference and Exhibition, New Orleans, Louisiana, October 4-7, 2009.
14. Felix Servin, J.M., Ellis, E.S., Shateeb, H. and Schmidt, H.K.: "Effect of Alkaline Agents on the Transport of Polysaccharides in a Carbonate Matrix," SPE paper 187589, presented at the SPE Kuwait Oil & Gas Show and Conference, Kuwait City, Kuwait, October 15-18, 2017.
15. Flaaten, A., Nguyen, Q.P., Zhang, J., Mohammadi, H., et al.: "ASP Chemical Flooding without the Need for Soft Water," SPE paper 116754, presented at the SPE Annual Technical Conference and Exhibition, Denver, Colorado, September 21-24, 2008.

About the Authors

Jesus M. Felix Servin

M.S. in Chemical and Biological Engineering, King Abdullah University of Science and Technology

Jesus M. Felix Servin joined the Reservoir Engineering Technology Division of Saudi Aramco's Exploration and Petroleum Engineering Center – Advanced Research Center (EXPEC ARC) in February 2012. His focus is on the development of electromagnetic methods and nanoparticle-based contrast agents for reservoir characterization and monitoring. Jesus's role has been instrumental in the development and deployment of the Magnetic Nano-Mappers project, including hardware design and in-house fabrication, instrumentation, computer programming, and data

processing.

Jesus' interests include the development of nanoscale strategies for reservoir illumination and electromagnetic methods for reservoir description and monitoring.

He received his B.S. degree in Engineering Physics from Instituto Tecnológico y de Estudios Superiores de Monterrey, Monterrey, Mexico, and an M.S. degree in Chemical and Biological Engineering from King Abdullah University of Science and Technology, Thuwal, Saudi Arabia.

Hala A. AlSadeg

B.S. in Materials Science and Engineering, Pennsylvania State University

Hala A. AlSadeg is a Petroleum Scientist working with the Reservoir Engineering Technology Team of Saudi Aramco's Exploration and Petroleum Engineering Center – Advanced Research Center (EXPEC ARC). She works on several research projects aimed at utilizing nanotechnology for enhanced oil recovery and reservoir characterization applications.

In 2018, Hala received her B.S. degree (Honors) in Materials Science and Engineering from the Pennsylvania State University in State College, PA. Her undergraduate research was focused on the fabrication and characterization of two-dimensional heterostructures for sensing and electronic applications.

Efficient CO₂ Multistage Acid Stimulation in Deep Hot-Gas Reservoirs

Dmitrii Gromakovskii, Maharaja Palanivel, Alfredo Lopez, and Vladimir Mikaelyan

Abstract /

Acidizing/acid fracturing is an established method of production stimulation in carbonate reservoirs. Over time, reservoirs become depleted, gas production declines, and flow back initiation can require additional time and cost. Energizing/foaming the stimulation fluid was determined to efficiently improve stimulation results and enhance post-treatment well clean up. The gases most commonly used to energize the treatment fluids include nitrogen (N₂) and carbon dioxide (CO₂). This article presents and discusses the results of an effectiveness study of foamed acidizing treatments performed using multistage completions; successful production outcomes were achieved in depleted reservoirs.

The Design-Execution-Evaluation cycle begins with a multistage fracturing well evaluation to determine whether the well is a candidate for foamed treatment. This evaluation includes studies of the reservoir data (reservoir pressure, lithology, and permeability), completion data — including fracture ports and open hole packers placement vs. hole size, reservoir net pay, and lithology — and offset wells stimulation results. Foamed multistage fracturing treatments are designed to help enhance post-stimulation performance regarding cost, operational efficiency, and completion limitations. Post-job evaluation includes highlighting the treatment as well as production analysis using a numerical simulator. The post-job evaluation also serves as an input to the design of upcoming treatments.

Foamed multistage acidizing using CO₂ foam proved to be successful in terms of post-treatment kickoff, clean up, and production, compared to conventionally treated wells. This success can be attributed to the following effects:

- Faster post-fracture clean up as a result of the decreased liquid volume pumped into the reservoir.
- Higher productivity resulting from acid placement benefits enabled by introducing CO₂ foam (diversion, retardation).
- Well delivery time reduction because the post-treatment N₂ lift was eliminated as a result of CO₂ energy stored in the wellbore and the reservoir.

This article presents the study of CO₂ multistage fracturing treatments compared to conventionally treated multistage fracturing wells. The study results can be used to further optimize treatment designs and improve field execution of upcoming multistage fracturing operations as well as help reduce overall well delivery time.

Introduction

Foamed acidizing treatments using nitrogen (N₂) and carbon dioxide (CO₂) were proven to be helpful in recovering stimulation fluids and removing water or emulsion blocks¹. The three primary issues in an acid fracturing treatment are reactivity control, fluid loss control, and conductivity generation. Foaming the acid helps prevent these issues by providing retardation, increasing treatment fluid efficiency, and providing deeper conductivity generation. Foaming the acid with CO₂ also provides benefits such as a significant increase in fluid efficiency, cleansing the formation of undissolved fines that are not soluble in hydrochloric (HCl) acid, and increasing dissolution while completely reducing or eliminating the need for swabbing the well².

Anderson and Fredrickson (1989)³ compare conductivities of foamed and nonfoamed acid fractures for various acids, proving that foaming significantly improves etched fracture conductivities and helps wash fines away from the fracture face, Table 1.

Because of these proven benefits, CO₂ acid fracturing activity has increased exponentially in the depleted carbonate deep hot-gas reservoirs in the Middle East. This technique has helped complete many prolific wells, even though they have low reservoir pressures.

Completion

Horizontal open hole multistage fracturing completions using swellable packers and ball activated millable

Table 1 Comparison of nonfoamed and foamed acid etched fracture conductivities³.

Formation and Location	Solubility (%)	Depth (ft)	Bottom-hole Temperature (°F)	Acid Type	Etching Time (min)	Fracture Conductivity (md-ft)	
						Nonfoamed	Foamed
Richfield, Michigan, USA	81	4,200	105	28% HCl acid	18	8,278	29,462
					36	14,542	85,857
Pettit, Louisiana, USA	78	6,802	200	28% HCl acid	18	1,426	16,920
					36	2,338	49,296
Marble Falls, Texas, USA	80	3,456	130	Acetic/HCl acid	18	306	2,588
					36	390	2,588
San Andres, Texas, USA	82	5,072	125	15% HCl acid	18	788	4,226
					36	18,292	37,364
San Andres, Texas, USA	85	2,665	100	28% HCl acid	18	0	5,904
					36	460	10,358

fracturing ports were deployed in six candidate wells (Wells A through F). The swellable packers were set across a well gauged section, with an optimal distance between the packers and ports. Placing the packers based on caliper logs is important because communication between stages during an acidizing treatment has been observed in many cases, where acid bypasses the packers easily by eroding the formation in the packer vicinity if they are placed in a washed out borehole section.

The maximum differential pressure rating for this assembly is 10,000 psi. This limitation is important to understand in depleted reservoirs because the back pressure provided by the reservoir is much lower than that of a non-depleted reservoir. Therefore, the surface pressure needs to be limited, so as to not exceed the completion differential pressure capacity.

Reservoir Description

Carbonate-1 is a Permian carbonate formation and the major nonassociated gas reservoir. The formation is divided into four depositional cycles — A, B, C, and D. The first three are usually moderate to good quality reservoirs, while the fourth is usually water-bearing or tight. Composition of the reservoir is mainly dolomites intermingled with limestone with intermittent anhydrite stringers in the tighter sections. Three porosity types are identified in the Carbonate-1 formation — interparticle, intercrystalline, and intermoldic⁴.

The Carbonate-1 formation's current reservoir pressure is lower than the hydrostatic pressure of the water column at the reservoir depth. Therefore, clean up after an acidizing treatment has become challenging and often requires coiled tubing to perform a N₂ lift to help unload the treatment fluids.

Horizontal wells drilled across this reservoir with multistage fracturing completions were typically treated with high quantities of acid and viscous gel. Recent developments in CO₂ availability and economic feasibility in the country makes the CO₂ foamed acid fracturing treatment one of the best possible options to stimulate these wells.

Fracturing Fluids

The primary acid component of the treatment was 26% HCl acid with a synthetic gelling agent. The pad fluid employed to generate the fracture profile and the viscous fingering effect was carboxymethyl hydroxypropyl guar gel with a zirconate crosslinker, which crosslinks at a low pH; higher pH systems are not compatible with CO₂ foams because of the low pH of the carbonic acid developed once the CO₂ contacts the water-based fluid. Either polylactic acid (PLA) based solid biodegradable diverters or a liquid relative permeability modifier were used for diversion, depending on the heterogeneity of the lateral sections to be treated, while considering logistical and economic restraints. Typical designs included CO₂ foams ranging from 40% to 65% internal phase fraction (IPF).

Stimulation Design and Execution

Acid volumes are designed based on total horizontal net pay (> 5% porosity) available. An average of 50 gal to 170 gal of foamed acid per net foot is used. Operational and economic limitations also are considered when choosing the total acid necessary for a treatment. The treatment is divided into cycles, while alternating pad and acid within a cycle, Table 2. Although reservoir pressures are low, initial poor injectivity is observed in most wells, requiring the treatment to begin with an acid spearhead.

A CO₂ IPF was selected based on the severity of the depletion in the well, which ranges from 40% to 65%, with 40% depletion in wells having ~5,000 psi reservoir pressure, and 65% in wells having ~3,500 psi reservoir pressure. Operational limitations, such as the number of CO₂ storage tanks and other economic factors associated with CO₂, are also considered before finalizing the design.

Flush fluid of the initial stages does not contain CO₂, because leaving CO₂ in the wellbore leads to faster pressure buildup during shut-in, and when a ball is dropped into the well for the next stage, it is preferred to not have it free fall in the tubing to help prevent damage, which can cause it to pass through the baffles without seating. Subsequently, the last stage in any horizontal well is flushing and overflushing with the maximum

Table 2 Typical design schedule per stage.

Stage No.	Stage Name	Fluid Type	Bottom-hole CO ₂ Quality (%)	Bottom-hole Fluid Volume (gal)	Bottom-hole Pump Rate (bbl/min)	Pumping Time (min)
	Spearhead	26% Viscosified acid	0	1,000	20	1.2
Cycle 1						
1	Pad	Cross-linked gel	0	1,600	20	1.9
2	Acid	26% Viscosified acid	0	3,600	25	3.4
3	Pad	Cross-linked gel	0	1,600	25	1.5
4	Acid	26% Viscosified acid	0	3,600	25	3.4
5	Diverter	PLA/RPM	60	2,200	25	2.1
Cycle 2						
6	Pad	Cross-linked gel	60	1,800	30	1.4
7	Acid	26% Viscosified acid	60	4,100	30	3.3
8	Pad	Cross-linked gel	60	1,800	30	1.4
9	Acid	26% Viscosified acid	60	4,100	30	3.3
10	Diverter	PLA/RPM	60	2,700	30	2.1
Cycle 3						
11	Pad	Cross-linked gel	60	2,100	35	1.4
12	Acid	26% Viscosified acid	60	4,600	35	3.1
13	Pad	Cross-linked gel	60	2,100	35	1.4
14	Acid	26% Viscosified acid	60	4,600	35	3.1
15	Diverter	PLA/RPM	60	3,200	35	2.2
Cycle 4						
16	Pad	Cross-linked gel	60	2,300	40	1.4
17	Acid	26% Viscosified acid	60	5,100	40	3
18	Pad	Cross-linked gel	60	2,300	40	1.4
19	Acid	26% Viscosified acid	60	5,100	40	3
20	Tank Bottoms	Tank bottoms (acid)	0	1,260	30	1
21	Flush	Treated water	0	5,500	30	4.4
22	Overflush	Treated water	0	8,000	10	19
23	Shut-in					
<i>Totals:</i>				65,260		68.2

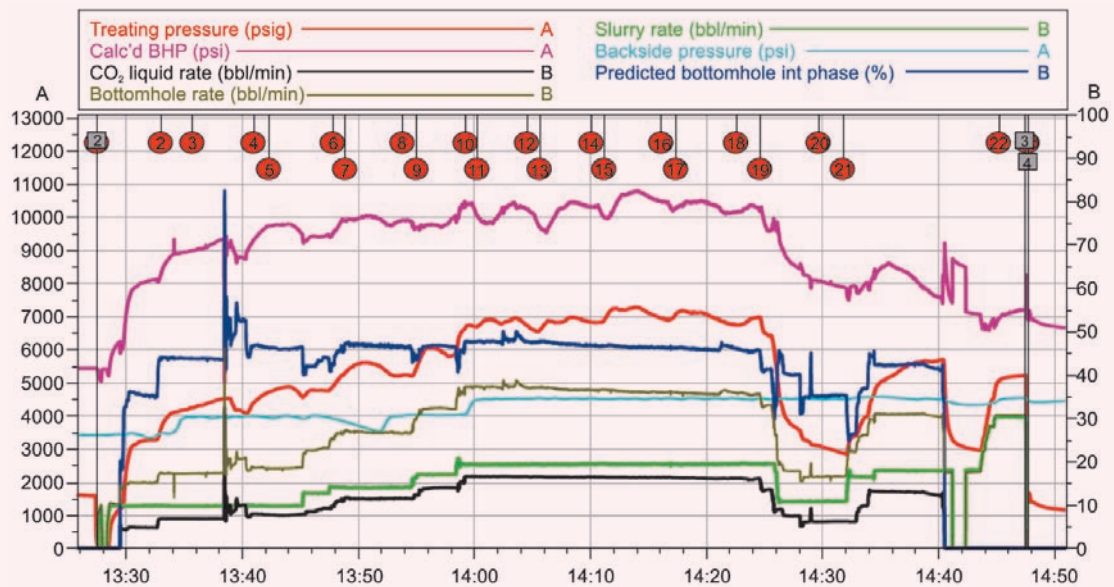
CO₂ IPF designed to help to initiate the flow back for well clean up.

Treatment rates are increased incrementally, as in any acid fracturing treatment, to help overcome the increased fluid loss resulting from greater acid reaction and to maintain the treating pressures above fracturing pressure, Fig. 1.

At the initial phase of multistage acidizing treatments,

the stage frequency used was approximately one stage every two days because of the necessary logistics and decision making after an injection test. The quantities of mixed acid were also much higher than current designs, which went through rigorous optimization to help reduce the stage delivery time by 50%. Treatments are now usually performed at a rate of one stage per day in these completions. The time between stages is typically 18 to

Fig. 1 Typical treatment plot.



20 hours, where the ball is dropped for the next stage, an injection test is performed to verify injectivity, CO₂ is replenished on-site, raw acid is transferred and mixed to the desired concentration with required additives, and quality assurance/quality control verification is performed, etc. Because of disposal concerns, acid for a following stage is not mixed until injectivity is verified. Additionally, pumping CO₂ at night requires a thorough risk assessment, as visibility is severely affected when CO₂ is vented during operations.

As an added benefit, approximately 11,400 bbl of freshwater was conserved when using the CO₂ foamed fluid in these treatments, Fig. 2. As populations and economic growth increase worldwide, competition for potable groundwater has also increased. Therefore, these treatments help reduce the environmental footprint of

such intensive fracturing operations.

Treatment Evaluation

Six horizontal wells having open hole multistage fracturing completions in the same geographical area and the same formation, and treated with similar CO₂ foamed acidizing were evaluated.

Five wells were commercially successful in terms of production, Fig. 3, meeting the expected stabilized gas rate to allow connecting to the gas manifold.

Two wells unloaded all treatment fluids in one day of flow back, while two others unloaded all treatment fluids in two days. Two wells required up to five days to clean up, Fig. 4.

The dimensionless productivity index (J_D)⁵ was used to normalize the available data for the purposes of comparison and evaluation. The concept of the J_D combines the design parameters and procedures in different wells, thereby providing a generalized approach for evaluating the effectiveness of the stimulation treatment.

The J_D Actual (Eqn. A-3) obtained from the productivity index was compared with the J_D Target (Eqn. A-1) to evaluate the effectiveness of the stimulation treatment for all the test wells, Fig. 5.

Observations

Well-A was the most successful in terms of stimulation effectiveness. It had the highest gas rates and the highest J_D among all subject wells. The design used 100 gal of foamed acid/ft of horizontal net pay, and an average foam quality of 46% was pumped. Treatment was performed in three stages, and good isolation between the stages was observed. The average lateral spacing between the

Fig. 2 The freshwater conservation comparison for Wells A through F.

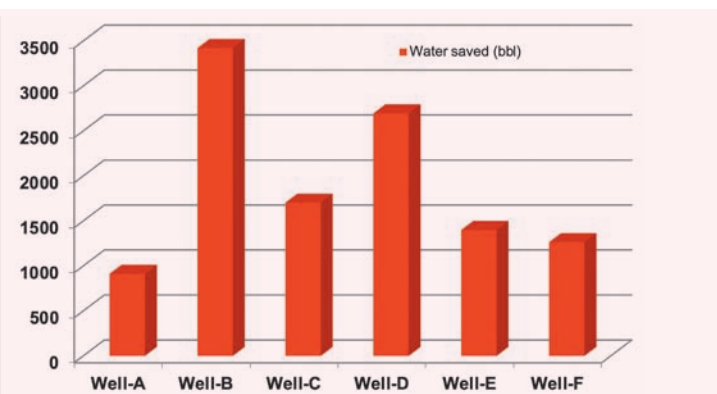


Fig. 3 The gas rate comparison for Wells A through F.

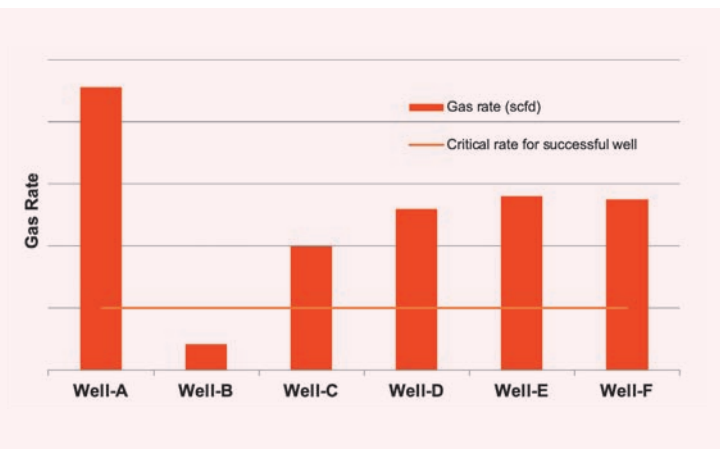


Fig. 4 The clean up time comparison for Wells A through F.

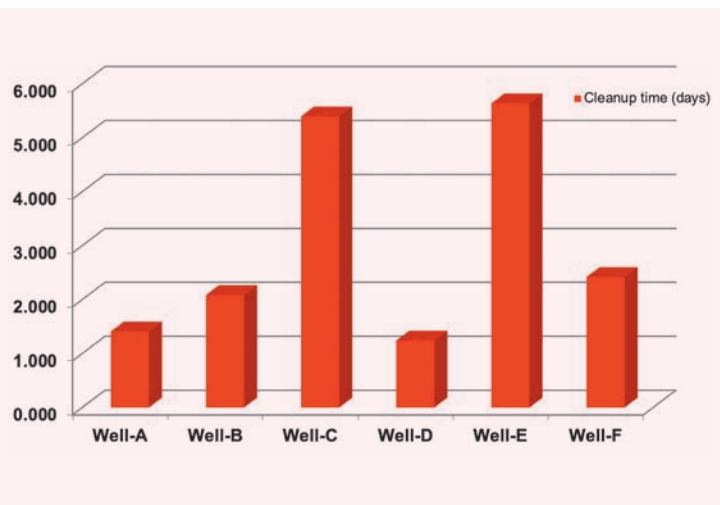
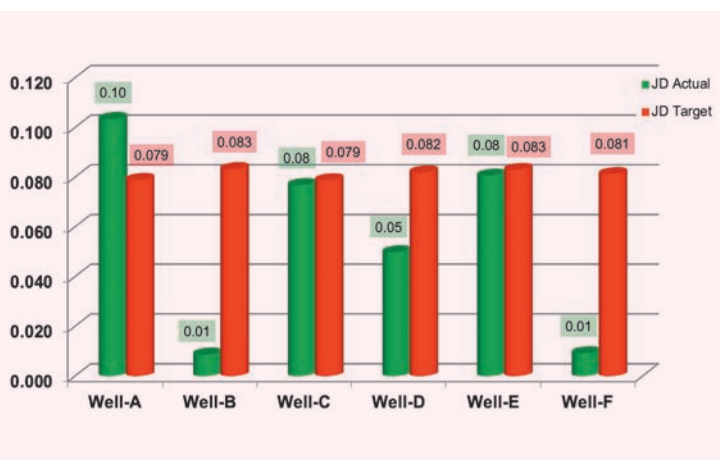


Fig. 5 The J_D comparison for Wells A through F.



stages was 1,552 ft.

Well-B was the least successful in terms of stimulation effectiveness. It had the lowest gas rates and least J_D among all subject wells. The treatment design used 160 gal of foamed acid/ft of horizontal net pay, and an average foam quality of 58% was pumped. Treatment was performed in six stages, and good isolation between stages was observed. Average lateral spacing between the stages was 594 ft. Signatures of communication behind the packers were observed during the treatment for almost all stages. Matrix acidizing was performed at low rates without any pad fluid.

Well-C was successful in terms of stimulation effectiveness. It had sufficient gas rates and the J_D Actual was comparable to the J_D Target. The design used 60 gal of foamed acid/ft of horizontal net pay, and an average foam quality of 53% was pumped. Treatment was performed in four stages, and good isolation between stages was observed. The average lateral spacing between the stages was 1,351 ft.

The Well-D stimulation was moderate, but was expected to be better. Gas rates were better than Well-C, and the J_D Actual was 39% less than the J_D Target. The treatment design used 49 gal of foamed acid/ft of horizontal net pay, and an average foam quality of 64% was pumped. The treatment was performed in four stages, and communication behind the packer was observed between Stages 2 and 3, resulting in understimulation of Stage 3. The average lateral spacing between the stages was 1,078 ft.

Well-E was successful in terms of stimulation effectiveness. It had sufficient gas rates and the J_D Actual was comparable to the J_D Target. The treatment used 170 gal of foamed acid/ft of horizontal net pay, and an average foam quality of 44% was pumped. The treatment was performed in seven stages. Isolation between the stages was questionable, but the PLA diversion stages showed a good pressure response. The average lateral spacing between the stages was 539 ft.

Well-F was not successful in terms

of stimulation effectiveness, although gas production was good and comparable to Wells D and E. The actual J_D Actual was much lower than the J_D Target. The treatment used 41 gal of foamed acid/ft of horizontal net pay instead of the designed 60 gal/ft, because Stage 1 was cancelled resulting from poor injectivity. An average foam quality of 62% was pumped in the remaining two stages. Consequently, Stage 3 had to be pumped at much lower rates than designed because of reduced completion limitations, as the ball could not withstand the differential pressure and passed through the baffle. The average lateral spacing between the stages was 1,465 ft.

Conclusions

The following conclusions are a result of this study:

- A volume of 100 gal of foamed acid/ft of horizontal net pay provided the best results in this reservoir.
- Successful isolation is important for achieving successful stimulation of the reservoir.
- Matrix acidizing at low rates is not recommended for this completion design, as much of the pay is exposed, resulting in understimulation of the well. Treatments need to be pumped at higher rates to remain above closure pressures.
- The PLA solid diverters can help overcome communication behind the packers by sealing the opening between the packer and formation.
- New completion assemblies with a higher differential pressure rating should help achieve better stimulation.

Acknowledgments

The authors would like to thank the management of Saudi Aramco and Halliburton for their support and permission to publish this article.

This article was presented at the SPE Abu Dhabi International Petroleum Exhibition and Conference, Abu Dhabi, UAE, November 12-15, 2018.

Nomenclature

A	half-length of the drainage eclipse in the horizontal plane (ft)
h	net thickness (ft)
I_{ani}	permeability anisotropy ratio (dimensionless)
J_D	dimensionless productivity index
k	reservoir permeability (horizontal if not denoted) (md)
kh	horizontal reservoir permeability (md)
kv	vertical reservoir permeability (md)
L	lateral length (ft)
p	reservoir pressure (psi)
p_{wf}	flowing wellhead pressure (psi)
q	gas flow rate (scfd)
r_eH	horizontal drainage radius (ft)
r_w	wellbore radius (ft)
s	skin effect (dimensionless)

References

1. Neill, G.H., Dobbs, J.B., Pruitt, G.T. and Crawford, H.R.: "Field and Laboratory Results of Carbon Dioxide and Nitrogen in Well Stimulation," *Journal of Petroleum Technology*, Vol. 16, Issue 3, March 1964, pp. 244-248.
2. Decker, R.L., Hyman, M.D. and Ridge, J.J.: "CO₂ Foamed Well Treatments," U.S. Patent No. 7,464,754 B1, December 2008.
3. Anderson, M.S. and Fredrickson, S.E.: "Dynamic Etching Tests Aid Fracture Acidizing Treatment Design," *SPE Production Engineering*, Vol. 4, Issue 4, November 1989, pp. 443-449.
4. Rahim, Z., Al-Anazi, H., Al-Kanaan, A. and Aziz, A.A.: "Successful Exploitation of Khuff-B Low Permeability Gas Condensate Reservoir through Optimized Development Strategy," SPE paper 136953, presented at the SPE/DGS Saudi Arabia Section Technical Symposium and Exhibition, al-Khobar, Saudi Arabia, April 4-7, 2010.
5. Diyashev, I.R. and Economides, M.J.: "The Dimensionless Productivity Index as a General Approach to Well Evaluation," *SPE Production & Operations*, Vol. 21, Issue 3, August 2006, pp. 394-401.

Appendix

Eqn. A-1 shows the dimensionless productivity index (J_D Target) for horizontal wells⁵:

$$J_D = \frac{1}{\ln \left[\frac{a + \sqrt{a^2 - (L/2)^2}}{L/2} \right] - 0.75 + \frac{I_{ani} h}{L} \left(\ln \left(\frac{I_{ani} h}{r_w (I_{ani} + 1)} \right) + s \right)} \quad (A-1)$$

Eqn. A-2 shows the permeability anisotropy ratio (I_{ani}) for horizontal wells⁵:

$$I_{ani} = \sqrt{\frac{k_H}{k_V}} \quad (A-2)$$

Eqn. A-3 shows the relationship between dimensioned productivity index and dimensionless J_D (J_D Actual) for gas wells⁵:

$$\frac{q}{p^2 - p_{wf}^2} = \frac{kh}{\alpha_r \mu Z T} J_D \quad (A-3)$$

Eqn. A-4 shows the half-length of the drainage eclipse in the horizontal plane⁵:

$$a = \frac{L}{2} \left\{ 0.5 + \left[0.25 + \left(\frac{r_e H}{L/2} \right)^4 \right]^{0.5} \right\}^{0.5} \quad (A-4)$$

About the Authors

Dmitrii Gromakovskii

*M.S. in Petroleum Engineering,
Heriot-Watt University*

Dmitrii Gromakovskii joined Saudi Aramco in 2012 as a Petroleum Engineer. He is currently working as a Production Engineer in the Hawiyah Gas Production Engineering Unit of the Southern Area Production Engineering Department. Dmitrii has extensive experience in hydrocarbon production engineering and enhancement through fracturing and stimulation. He

also has varied oil and gas technical/operational experience.

Dmitrii received his M.S. degree in Petroleum Engineering from Heriot-Watt University, Edinburgh, U.K. He is a Society of Petroleum Engineer (SPE) Certified Petroleum Engineer.

Maharaja Palanivel

*B.S. in Automobile Engineering,
Anna University*

Maharaja Palanivel is a Technical Adviser with Halliburton Energy Services, responsible for the planning and designing of hydraulic fracturing and acidizing applications in Saudi Arabia and Bahrain. He also supervises the field engineering team while mentoring and developing them. Maharaja joined

Halliburton in 2011 as an Associate Technical Professional and has held a variety of positions in the engineering discipline during the past 7 years.

He received his B.S. degree in Automobile Engineering from Anna University, Tamil Nadu, India.

Alfredo Lopez

*B.S. in Petroleum Engineering,
University of Zulia*

Alfredo Lopez is a Technical Adviser for Halliburton in Saudi Arabia. He served as part of the Production Enhancement Team supporting Saudi Aramco on the technical aspects of fracturing and stimulation in oil and gas wells, and on developing engineered solutions and new technology applications to improve productivity for conventional and unconventional reservoirs. Prior to this assignment, Alfredo held

technical and sales positions in Venezuela. Overall, he has 23 years of experience with Halliburton, in the areas of acid stimulation, fracturing, well intervention, sand control, cementing, and water control.

In 1995, Alfredo received his B.S. degree in Petroleum Engineering from the University of Zulia, Maracaibo, Venezuela.

Vladimir Mikaelyan

*M.S. in Petroleum Engineering,
Tyumen Oil and Gas State University*

Vladimir Mikaelyan is a Principal Stimulation Engineer at Halliburton, with over 10 years of experience. Prior to joining Halliburton, he worked with Surgutneftegas, an oil and gas producer company, as an Oil Production Technologist. With Halliburton, Vladimir provided both field and desk engineering support to a number of customers in Russia from 2006 to 2012, covering onshore projects in Western Siberia as well as offshore conformance operations on Sakhalin Island.

In 2013, he joined Halliburton Energy Services Saudi Arabia, and now works as an in-house Engineer on the Saudi Aramco unconventional project supporting Saudi Aramco's Southern Ghawar Production Engineering Department.

Vladimir received his B.S. and M.S. degrees in Petroleum Engineering from Tyumen Oil and Gas State University, Western Siberia, Russia.

Measuring Oil-Water Mixture Densities for Downhole Oil Field Operations Using Inclination Angle Method

Dr. Chidirim E. Ejim and Dr. Jinjiang Xiao

Abstract /

Information on mixture density is important in downhole operations involved in pumping oil and water to determine, for example, water cut, which can be used to monitor in situ production changes. This study presents a method to determine the oil-water mixture density by applying first principle fluid mechanics to data representative of the downhole production measurements. Knowledge of oil-water mixture density in upstream and downstream oil field operations is essential for optimum production management.

A 3½", 9.20 lb/ft pipe, and a 7", 26 lb/ft pipe, typically used as tubing and casing, respectively, were installed in an oil-water test flow loop. The total flow rates were varied from 2,000 barrels per day (bpd) to 12,000 bpd, with the corresponding water cuts determined from the tests. The oil-water mixture densities were determined from the water cut measurements during the test. Pressure drop data was collected at different inclination angles. The inclination angle method was used to compute the oil-water mixture densities for 40° and 60° inclination angles. The results were compared with mixture densities obtained from test water cut measurements.

The estimated values of mixture densities for the 40° and 60° inclination angles varied from 45.9 lb/ft³ to 63.5 lb/ft³. The results showed that the percentage error in the oil-water mixture densities obtained from the inclination angle method compared to the mixture densities obtained from the test water cut measurements was within 7.5%. These results suggest that having simple pressure measurements combined with known inclination angles can be employed to measure the densities of oil-water mixtures. It can be concluded that the inclination angle method of measuring oil-water mixture density is fairly accurate, and offers an alternative method of measuring the mixture densities of oil-water flows.

This study highlights a different method of estimating mixture densities in flows involving oil-water mixtures typical of oil field production operations. The method is simple and has the advantage of easy integration into a flow measurement system. Such systems are beneficial to oil field operators for optimum production management of hydrocarbon reserves from a field asset.

Introduction

Production of oil-water mixtures is very common in oil field operations, either for nonproduction or production logging. One of the physical properties of the fluid mixture required by production engineers, reservoir engineers, artificial lift engineers, or the field operator, is the density of the oil-water mixture, which can be used to estimate the water cut of the produced fluid downhole. Water cut is the ratio of water volume flow rate to the oil-water volume flow rate; however, to determine the production water cut, accurate knowledge of the downhole oil-water mixture density is needed.

Electric submersible pumps (ESPs) are a type of artificial lift method used in the oil and gas industry to either lift reservoir fluids from dead wells or boost production from naturally flowing wells. ESPs operate favorably when pumping pure liquids, e.g., water or oil, or liquid with very low gas content. Depending on the proportions of oil and water, or water cut, from the reservoir, the density of the oil-water mixture can vary substantially, thereby affecting the ESP operation. For instance, an increase in water cut results in an increase in the oil-water mixture density, which tends to increase the power consumption of the ESP motor as it does more work to lift the heavier production fluid mixture to the surface. Therefore, the ability to measure the oil-water mixture density downhole is desirable to the field operator to obtain additional information on the flow condition of the ESP for increased operational efficiency of the artificial lift system.

There are tools available to measure the fluid density downhole. The two main types of tools are those based on the gamma ray densitometer and the gradiomanometer¹.

The gamma ray tool is based on the principle that the absorbance of gamma rays is inversely proportional to the density of the medium through which the gamma rays pass. The tool consists of a gamma ray source, a channel through which the fluid medium can flow through, and a gamma ray detector. Cited limitations of

the gamma ray tool include low sensitivity in oil-water flows, small sampling size and the statistical nature of the measurement due to fluctuations in the readings, which is inherent in any nuclear measurement. In addition, the use of nuclear-based technology can cause health, safety, security, and environment concerns, which can be prohibited in some operator jurisdictions.

The gradiomanometer is a device used to determine average fluid density by measuring the pressure difference between two pressure sensors. The pressure sensors are typically spaced (axially) about 2 ft from each other. The accuracy of the gradiomanometer is affected by well deviation, kinetic effect, and friction effect. Well deviation is the change in direction of the well trajectory from vertical. The kinetic effect occurs from the difference in fluid velocity at the upper and lower sensor locations, which is typically caused by a change in geometry at the respective locations. The friction effect is due to pressure losses resulting from tool surface friction, and depends on the tool geometry and flow rate.

During density measurements using a gradiomanometer, only the pressure difference measurements and well deviation corrections are used to determine the average fluid density. The friction effect is typically neglected for flow rates below 2,000 barrels per day (bpd)². Neglecting the friction term affects the accuracy of the gradiomanometer. For flow rates above 2,000 bpd, where the frictional term is not neglected, determining the oil-water mixture density can be complicated since the fluid density is an implicit function of the friction factor term in the flow hydraulics³. A further cited limitation of the gradiomanometer is the degree of well deviation in which they are used. Measurements are not valid in horizontal wells, and as such, use of these tools are restricted only to vertical or inclined wells.

Although the gradiomanometer is commonly used in the oil and gas industry, there is still a need to explore related measurement principles, which are simple to use and can be more tolerant to high well deviation when performing oil-water mixture density measurements. A further application is the potential incorporation of such a tool into an ESP system for potential in situ measurements. This study presents the underlying principles for such a technique in measuring oil-water mixture densities.

Background Theory

Mixture density estimation requires an understanding of hydraulics through pipes or annular conduits. From elementary fluid mechanics, and applying the steady flow energy equation⁴, it can be seen from the first principle that the pressure gradient in a fluid flowing in a conduit can be given as:

$$\frac{\Delta P}{L} = g\rho_m \sin\theta + \frac{8f\rho_m Q_m^2}{\pi^2 D^5} \quad 1$$

where ΔP = total pressure loss between measurement points, L = axial distance between the pressure measurement points, g = acceleration due to gravity, θ = inclination angle (from the horizontal) of the flow axis, ρ_m = density of oil-water mixture, Q_m = volume

flow rate of oil-water mixture, D = hydraulic diameter of the conduit, and f = friction factor.

The friction factor is a function of the relative pipe roughness $\left(\frac{\varepsilon}{D}\right)$ and Reynolds Number $\left(\frac{4\rho_m Q_m}{\pi D \mu_m}\right)$, where ε is the absolute roughness of the wetted pipe wall, and μ_m is the absolute or dynamic viscosity of the oil-water mixture.

For a given mixture flow rate and pipe hydraulic diameter, to determine the mixture density, pressure drop measurements can be made along two sections, "1" and "2," of a pipe having two different inclination angles, θ_1 and θ_2 , respectively, from the horizontal. As such, Eqn. 1 can be written as shown in Eqns. 2 and 3, where subscripts "1" and "2" refer to the corresponding parameters defined earlier for pipe sections "1" and "2," respectively.

$$\frac{\Delta P_1}{L_1} = g\rho_m \sin\theta_1 + \frac{8f\rho_m Q_m^2}{\pi^2 D^5} \quad 2$$

$$\frac{\Delta P_2}{L_2} = g\rho_m \sin\theta_2 + \frac{8f\rho_m Q_m^2}{\pi^2 D^5} \quad 3$$

From Eqns. 2 and 3, the parameters ε , D , ρ_m , Q_m , and μ_m are the same in both pipe sections for the same pipe material and condition. Therefore, the second terms on the right-hand side of the equations are equal. Solving Eqns. 2 and 3 gives an equation for the mixture density as:

$$\rho_m = \frac{\frac{\Delta P_1}{L_1} - \frac{\Delta P_2}{L_2}}{g(\sin\theta_1 - \sin\theta_2)} \quad 4$$

Given the same flow rate and conduit size, Eqn. 4 indicates that the mixture density can be determined simply from knowing an operating parameter (pressure drop measurements), and geometric parameters (axial length and inclination angle). Equation 4 is not restricted to a pure cylindrical conduit, but is also applicable to annular pipe sections.

To determine the error in estimating the mixture density using Eqn. 4, the density is compared to that obtained based on a homogeneous mixture from measured flow properties. For a homogeneous mixture of oil and water, using mass balance and applying continuity, the following equations result:

$$Q_m = Q_o + Q_w \quad 5$$

$$\rho_m = \frac{Q_o}{Q_w + Q_o} \rho_o + \frac{Q_w}{Q_w + Q_o} \rho_w \quad 6$$

$$\rho_m = \alpha_o \rho_o + \alpha_w \rho_w \quad 7$$

$$\rho_m = (1 - \alpha_w) \rho_o + (\alpha_w) \rho_w \quad 8$$

where Q_o = oil flow rate, Q_w = water flow rate, ρ_o = oil density, ρ_w = water density, α_o = oil cut, and α_w = water cut.

Using either Eqns. 6, 7, or 8 to obtain the actual or measured homogeneous mixture density, the percent error in density measurement obtained from Eqn. 4 is given by:

Density Estimate %Error =

$$\left[\frac{(\rho_m)_{\text{Equation (4)}} - (\rho_m)_{\text{Equation (6)}}}{(\rho_m)_{\text{Equation (6)}}} \right] \times 100 \quad 9$$

Experimental Layout and Procedure

Figure 1 is a schematic of the experimental layout used to check the percent error of Eqn. 4 for oil-water mixture density estimation. Mineral oil EXXSOL D80 and water were used as the test fluids. The fluids were held in separate sections of an oil-water separator, with each fluid supplied into the system by their respective pumps. Flow control and measurement were accomplished using the valves and turbine flow meters, respectively, on each line.

Flows from the oil and water lines enter a static mixer section, where the fluids are properly mixed before the mixture enters the annular pipe section. The annular section comprises of a smaller casing within a larger casing size, representative of a typical annulus formed between a casing's internal diameter and the equipment's outer diameter in a wellbore. Pressure drop measurements were made by a differential pressure transmitter from pressure taps within the straight section of the annular pipe section. The taps were located to allow the oil-water mixture to have a fully developed flow within the measurement section downstream of the static mixer. The annular section is mounted on an adjustable frame

Fig. 1 Schematic of the experimental layout to estimate the oil-water mixture density.

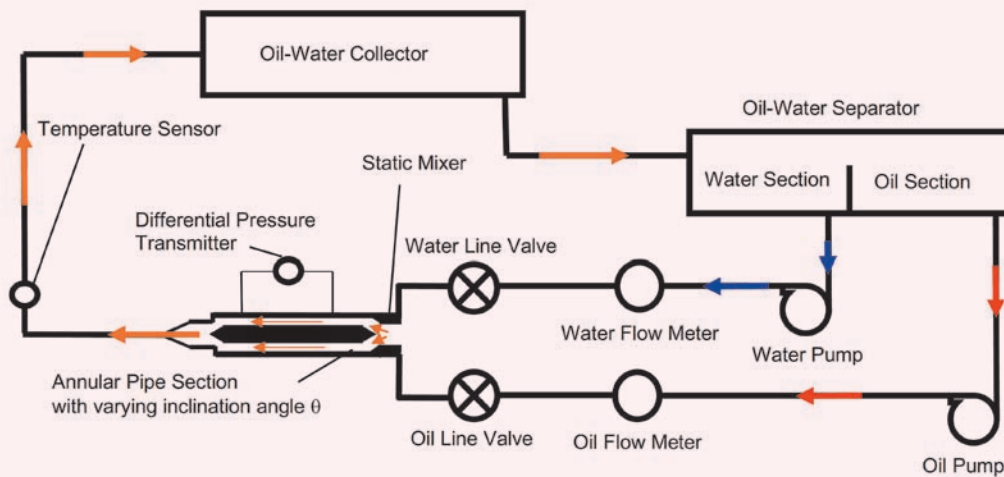


Table 1 Oil and water average fluid properties at 102 °F.

	Density (lb/ft ³)	Absolute Viscosity (cP)	Flow Range (bpd)
EXXSOL D80 Oil	48.1	1.328	0 – 12,000
Water	61.9	0.668	0 – 12,000

Table 2 Additional test information.

Description	Dimensions
Smaller Diameter of Annular Section, D_i (in)	3.50
Larger Diameter of Annular Section, D_o (in)	6.28
Distance between pressure taps, L (in)	38.98
Absolute pipe roughness for commercial steel pipe, ϵ (ft) ⁵	1.5×10^{-4}
Annular pipe inclination angles from horizontal, θ (°)	0, 40, 60, 90

that can be tilted to various inclination angles.

Further downstream after the fluid pressure drop measurement section, the oil-water mixture flows through a return line, where the mixture temperature is measured using a temperature sensor. The oil-water mixture flow rate through the test loop is assumed to be isothermal because of the large liquid reservoir volume used during the test. The oil-water mixture flows into a collector tank and then into an oil-water separator tank, where the fluids are separated by gravity and the flow process is repeated within the closed loop flow system. The temperature throughout the tests varied from 97 °F to 104 °F. Table 1 shows the fluid properties at the average test temperature of 102 °F, and Table 2 presents other test information.

In performing the test, the system was allowed to stabilize to the required flow conditions before the required test data was acquired. For each inclination angle of the annular test section and a specific water cut, about six data points were collected for varying volume flow rates of water and oil. The total (oil and water) volume flow rates tested were 2,000 bpd, 4,000 bpd, 6,000 bpd, 8,000 bpd, 10,000 bpd, and 12,000 bpd, with corresponding water cuts of 0%, 20%, 40%, 60%, 80%, and 100%. In total, about 142 data points were collected during the tests; however, 72 data points — for $\theta = 40^\circ$ and 60° — were used to check the density measurement analysis. These inclinations were selected since they are nonhorizontal and nonvertical. The measured variables for these inclinations were substituted into Eqn. 4 to determine the oil-water mixture densities. The corresponding homogeneous oil-water mixture densities were obtained using the measured flow rates and substituted into Eqn. 6. The error in estimating mixture densities using the inclination angle method of Eqn. 4 was computed from Eqn. 9.

Results and Discussion

For brevity, the number of plots in this section have been selected to show the variation of percentage error in the inclination angle method for a given measured water cut for all the test flow rates. The water cuts are grouped into less than 40%, 40% to 60%, and greater than 60%, to represent low, medium, and high water cut ranges measured during the test. The other set of plots show the percent error variation for a given total (oil-water mixture) flow rate and all test water cuts. These can be grouped as low-flow (less than 4,000 bpd), medium-flow (4,000 bpd to 8,000 bpd) and high-flow (greater than 8,000 bpd) rates, with respect to the range of flow rates in this study. The results presented here are for 40° and 60° inclination angles for the reasons highlighted in the previous section.

Oil-Water Mixture Density Estimate Variation at Different Water Cuts

Figure 2 shows the variation of the density estimate percent error of water cuts at 0% and 20%. For the 0% water cut, the mixture density is underestimated by up to 4.5%. For the 20% water cut, the percent error varied from -6.7% to 1.8%. Comparing the density values of both water cuts, there is an overall increase

Fig. 2 Variation of percent error with estimated mixture density of water cuts at 0% and 20%.

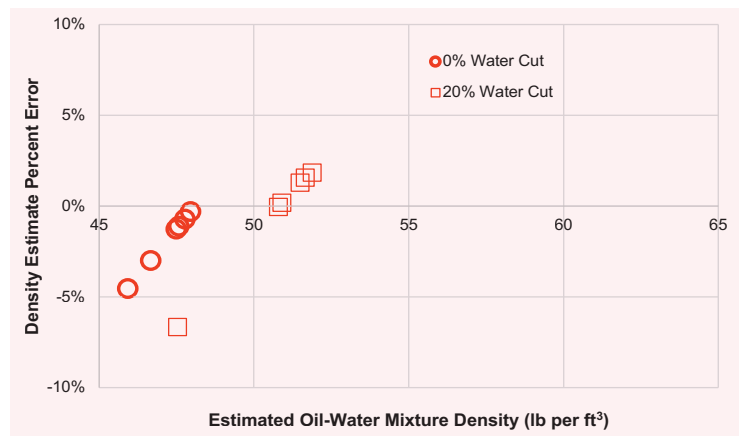


Fig. 3 Variation of percent error with estimated mixture density of water cuts at 40% and 60%.

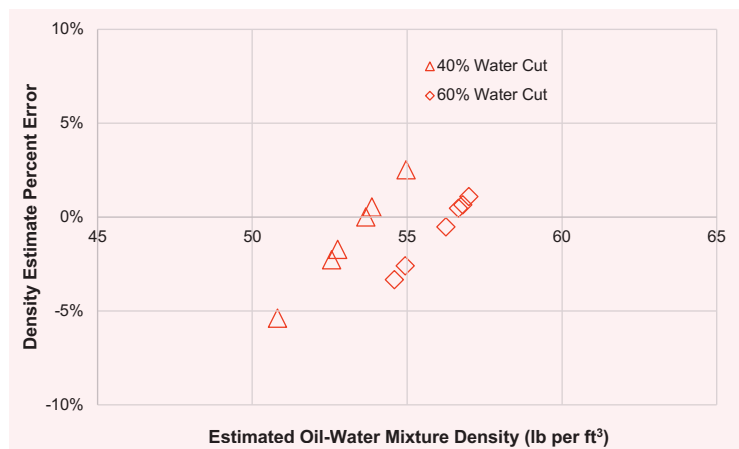


Fig. 4 Variation of percent error with estimated mixture density of water cuts at 80% and 100%.

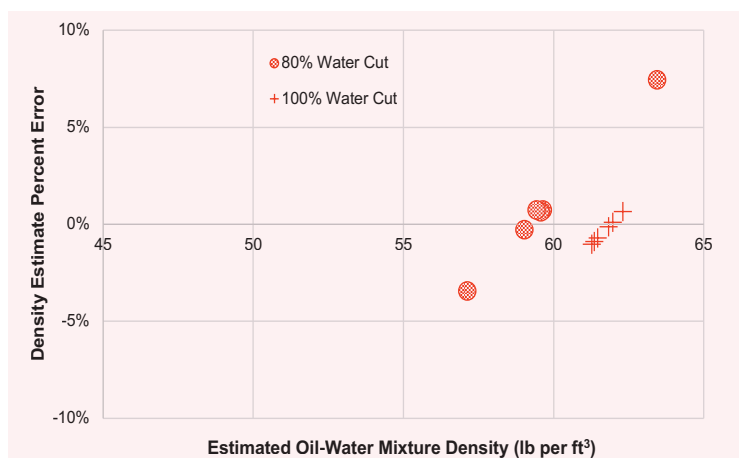


Fig. 5 Variation of percent error with estimated mixture density at 2,000 bpd and 4,000 bpd.

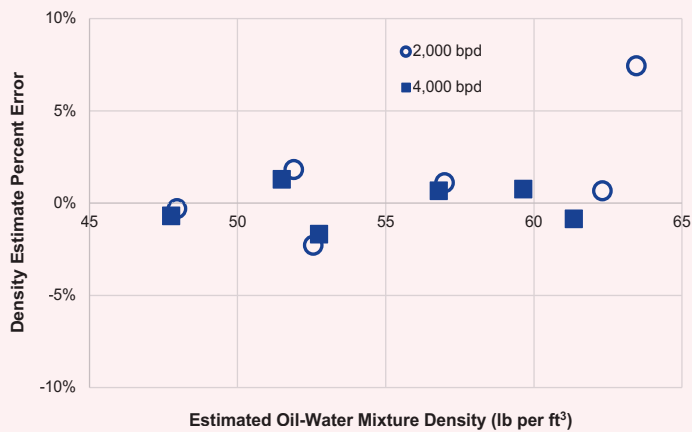


Fig. 6 Variation of percent error with estimated mixture density at 6,000 bpd and 8,000 bpd.

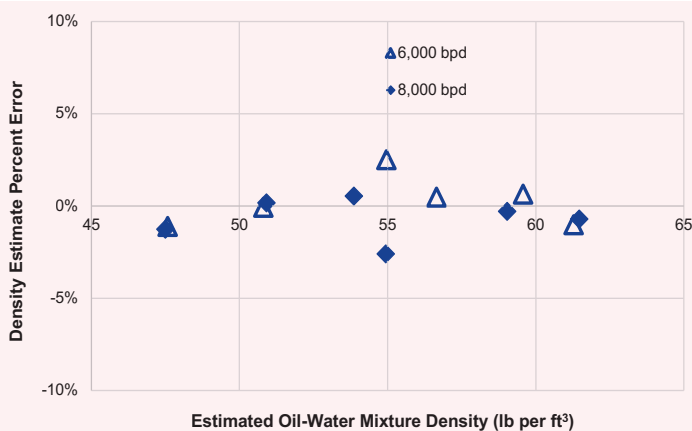
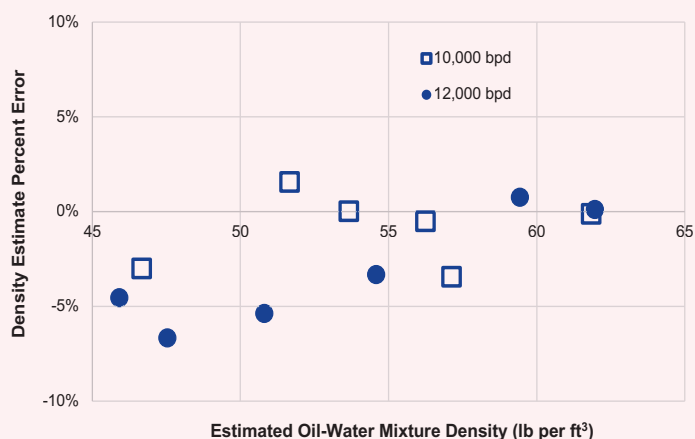


Fig. 7 Variation of percent error with estimated mixture density at 10,000 bpd and 12,000 bpd.



in the mixture density as the water cut increased from 0% to 20%. Since the density of water — 61.9 lb/ft³ — is greater than the density of oil — 48.1 lb/ft³ — an increase in the proportion of water in the mixture would tend to increase the mixture density over that of pure oil — 0% water cut. Therefore, the observed increase in oil-water mixture density with water cut is consistent with fundamental principles. Based on the percent error range for these low water cuts, the estimated density using the inclination angle method of Eqn. 4 can be seen to yield reasonable results.

Figure 3 shows the variation of the density estimate percent error of water cuts at 40% and 60%. The percent error varied from -5.4% to 2.5% for the 40% water cut measurements, and from -3.3% to 1.1% for the 60% water cut tests. Similar to Fig. 2, there is a trend of increasing mixture density as the water cut changes from 40% to 60%.

Figure 4 presents the results for the high water cut group of 80% and 100%. The percent error varied from -3.4% to 7.4%, and -1.0% to 0.7%, for the 80% and 100% water cuts, respectively. The same trend of increasing mixture density with water cuts was also observed as in Figs. 2 and 3. From Figs. 2 to 4, the highest underprediction (-6.7%) occurred at 20% water cut, whereas the highest overprediction (7.4%) occurred at 80% water cut. The overall magnitude of estimated oil-water mixture densities varied from 45.9 lb/ft³ to 63.5 lb/ft³. This density range is wider compared to density values between 48.1 lb/ft³ and 61.9 lb/ft³ for oil and water, respectively, as previously stated. Some of these errors may be attributed to the change in fluid properties within the test temperature range. Other potential error contribution includes measurement discrepancy due to some fluid contamination within the system during the tests. Moreover, based on the error range observed during the test, the results indicate that irrespective of the low, medium or high water cut groups tested in this study, the inclination angle method of measuring oil-water mixture densities gives realistic results.

Oil-Water Density Estimate Variation at Different Total Mixture Flow Rates

Figures 5 to 7 were replotted from Figs. 2 to 4 to present how the mixture density estimate varies at given total oil and water flow rates, and all water cuts during the test. Figure 5 shows the results for the low-flow range (2,000 bpd to 4,000 bpd) flow rates for this study. The maximum variation in percent error for the 2,000 bpd flow rate is from -2.3% to 7.4%, whereas the error range is from -1.7% to 1.3%, for the 4,000 bpd tests. As the total flow rate increases into the medium-flow range of the test, Fig. 6 shows that the percent error range varies from -1% to 2.5% and -2.6% to 0.5% for the 6,000 bpd, and 8,000 bpd, respectively. For the high-flow range, the percent errors varied from -3.4% to 1.6% at 10,000 bpd, whereas for 12,000 bpd, the percent error range varied from -6.7% to 0.7%. From these results, the highest underprediction occurred at 12,000 bpd, whereas the highest mixture density overprediction occurred at the total flow rate of 2,000 bpd.

Summary and Conclusions

The current work presented the method of using the inclination angle method to determine the density of oil-water mixtures. The results shown in this study are for 40° and 60° inclination angles. The method was tested by varying the total flow rate of oil and water from 2,000 bpd to 12,000 bpd, and for water cuts ranging from 0% to 100%. The maximum range of percent error varied from -6.7% to 7.4%. The highest underprediction (-6.7%) of the oil-water mixture density occurred for a total flow rate of 12,000 bpd and 20% water cut, whereas the highest overprediction (7.4%) occurred for a total flow rate of 2,000 bpd and 80% water cut. The magnitude of estimated oil-water mixture densities varied from 45.9 lb/ft³ to 63.5 lb/ft³. Observation of the oil-water mixture density variation for different water cuts showed a progressing increase in oil-water mixture density as the water cut was increased from 0% to 100%. This observation is consistent with fundamental principles as oil-water mixture density increases with water cut. Based on the magnitude of the percent errors from this study, it indicates that the inclination angle method provides a reasonable method of determining the density of oil-water mixtures.

Given the realistic results observed for the method presented in this study, it is feasible to have a device with the same working principle, which can be used to determine oil-water mixture densities. For oil field operations, determining the oil-water mixture density, especially in situ, is desirable, e.g., in downhole production using ESPs. The inclination angle method presented in this work offers a simple and fairly accurate means of obtaining such oil-water mixture density measurements. The technique can be easily incorporated as part of the metering system for ESPs downhole. Such systems add value to field operators by providing efficient management of their hydrocarbon reserve.

Acknowledgments

The authors would like to thank the management of Saudi Aramco for their support and permission to publish this article.

Nomenclature

D	= hydraulic diameter of the conduit, inch (or m)
D_i	= smaller diameter of annular pipe section, inch (or m)
D_o	= larger diameter of annular pipe section, inch (or m)
f	= friction factor
g	= acceleration due to gravity, ft/s ² (or m/s ²)
L	= axial distance between the pressure measurement points, ft (or m)
L_1	= axial distance between the pressure measurement points of inclined Section 1, ft (or m)
L_2	= axial distance between the pressure measurement points of inclined Section 2, ft (or m)
Q_m	= volume flow rate of oil-water mixture, bpd (or m ³ /s)
Q_o	= volume flow rate of oil, bpd (or m ³ /s)
Q_w	= volume flow rate of water, bpd (or m ³ /s)
α_o	= oil cut
α_w	= water cut
ΔP	= total pressure loss between measurement points, psi (or Pa)
ΔP_1	= total pressure loss between measurement points in inclined Section 1, psi (or Pa)
ΔP_2	= total pressure loss between measurement points in inclined Section 2, psi (or Pa)
ϵ	= absolute roughness of the wetted pipe wall, ft (or m)
μ_m	= absolute or dynamic viscosity of the oil-water mixture, cP (or Pa-s)
ρ_m	= density of oil-water mixture, lb/ft ³ (or kg/m ³)
ρ_o	= oil density, lb/ft ³ (or kg/m ³)
ρ_w	= water density, lb/ft ³ (or kg/m ³)
θ	= inclination angle (from the horizontal) of the flow axis (°)
θ_1	= inclination angle (from the horizontal) of the flow axis in Section 1 (°)
θ_2	= inclination angle (from the horizontal) of the flow axis in Section 2 (°)

References

1. Liu, H.: *Principles and Applications of Well Logging*, 2nd edition, Berlin: Springer, 2017, 356 p.
2. Schlumberger, *Oilfield Glossary*, https://www.glossary.oilfield.slb.com/Terms/f/friction_effect.aspx, 2019.
3. Streeter, V.L. and Wylie, E.B.: *Fluid Mechanics*, 1st edition, Singapore: McGraw-Hill, 1983, 562 p.
4. Douglas, J.F., Gasiorek, J.M. and Swaffield, J.A.: *Fluid Mechanics*, 3rd edition, Singapore: Longman, 1995, 819 p.
5. Flowserve: *Cameron Hydraulic Data*, 19th edition, Heald, C.C. (ed.), Flowserve, 2010.

About the Authors**Dr. Chidirim E. Ejim**

*Ph.D. in Mechanical Engineering,
University of Alberta*

Dr. Chidirim E. Ejim is a Petroleum Engineer working in the artificial lift focus area within the Production Technology Team of Saudi Aramco's Exploration and Petroleum Engineering Center – Advanced Research Center (EXPEC ARC). Prior to joining Saudi Aramco in 2014, Chidirim spent over 7 years with Schlumberger's Artificial Lift Segment, working on surface horizontal pumping systems; downhole pump design,

development and testing; multiphase production systems; as well as downhole gas separator/gas handler testing and analysis.

He received his B.Eng. degree (Honors) from the University of Malta, Msida, Malta; his M.S. degree from the University of Waterloo, Ontario, Canada; and his Ph.D. degree from the University of Alberta, Edmonton, Canada, all in Mechanical Engineering.

Dr. Jinjiang Xiao

*Ph.D. in Petroleum Engineering,
University of Tulsa*

Dr. Jinjiang Xiao is a Senior Petroleum Engineering Consultant working in Saudi Aramco's Exploration and Petroleum Engineering Center – Advanced Research Center (EXPEC ARC). His current focus is artificial lift research and development.

Prior to joining Saudi Aramco in 2003, Jinjiang spent

10 years with Amoco and later BP-Amoco, working on multiphase flow, flow assurance and deepwater production engineering.

He received both his M.S. and Ph.D. degrees in Petroleum Engineering from the University of Tulsa, Tulsa, OK.

Forward Integration of Dynamic Data into 3D Static Modeling Significantly Improves Reservoir Characterization

Babatope O. Kayode, Otto E. Meza Carmargo, Nerio Quintero Tudares, and Shaikha S. Al-Dossary

Abstract /

Geomodeling is usually done to honor static data such as core data, well logs, and seismic acoustic impedance (AI) maps where available. Once the static geomodel is complete, history matching is carried out by tuning the static model properties until the model reproduces the observed dynamic behavior. The objective of this article is to showcase how a systematic a-priori integration of dynamic elements into geomodeling eliminated the need for history matching. These dynamic elements are connected reservoir regions (CRRs)¹ and permeability thickness (kh) interpretation from pressure transient analysis (PTA). This article also introduces the concept of CRR-based permeability modeling.

CRRs were defined based on time-lapse shut-in pressure trend groups. Core and log data were grouped on the basis of the identified CRR and used to build CRR-based neural network models for predicting permeability logs of noncored wells within each CRR. The geomodeler then created two geo-realizations by using the permeability logs within each CRR to distribute permeability within the CRR using two assumptions of variogram lengths: (1) variogram range obtained from the analysis of limited core data, and (2) variogram range required to ensure intra-CRR connectivity.

Pressure transient was simulated for wells with observed PTA data using the two realizations, and a comparison of the log-log plots of simulated pressure transient derivative and observed pressure transient derivative were used to determine the quality of each realization for each well. The realization that provided the least squares of error across all the wells was selected as a base case geomodel. Permeability correction coefficients were applied on the base case geomodel until PTA kh was acceptably matched. The resulting permeability log at the PTA well is referred to as a PTA corrected permeability log. Some cored wells were originally exempted from the neural network permeability modeling because they didn't have logs (sonic, density, and neutron logs). Hybrid permeability logs were derived from a combination of the predicted permeability logs and core permeability at these well locations.

All permeability correction logs (1) PTA corrected permeability logs, and (2) hybrid permeability logs, were then fed back into the geomodeling workflow to generate an improved permeability distribution, which respects core data, PTA kh , and CRRs.

The do-nothing simulation run has more than 80% of the wells' pressure data acceptably history matched. This application demonstrates that a-priori integration of dynamic elements like CRR, PTA kh , and the use of CRR-based permeability modeling results in a better characterized geomodel with the potential for eliminating the need for history matching.

Data Set Description

This carbonate field has two reservoir zones denoted from top to bottom as Res-y and Res-z. Available data includes static pressure and production data from several wells over several years. In addition, the following data was available:

- Six wells with both logs and core data.
- Ten wells with logs, but no core data.
- Five wells with core data, but no logs.
- Four wells with pressure transient analysis (PTA) results.
- Four wells with borehole image logs confirming the presence of fractures.

Methodology

Connected Reservoir Regions (CRRs)

All the shut-in pressures from all the wells were plotted on the same axis to identify trends and establish pressure groups. Some of the wells have historically produced from more than one reservoir, and so the static pressures

measured on such wells reflect the prevailing pressure on the reservoir in which it was producing at the time of measurement. To eliminate the influence of the zone of completion on a wells' static pressure trend, we separated the static pressure data by reservoir to see if there is lateral variation of the pressure trend, and by implication, variation of reservoir quality within each reservoir².

Figure 1 is a time-lapse plot of the average reservoir pressures for all wells in Res-y and Res-z. Within each reservoir, the static pressure trend is similar, but between reservoirs the trend shows differences. This implies that the individual reservoirs are disconnected, whereas within each reservoir, there is large-scale interwell connectivity. This pressure behavior is consistent with well logs and seismic information, which show a thick and continuous anhydrite layer between the two reservoirs. Each reservoir therefore constitutes a different connected reservoir region (CRR).

The axes of Fig. 1 and all subsequent plots in this article have been masked for data confidentiality reasons.

In addition, since the goal of the current article is to illustrate the merits of a methodology rather than the discussion of a case study, only the results from Res-z will be discussed.

CRR-based Permeability Modeling

There were six wells with both log and core data, 10 wells with logs but no core data, and finally, five wells with core data but no logs. Using approaches well documented in literature³⁻⁶, the permeability function was created based on the relationship between core and log data using only wells, which have both, and the resulting permeability function was then used to predict permeability as a function of log response for logged noncored wells. In the course of creating the permeability function, one well having both log and core data was left out of the training data set to be used for evaluating — blind test — the predictability of the resulting permeability function.

To improve the quality of permeability function, separate permeability functions were developed for each

CRR based on only data available within the CRR. This idea of implementing different permeability functions for reservoir regions that have geologic differences has been discussed⁴ earlier. The authors noted that well logs sometimes respond differently in different hydraulic zones, so different permeability functions should be developed for the different zones in such instances. For example, the amplitude of the sonic log corresponding to a porosity of 15% in a predominantly dolomitic environment could be significantly different from its magnitude in a predominantly calcitic environment. Therefore, if a permeability function based on the relationship between the core and log data from the calcite environment is used to predict permeability as a function of the log response in a dolomitic environment, results could be erroneous.

To illustrate the benefit of CRR-based permeability modeling, Fig. 2 shows the result for Res-z. Shown is the result of the permeability prediction for the blind test well, which has both log and core data, but was not used as part of the training data set. On one hand, all available core and log data — irrespective of the CRR — were used in deriving a single permeability function. On the other hand, a permeability function was derived for each CRR (in this case each CRR corresponds to individual reservoirs) using only the core and log data within the CRR. Afterward, these individual permeability functions were combined along the wells.

The red dots in Fig. 2 are the cored permeability data in the blind test well; the blue line is the prediction result of the single permeability function using all core and log data, and the black line is the prediction result from the CRR-based permeability function in which the core and log data have been grouped according to CRR. Clearly, the CRR-based permeability function gives a better prediction result for the blind test well on Res-z.

Although not shown here, the permeability prediction results were similarly better for Res-y when different permeability functions were built for each CRR.

Fig. 1 A time-lapse plot of the average reservoir pressures for all wells in Res-y and Res-z.

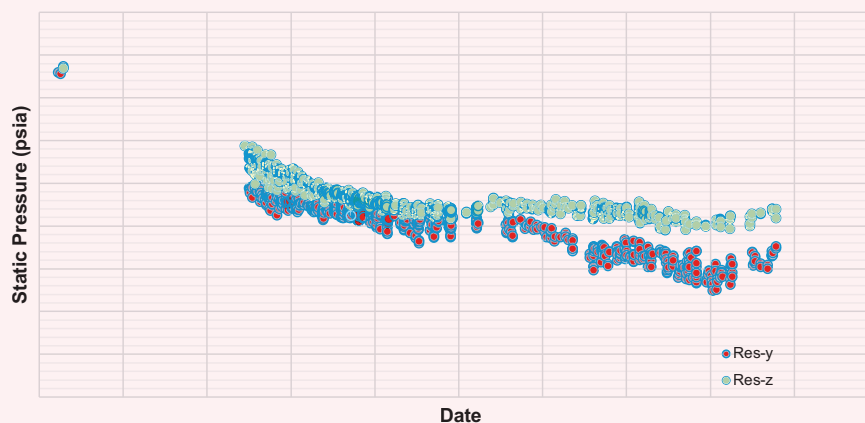
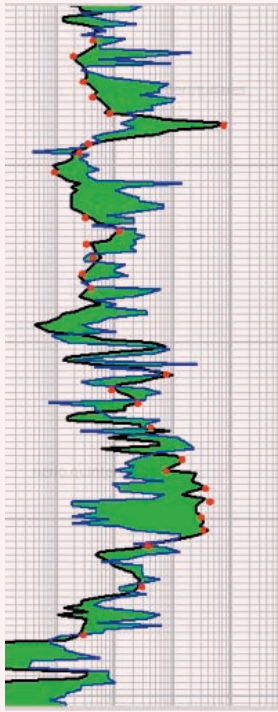


Fig. 2 Comparison of the permeability function prediction with core permeability within the Res-z interval of the blind test well — with CRR (black line) and without CRR (blue line).



Simulation Results Based on Initial 3D Geomodel (Case 1)

An initial geomodel realization (Case 1) was created using statistical distribution and variogram analysis results obtained from the available core data. Figure 3 shows the simulated field production rate based on the geomodel of case 1, which is less than the production rate that has been historically observed in the field. Figure 4 shows a plot of simulated and historical pressure data

for all wells in Res-z after the aquifer size and strength have been calibrated.

It is observed from Fig. 4 that the simulated pressures of the different wells within Res-z show a larger dispersion than suggested by the Res-z historical pressure data. Res-z historical pressure data shows that the wells within it are very connected, this is indicated by similar pressures measured from spatially separated wells at similar dates. The geomodel case 1 simulated pressures, however, show significant differences in pressure between neighboring wells on Res-z, and this indicates that the interwell connectivity in the geomodel case 1 is not consistent with the Res-z historical pressure data. Although not shown here, the interwell connectivity assessment for Res-y also shows a large dispersion of the wells' simulated pressure, indicating that the geomodel case 1 connectivity between the wells is not consistent with historical data.

One source of the poor interwell connectivity is the extrapolation of the permeability function beyond the lower limit of core data, thereby leading to the prediction of very low permeability values, which are later populated in 3D. To predict permeability at noncored wells using permeability function, the function should be created using log and core data covering all permeability ranges within the reservoir⁴. This implies that the permeability function should not be extrapolated beyond the limits of available core data. Another source of the poor interwell connectivity is non-inclusion of observed fractures in the case 1 geomodel.

Forward Integration of Dynamic Elements (Creation of Geomodel Case 2)

CRR-based Variogram

In certain cases, variogram lengths obtained from core data analysis may be biased by data availability. It is therefore advisable to ensure that the variogram used in geomodeling is large enough to ensure that connectivity is preserved within each CRR. In this example, another geomodel realization (case 2) was created by increasing the variogram range to half of

Fig. 3 Comparison of simulated and historical production rate showing that the case 1 geomodel production rate is less than the historical production rate.

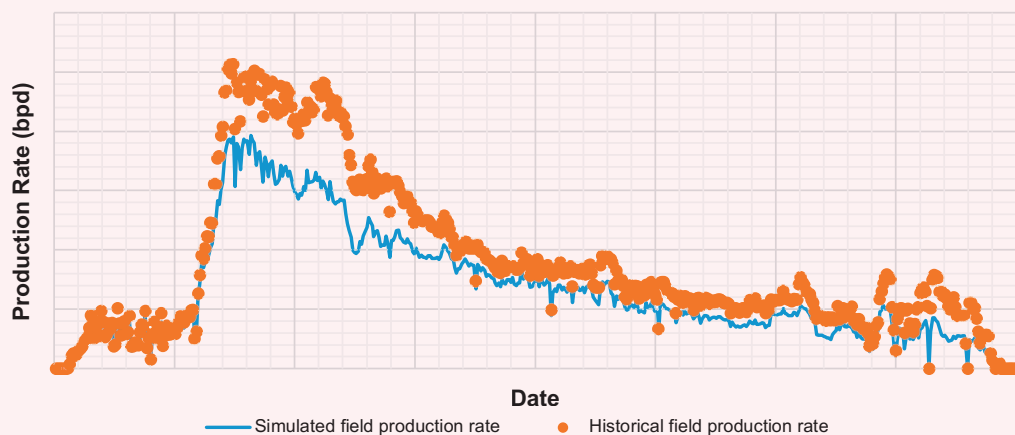


Fig. 4 The plots of simulated and historical pressure data for all wells in Res-z after the aquifer size and strength have been calibrated.

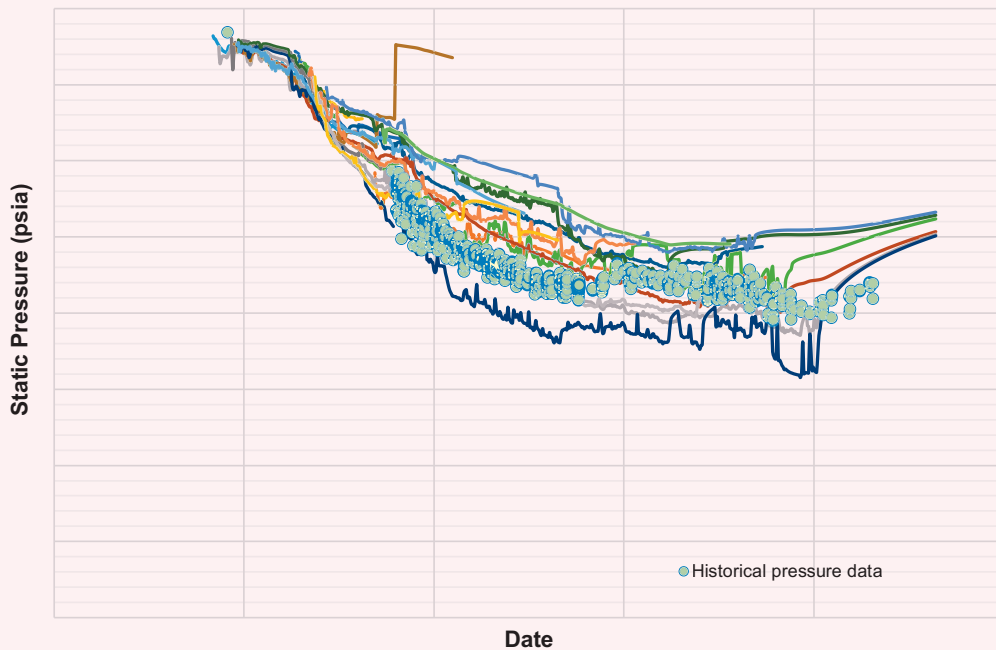
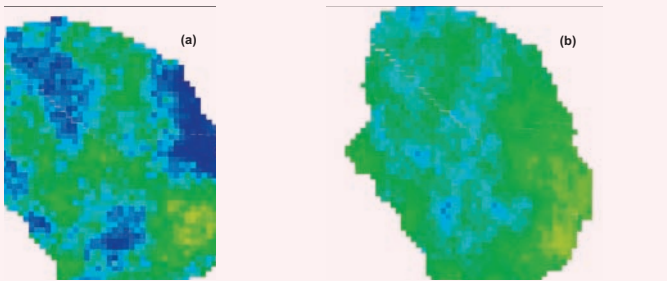


Fig. 5 (a) Permeability distribution based on the variogram length interpretation determined from limited cored data, and (b) permeability distribution based on a longer variogram range resulting in a better connected reservoir.



the maximum interwell distance for each reservoir. The goal was to ensure communication at large-scale between all wells within each reservoir as observed from the wells' historical pressure data. This is consistent with the work of earlier researchers⁷, which showed that a hydraulic unit is a reservoir zone that is laterally and vertically continuous and has similar permeability, porosity, and bedding characteristics.

Figures 5a and 5b compare the average permeability in Res-z for two scenarios of permeability distribution. Figure 5a, the geomodel case 1 permeability distribution scenario, is based on the variogram length interpretation from limited core data coverage, resulting in patches of permeability around the control wells. Figure 5b, the geomodel case 2 permeability distribution scenario, is

based on a longer variogram range resulting in a better connected reservoir.

Rank, Match, and Spread (RMS) Ranking

This is a novel approach for multiple realizations ranking based on multiple well pressure derivative matching⁸. There are four wells having PTA analysis results, and our goal is to determine which of the two geomodel realizations — case 1 and case 2 — gives the least error in predicting the permeability thickness (kh) seen by PTA at these well locations. For the purpose of illustration, Fig. 6 shows the comparison of the simulated pressure transient derivative with the observed pressure transient derivative for two of the four wells that have PTA.

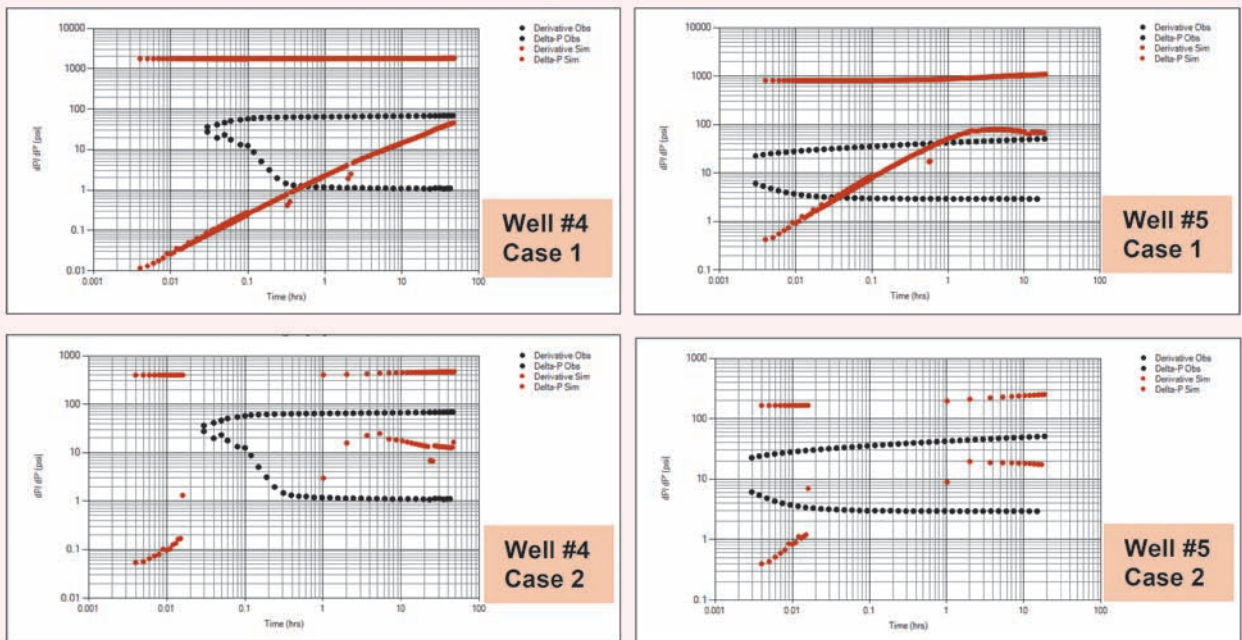
It is seen that at these well locations, geomodel case 2 shows the least mismatch error relative to the PTA kh . A kh mismatch error is based on comparison of the zero-slope section of pressure derivative plots. The model kh at the two PTA well locations are pessimistic compared to the PTA kh in both geomodel cases; nevertheless, case 2 shows the least mismatch error and further confirms the benefit of 3D permeability distribution using the CRR-based variogram range rather than the variogram range obtained from the analysis of limited core data.

Although not shown here, the remaining two PTA wells also show the least kh mismatch error on the case 2 geomodel.

Fracture Modeling

From available image logs, these reservoirs are known to be highly fractured. Beginning with geomodel case 2, a geomechanics-driven fracture model was developed for the reservoir intervals. The fracture model was based mainly on five components: (1) geomechanics structural

Fig. 6 The comparison of the simulated pressure transient derivative with the observed pressure transient derivative for two of the four wells that have PTA.



restoration, (2) paleo-stress inversion, (3) brittleness index classification, (4) borehole image interpretation, and (5) critical stress analysis. This process will allow us to drive the fracture intensity model and constrain the fracture permeability based on the current stress regime.

Borehole Image Interpretation. Four wells with borehole images were provided together with a full natural fracture description, including natural fracture type, dip angle, dip azimuth, and intensity at the well level. The apparent aperture was estimated by using a normalized image through deep resistivity response, resulting in a maximum aperture value of ~ 1.6 mm.

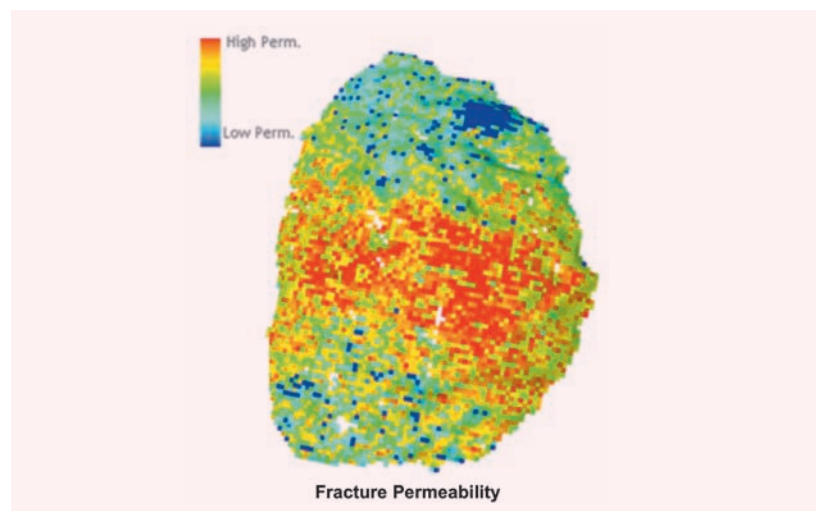
Rock Brittleness Property. Brittle materials, even those of high strength, absorb relatively little energy prior to fracture. In a complex heterogeneous fracture rock mass, the brittleness property can be modeled using a neural network classification using the elastic properties and stress regime producing the mechanical facies as inputs. Those mechanical facies have some correlation with the distribution of natural fractures, where this correlation can be evaluated using a histogram filtered by fracture density.

Paleo-Stress Analysis. The geomechanical restoration process was utilized to calculate the stress and strain of paleo stress deformation, analyzing each geological tectonic episode. This analysis distinguishes between fractures created by folding and those created by faulting processes. These processes are modeled using a geomechanical restoration and the paleo stress inversion method⁹.

Critical Stress Analysis. The in situ stress regime was modeled using Finite Element Model (FEM) techniques,

which can predict the stress/strain tensor regime using mechanical boundary elements. The maximum principal horizontal stress model and magnitude is obtained from this methodology for each cell of the 3D geocellular model. The critical stress concept criteria was then applied based on the Mohr Coulomb approach, which mainly depends on the stress magnitude/direction and fracture plane orientation. When shear stress exceeds shear stiffness, it results in dilation and hydraulically more permeable fractures⁶. Figure 7 shows that the highly

Fig. 7 The fluid flow path model shows a trending NNW-SSE direction.



conductive fracture or fluid flow paths is mainly trending in a NNW-SSE direction, and it has a conjugate direction trending in a NNE-SSW direction in accordance with the maximum stress direction.

Upon the introduction of the fracture model of Fig. 7 into geomodel case 2, the model kh significantly improved by the better match of the pressure derivative zero-slope line at the location of Well-4, Fig. 8. The blue curves are the log-log diagnostic plots based on the original case 2 geomodel, while the red lines are the diagnostic plots after the introduction of fractures and limiting the geomodel permeability to the observed core data minimum value.

Although not shown here, the kh match at other PTA well locations also improved significantly after the introduction of the fracture model, except for the Well-5 location, at which there are no fractures in the 3D model.

RMS Calibration. The goal of RMS calibration is to ensure an acceptable match of kh between the observed PTA data and the geomodel. After incorporating the fracture model into geomodel case 2, it was necessary to increase the fracture permeability by a factor of 2, to

obtain a kh — derivative zero-slope — match, Fig. 9. The location of Well-5 shows no fracture in the 3D model, and so a matrix permeability multiplier factor of 5 was used to match its derivative zero-slope. This resulted in a PTA corrected permeability log at the location of Well-5.

Hybrid Permeability Logs. There were five wells that have core porosity and permeability data that were not included in the workflow for generating the permeability function because they have no well logs. They were also not included in the 3D permeability distribution as control points.

The geomodel case 2 permeability log at these well locations was compared with their core data, and a hybrid permeability log was created for each of these wells, honoring the observed core data where applicable and the geomodel case 2 permeability log elsewhere.

Figure 10 shows the comparison between the geomodel case 2 permeability log and the hybrid permeability log for one of the five wells.

Summary of Additional Parameters Used for Creating a Case 2 Geomodel

1. The variogram range for permeability distribution was set to half of the maximum interwell distance to preserve connectivity within each CRR.
2. The hybrid permeability logs for the five cored but nonlogged wells were included as part of the control wells for 3D permeability distribution.
3. The case 2 permeability log for Well-5 was multiplied by the RMS calibration co-efficient of 5, and the PTA corrected permeability log was also included as part of the 3D permeability distribution control wells.
4. The case 2 geomodel permeability distribution was carried out using six additional control wells than what was used for case 1.
5. A fracture model was incorporated into case 2, and the fracture permeability was multiplied by a factor of 2 to ensure a match of the geomodel and PTA kh .
6. The minimum geomodel permeability was limited to core data value. This eliminated the low permeability predicted by extrapolation of the permeability

Fig. 8 Comparison of historical pressure transient derivative with the derivative of simulated pressure transient for case 2 — before (blue line) and after (red line) introduction of the fracture model.

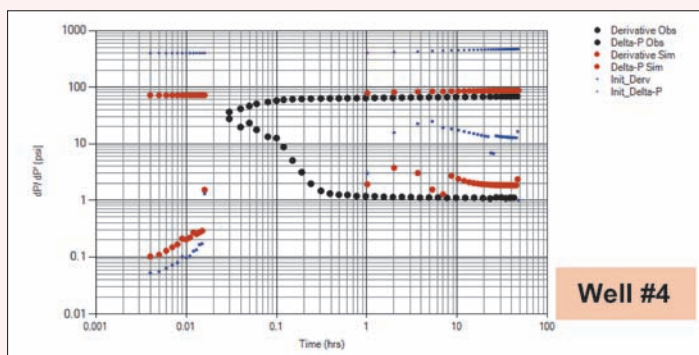


Fig. 9 Simulated kh matching with the observed kh after the fracture permeability of Well-4 was multiplied by 2 and the location matrix permeability of Well-5 was multiplied by 5.

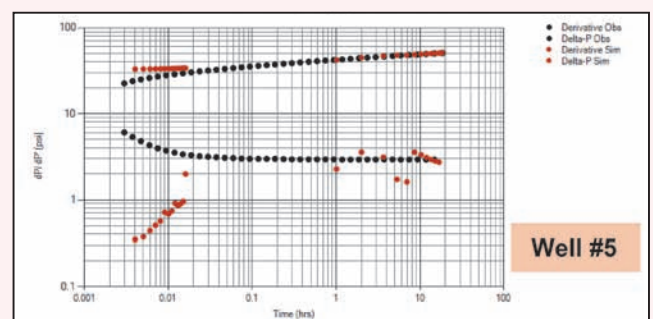
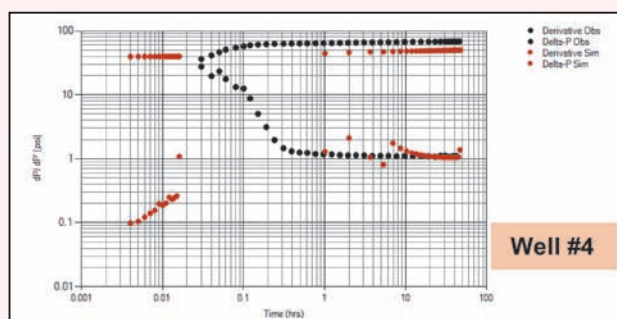
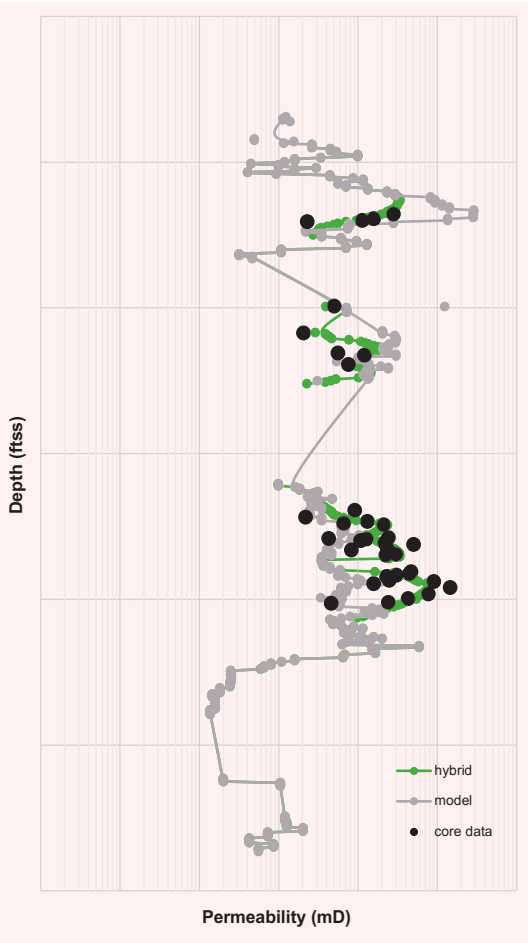


Fig. 10 The comparison between the geomodel case 2 permeability log and the hybrid permeability log for one of the five wells.



function, and which, when distributed in 3D, creates fictitious interwell barriers.

Simulation Result Based on Geomodel Case 2

Starting with the case 2 model, the aquifer strength and size were calibrated appropriately. In most cases, there would be no dynamic data from the aquifer zone to be used in a-priori calibration of the aquifer region. Therefore, the aquifer region will always be a region most susceptible to modifications during history matching. In this example, the simulated field production rate is now matching with the historical field production rate, Fig. 11. In addition, Fig. 12 shows that about 80% of the wells' simulated pressure was already matching their historical data prior to any history matching modifications. No further modifications were required within the hydrocarbon zones because several dynamic elements had already been pre-integrated into the geomodel case 2.

Although not shown here, after the pre-integration of dynamic data as earlier discussed, Res-y simulated well pressures are also reasonably matching the observed data, without any further history matching modifications.

Discussion of Results

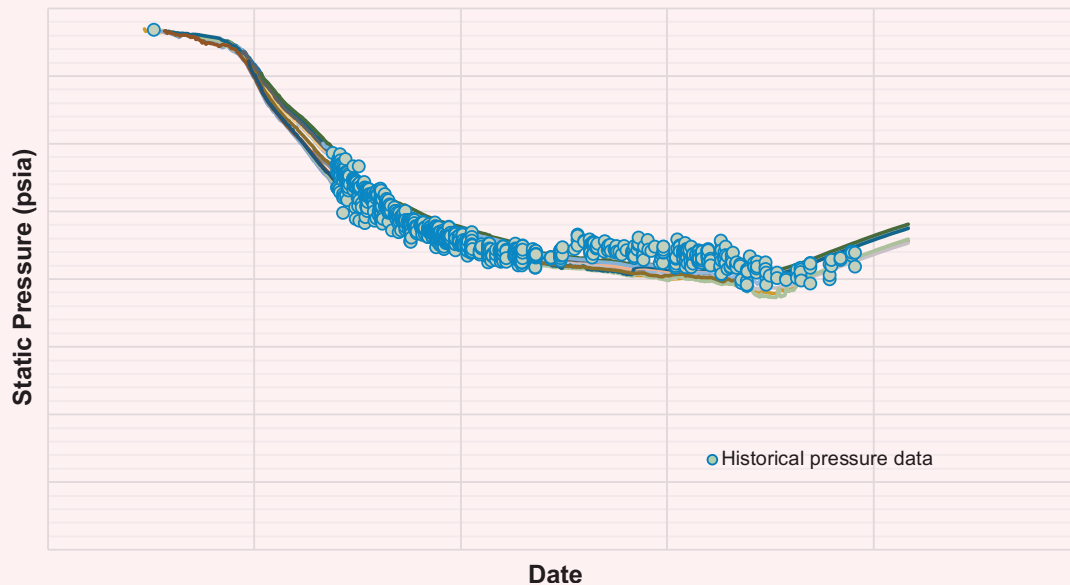
Creation of geomodel case 2 incorporates permeability corrections at the locations of six additional wells in the form of corrected logs, i.e., the PTA corrected permeability log, and the hybrid permeability log. Since the permeability corrections are not based on constant local multipliers around the wells, but are rather applied in the form of corrected permeability logs, the process gives rise to a smooth and geologically consistent permeability correction.

In certain cases, variogram lengths obtained from core data analysis may be biased by data availability. Therefore, it is advisable to ensure that the variogram

Fig. 11 The simulated field production rate matches the historical field production rate.



Fig. 12 In Res-z, approximately 80% of the wells' simulated pressure was already matching their historical data prior to any history matching modifications.



range used in geomodeling is large enough to ensure that the connectivity is preserved within the identified CRRs. As illustrated in Fig. 6, the kh predicted by geomodel case 1 is more pessimistic at all PTA well locations than in geomodel case 2.

Instead of applying well-by-well local modifications to history match the pressures of geomodel case 1 shown in Fig. 4, it was much easier, faster, and geologically consistent to pre-integrate dynamic information (understanding) into geomodel case 2, and thereby achieve a reasonably history matched model, without any further modifications within the hydrocarbon pore volume as shown in Fig. 12.

In summary, the goal of this article is not to discuss the methodology for history matching, rather, to show that history matching may not be required if dynamic data are properly integrated a-priori into geomodeling. The a-priori integrated data in this particular example includes:

- CRR-based variogram; Fig. 5a vs. Fig. 5b.
- CRR-based permeability modeling; Fig. 2.
- RMS calibration both fracture and matrix; Fig. 9.
- Hybrid permeability from wells having core data but no logs; Fig. 10.
- Interwell connectivity improvement by using a fracture model and setting the minimum model permeability equal to the minimum observed core permeability.

Conclusions

The current example shows that when the original geomodel has already been constrained to available dynamic elements, such as a geomechanical fracture

model, CRR, and kh from PTA, it is potentially possible to eliminate the need for history matching.

Acknowledgments

The authors would like to thank the management of Saudi Aramco for their support and permission to publish this article.

This article was presented at the International Petroleum Technology Conference, Beijing, China, March 26-28, 2019.

References

1. Kayode, B.O., Al-Saleh, M.A., Lyngra, S. and Al-Ghareeb, Z.M.: "Pressure Conditioned Modeling: Application of Time-Lapse Shut-in Pressure Data to Map Connected Reservoir Regions for Conditioning of 3D Geomodel Property Distributions," SPE paper 192204, presented at the SPE Kingdom of Saudi Arabia Annual Technical Symposium and Exhibition, Dammam, Saudi Arabia, April 23-26, 2018.
2. Kayode, B.O., Yaacob, M.R. and Abdullah, F.A.: "Connected Reservoir Regions Map Created from Time-Lapse Pressure Data Shows Similarity to Other Reservoir Quality Maps in a Heterogeneous Carbonate Reservoir," SPE paper 19163, presented at the International Petroleum Technology Conference, Beijing, China, March 26-28, 2019.
3. Georgi, D.T., Harville, D.G., Phillips, C. and Ostroff, G.M.: "Extrapolation of Core Permeability Data with Wireline Logs to Uncored Intervals," paper presented at the SPWLA 34th Annual Logging Symposium, Calgary, Alberta, Canada, June 13-16, 1993.
4. Johnson, W.W.: "Permeability Determination from Well Logs and Core Data," SPE paper 27647, presented at the Permian Basin Oil and Gas Recovery Conference, Midland, Texas, March 16-18, 1994.
5. Lacentre, P.E. and Carrica, P.M.: "A Method to Estimate Permeability on Uncored Wells Based on Well Logs and

- Core Data,” SPE paper 81058, presented at the SPE Latin America and Caribbean Petroleum Engineering Conference, Port-of-Spain, Trinidad and Tobago, April 27-30, 2003.
6. Rogers, S.F.: “Critical Stress-Related Permeability in Fractured Rocks,” *Geological Society London, Special Publications*, Vol. 209, January 2003, pp. 7-16.
 7. Hearn, C.L., Ebanks Jr., W.J., Tye, R.S. and Ranganathan, V.: “Geological Factors Influencing Reservoir Performance of the Hartzog Draw Field, Wyoming,” SPE paper 12016, presented at the SPE Annual Technical Conference and Exhibition, San Francisco, California, October 5-8, 1983.
 8. Kayode, B.O., Qahtani, G., Thawad, F. and Hage, A.: “Advances in Reservoir Modeling: A New Approach for Building Robust Reservoir Models,” SPE paper 187993, presented at the SPE Kingdom of Saudi Arabia Annual Technical Symposium and Exhibition, Dammam, Saudi Arabia, April 24-27, 2017.
 9. Maerten, F.: “Adaptive Cross Approximation Applied to the Solution of System of Equations and Post-Processing for 3D Elastostatic Problems Using the Boundary Element Method,” *Engineering Analysis with Boundary Elements*, Vol. 34, Issue 5, May 2010, pp. 483-491.

About the Authors

Babatope O. Kayode

*B.S. in Petroleum Engineering,
University of Ibadan*

Babatope O. Kayode is a Petroleum Engineer working with the Integrated Reservoir Studies Group in Saudi Aramco’s Reservoir Description & Simulation Department.

His previous work experience with SOWSCO Well Services Nigeria Ltd. involved the planning, supervision, and interpretation of pressure transient tests. Babatope also worked with Total Exploration and Production in Nigeria and in France, where he was involved in the construction and live updates of dynamic simulation

models. Babatope has 18 years of oil industry experience spanning Africa and Europe, and currently the Middle East. His research interest is in the area of developing workflows for faster and better history matching.

Babatope received his B.S. degree in Petroleum Engineering from the University of Ibadan, Nigeria, and he is currently in the final stages of completing an M.S. degree in Petroleum Engineering from Heriot-Watt University, Edinburgh, Scotland, U.K.

Otto E. Meza Carmargo

*B.S. in Geological Engineering,
University of San Marcos*

Otto E. Meza Carmargo joined Saudi Aramco in 2014 as a Geologist Engineer working in the Exploration Technical Services Department. He has 10 years of experience in the oil industry, and prior to joining Saudi Aramco, he worked in a variety of geological positions across the Middle East region, Brazil, Peru and the U.K. Otto’s experience includes several aspects of reservoir

characterization and integrated geomechanics modeling for conventional and unconventional reservoirs.

He received his B.S. degree in Geological Engineering from the University of San Marcos, Lima, Peru.

Nerio Quintero Tudares

*B.S. in Petroleum Engineering,
University of Zulia*

Nerio Quintero Tudares joined Saudi Aramco in 2014 as a Petroleum Engineer and is currently working as a Petrophysicist in the Advanced Petrophysical Modeling Group of the Reservoir Description and Simulation Department. He works on the development of reservoir integral studies of the major gas fields within the Kingdom.

Nerio has 19 years of experience in the oil and gas industry. Prior to joining Saudi Aramco, he worked as a Petrophysicist for Halliburton Formation and Reservoir

Solutions and Consulting Services in both conventional and unconventional oil and gas reservoirs, which included Venezuela, Colombia, Ecuador, Argentina, Congo, Egypt, Mexico, and the United States.

Nerio received his B.S. degree in Petroleum Engineering from the University of Zulia, Maracaibo, Venezuela, and his M.S. degree in Administration of Information Technology from Tecmilenio University, Monterrey, Mexico.

Shaikha S. Al-Dossary

*B.Eng. in Petroleum Engineering,
University of Leeds*

Shaikha S. Al-Dossary joined Saudi Aramco’s College Degree Program for Non-Employees in 2009. She has worked as a Reservoir Management Engineer, Petrophysicist, and Reservoir Simulation Engineer. In 2013, Shaikha joined Saudi Aramco as a Petroleum Engineer, working with the Event Solution Team in the Reservoir Simulations Division.

She served as the Society of Petroleum Engineers-

Kingdom of Saudi Arabia (SPE-KSA) Young Professional and Student Outreach Chairperson from 2016 to 2017.

In 2013, Shaikha received her B.Eng. degree in Petroleum Engineering from the University of Leeds, Leeds, U.K. Currently, she is at Imperial College London studying for her M.S. degree in Petroleum Engineering.

In Situ Pore Plugging Using Nanosilica-based Fluid System for Gas Shut-off

Prasad B. Karadkar, Dr. Ayman M. Al-Mohsin, Dr. Mohammed A. Bataweel, and Dr. Jin Huang

Abstract /

A nanosilica-based fluid system was evaluated for forming in situ glass-like material inside a matrix for permanent gas shut-off. This novel method involves two steps: first, pumping a low viscosity aqueous nanosilica mixture into the formation and allowing it to gel up, and second, gas production dehydrates nanosilica to form glass-like material inside the matrix. For this article, a nanosilica-based fluid system was assessed for pumping strategy and performance evaluation.

A nanosilica-based fluid system consists of a mixture of colloidal silica and activators. It possesses low viscosity, which assists in deeper penetration during placement. With time and temperature, it can lead to in situ gelation to form a rigid gel to block the pore space. Gas production can dehydrate nanosilica gel to form in situ glass-like material inside the formation porosity for permanent gas shut-off. The nanosilica-based fluid system was optimized using gelation tests and coreflooding tests to evaluate its performance under high-pressure, high temperature (HPHT) conditions. Formation of in situ glass-like material inside pores was analyzed using a scanning electron microscope (SEM).

The gelation time can be tailored by varying the activator type and concentration to match the field operation requirements. Kinetics of colloidal silica gelation at elevated temperatures showed faster viscosity buildup. Before gelation, the viscosity for the nanosilica-based fluid system was recorded as less than 5 centipoise (cP) at a 10 1/s shear rate, whereas the viscosity was increased more than 500 cP at a 10 1/s shear rate. Using core flow tests, nitrogen (N_2) gas permeability of the Berea sandstone core was completely plugged after pumping the 5 pore volumes (PVs) of nanosilica-based fluid system at 200 °F. During the nanosilica-based fluid system injection through the core, the differential pressure was increased to only 10 psi, showing better injectivity. The SEM images showed the presence of glass-like material filling the porosity, which showed in situ generation of glass-like material inside the pores.

The nanosilica-based fluid system has a low viscosity and can penetrate deeper into the formation matrix before transforming into a gel. Undesirable gas flow can dehydrate nanosilica gel to form in situ glass-like material inside the matrix for permanent sealing. This is environmentally friendly and can serve as an alternative to currently used conformance polymers for gas shut-off applications.

Introduction

Gas and water coning are used to describe the mechanism underlying the upward movement of water and/or the downward movement of gas into a producing well. Coning can seriously influence the well's productivity and influence the degree of depletion and the overall recovery efficiency of the oil reservoirs. Delaying production of gas and water are essentially the controlling factors in maximizing the field's ultimate oil recovery¹. Coning is primarily the result of the movement of reservoir fluids in the direction of least resistance, balanced by a tendency of the fluids to maintain gravity equilibrium. Gas coning tends to occur more easily than water coning because of the relatively low viscosity and high mobility of gas. Production with a high gas-oil ratio occurs because of high gas mobility in the formation². To maximize oil production from an oil well, the ability to shut off or reduce gas production becomes critical. The next challenge is to identify the gas entry point and to design an effective gas shut-off technique.

To minimize water production from oil/gas wells, a wide range of methods have been developed in the petroleum industry. For unwanted gas, shut off can be an additional application of water shut-off technologies. To select the right method to eliminate water/gas production, it is essential to understand the problem type. Generally, there are two main reasons of unwanted water/gas production, and these can be classified into either wellbore or reservoir related sources. The root cause of the wellbore source can be casing leaks, packer leaks, channels behind the casing, barrier breakdowns, or completions into or near the water zone³. In terms of a reservoir, related sources of water/gas production can be categorized as follows: channeling through high permeability streaks, fractures or fracture-like, bottom water and coning, poor areal sweep, and many more³⁻⁷.

Different technologies has been reported in the literature to tackle water and unwanted gas production. Kabir (2001)⁸ reviewed different current and emerging technologies for addressing water/gas shut-off, which can be

classified as mechanical, chemical, and microbiological. Different mechanical means can be used to shut off water/gas, e.g., tubing patch, casing patch, bridge plug, straddle packer, scab liner, and cement squeeze, which can provide a seal in the well's hardware and in large near wellbore openings. One of the major drawbacks to using the mechanical technique is the treatment limits in a wellbore. Water/gas shut-off offers advantages over mechanical shut-off, such as matrix treatment to maximize the success of the shut-off treatment and selective reduction of unwanted phase flow.

Kabir (2001)⁸ also summarized different chemical systems with their advantages and disadvantages such as inorganic gels, resins/elastomers, monomer systems, polymer gel, relative permeability modifiers, bio-polymers, viscous flooding, and foamed systems.

A careful selection of a technology for water/gas management requires in-depth analysis of the existing data with the purpose of understanding where and how water is produced. This will give an insight of identifying the proper solution/applicable treatment. When considering reservoir related problems, chemical treatments are the most appropriate solution as a water control agent. An effective choice and deployment of any such system is equally challenging as the objective of the job. Therefore, engineers must consider the technical aspect of the treatment like strength, depth, and stability requirements vs. the cost aspect, e.g., volume, type of treatment, concentrations and shut-in time⁹.

Selecting the right chemical treatment depends on the reservoir condition and properties like reservoir pressure, temperature, and salinity. Gel treatment, as a water control, has been proven a cost-effective technique^{10, 11}. There are two types of gels that were implemented as a conformance control agent, in situ gel and particle gels. Conventionally, in situ gels have been used for water control in the oil field to minimize undesired water production. This method consists of injecting a mixture of polymer, crosslinker and other additives, which is called a "gelant." The components of the gelant will start reacting under reservoir conditions such as temperature, salinity, pH, etc.), forming a gel to prevent water flow.

Particle gels are a new trend in the oil industry as water control materials, which is prepared at surface facilities. The gel has already been formed and cross-linked prior to injection, so the reservoir environments do not impact the gelation. These particle gels are a relatively new remedial treatment for excessive water production problems. This novel water control system can be adjusted according to formation pore throat sizes, particularly for deep profile control. Several researchers proposed particle technologies that can be implemented to homogenize reservoir and control excessive water production. These technologies include preformed sized particle gels^{10, 12}, pH sensitive gels^{13, 14}, bright water^{15, 16}, microgels and sub-microgels¹⁷. The unwanted gas production from zones that are not exposed for production can be treated with gel technology to shut off gas production¹⁸.

Research in the nano-science area and advancement of nanotechnology are progressing promptly. It can be seen

that their outcomes are now apparent and well established in several industries. Yet, even though nanotechnology is a somewhat new science, it already has abundant applications in our daily life, extending from consumer goods to medicine to improving the environment. Nowadays, the petroleum industry has been forthcoming in nanotechnology with excessive opportunities¹⁹. The properties of these advanced materials, i.e., lightweight, tiny size, mechanical strength, and thermal resistance, can be a game changer in several applications.

For example, the main goal of chemical enhanced oil recovery methods is to enhance the overall oil displacement efficiency via reducing the microscopic trapped oil in small pores due to capillary forces²⁰. Hendraningrat et al. (2013)²¹ reported that nanosilica could significantly increase oil recovery by modifying surface tension. Almohsin et al. (2018)²² used a graphene-based zirconium oxide nanocomposite as the crosslinker incorporated with polyacrylamide to enhance the thermal and mechanical stability. For water shut-off applications, nanoparticles have become an attractive solution^{23, 24}.

In this article, a nanosilica-based fluid system was assessed for gas shut-off application. A nanosilica-based fluid system consists of a mixture of colloidal silica and activators, which can lead to in situ gelation to form a rigid gel to block the pore space. Gas production can dehydrate nanosilica gel to form in situ glass-like material inside the formation porosity and will be demonstrated in this article. The nanosilica-based fluid system was optimized using gelation and coreflooding tests to evaluate its performance under high-pressure, high temperature (HPHT) conditions. Formation of in situ glass-like material inside pores was analyzed using a scanning electron microscope (SEM). The nanosilica-based fluid system has a low viscosity and can penetrate deeper into the formation matrix before transforming into a gel. Undesirable gas flow can dehydrate nanosilica gel to form in situ glass-like material inside the matrix for permanent sealing.

Experimental

Materials

The fluid system is comprised of nanosilica and an activator. A surface modified nanosilica particle solution was used to prepare a water/gas shut-off fluid system. It is aqueous dispersion of colloidal silica nanoparticles at a 40% concentration, which is slightly more viscous than water (< 5 centipoise (cP)). Being stabilized, the amorphous silica nanoparticles have a spherical shape and carry a negative surface charge. Sodium silicate (NaSil) was utilized as an activator to prepare the nanosilica-based fluid system.

Gelation Time

Gelation time is defined as the initial gelation time in which the nanosilica-based fluid system viscosity significantly increases. A reasonable "gelation time" must be realized to allow safe pumping operation of the fluid through the tubular and into the target zone. A HPHT rheometer was used to study the gelation time by varying the activator concentration at 200 °F. A freshly

prepared gel fluid (~52 mL) was placed in the cup and affixed to the rotor fixture on the rheometer. The sample was set at a constant shear rate at 10 s^{-1} on the smooth bob-sleeve (R1-B5), with 500 psi of nitrogen (N_2) gas applied pressure at a preset testing temperature.

Coreflooding Test

Coreflood experiments were conducted to evaluate the tendency and stability of the fluid system to shut off water/gas production in sandstone formations. The coreflooding setup was modified to bypass the nanosilica-based shut-off chemical system from the face of the core plug to make sure all the lines are clean during shut-in. Two back pressure regulators were used, one connected to the lines coming out through the core plug and another connected to the bypass core plug. The bypass regulator was used for both cleaning the injection side and to maintain constant pressure after chemical treatment. N_2 gas was used to flow through the core before chemical treatment to measure the initial permeability, and after chemical treatment to dehydrate the nanosilica-based fluid system to form a glass-like material inside the matrix.

Figure 1 is a schematic diagram of the coreflood setup. The core holder is accommodated in an oven at a constant temperature, which can hold the core plug at a mimicked reservoir temperature of 200 °F and a confining pressure of 2,500 psi. The pressure drop across the core plug was monitored using a set of differential pressure transmitters. The liquids were delivered using a high-pressure, high volume Quizix pump. N_2 gas was pumped through the core using a gas flow controller. The pore pressure was maintained at 500 psi using a back pressure regulator. Berea sandstone core plugs were used in this study.

SEM

A SEM was utilized to image the untreated core surface before coreflooding tests, and the treated core plug matrix after coreflooding tests. To analyze the core matrix, the core plug was broken down after the coreflooding tests. SEM images at different resolutions — 500 μm , 200 μm , and 100 μm — analyzed the formation of glass-like material on the treated core surface.

Results and Discussions

Mechanism of Nanosilica-based Fluid System Gelation and Formation of Glass-like Material

Figure 2 schematically illustrates the gelation mechanism/process of the nanosilica-based fluid: nanosilica transfer from a stable liquid to a strong gel upon the addition of an activator. The process can be roughly divided into the following consecutive steps: stabilization of silica nanoparticles, interaction of nanoparticles, and formation of chemical bonds. It should be noted that there are no distinct transitions between the steps, and the gelation will usually be observed and described as one process.

As indicated in Fig. 2a, nanosilica is a dispersion of discrete nonporous nanoparticles of amorphous silica (SiO_2). In the alkaline pH solution, anionic silica nanoparticles have high negative surface charges, which keeps the nanoparticles far apart due to the strong repulsion forces in between. Therefore, the initial colloidal suspension is very stable. When an activator (inorganic salts, acids, etc.) is introduced to the nanosilica suspension, the counter ions (Fig. 2b) reduces the repulsion barrier between the nanoparticles and brings the nanoparticles together. At this step, the nanoparticles just come into

Fig. 1 Schematic representation of the coreflooding setup.

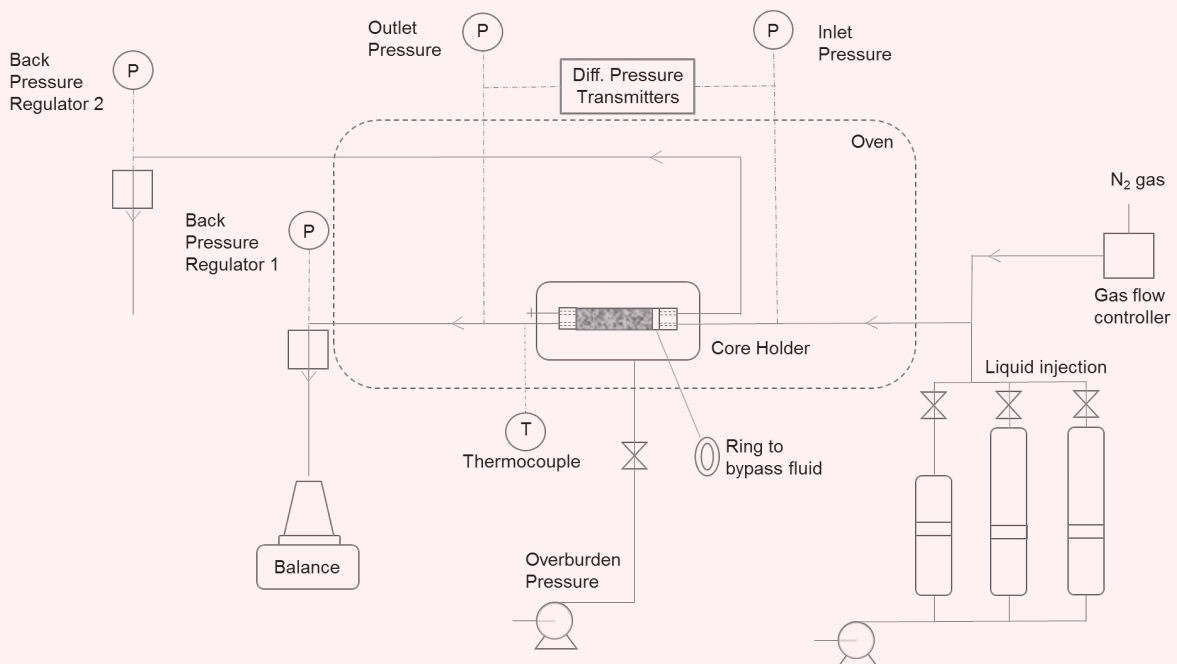
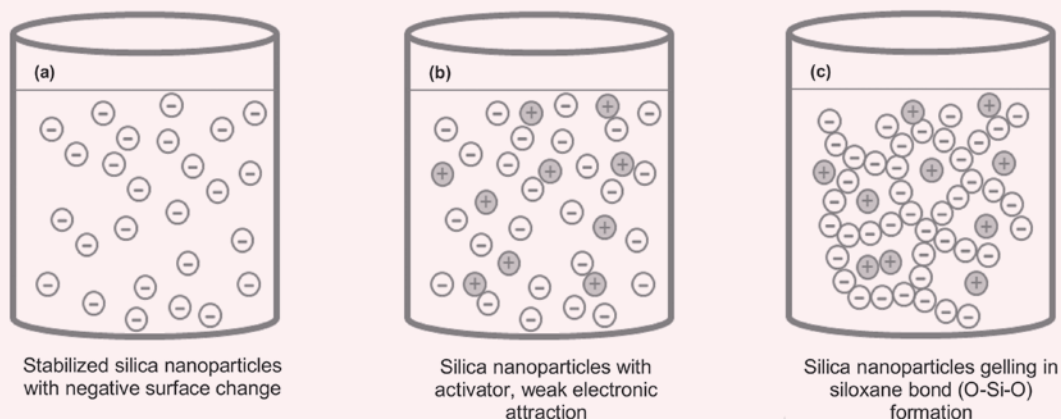


Fig. 2 Mechanism of nanosilica-based fluid system gelation.

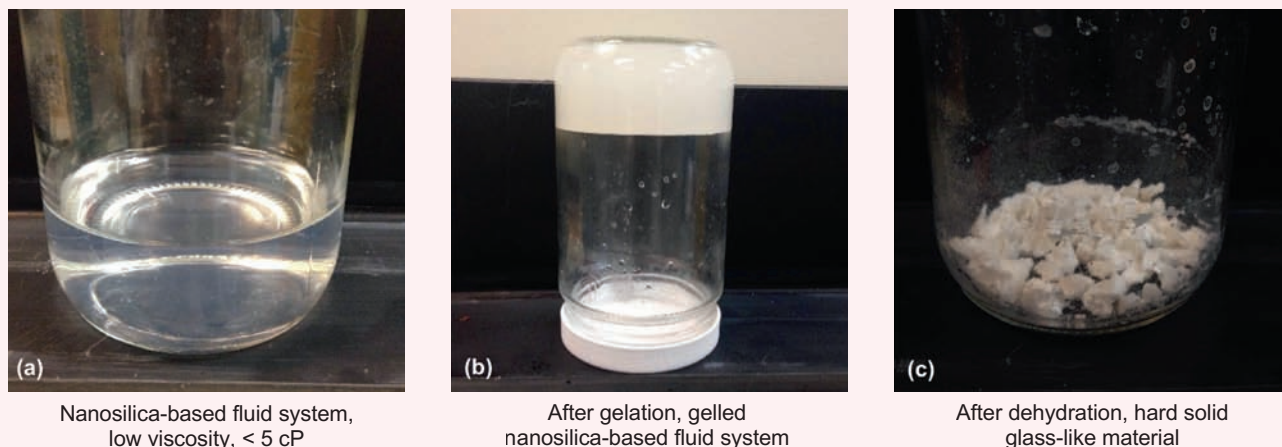


contact by weak electronic interaction, but there is no covalent bonds formed. In other words, only physical interaction exists in nanoparticles. The nanosilica liquid might start to deviate from the initial stable state, but still shows lower viscosity. Once the nanoparticles are close enough, they will collide with and adhere to each other through the formation of covalent bonds (siloxane bond, O-Si-O), Fig. 2c.

This initiates the gelation process. Further interacting and linking of more and more nanoparticles will lead to the formation of extended networks as the gelation process continues. The nanosilica fluid will show increased viscosity, which indicates the progression of gelation. Nanoparticles only aggregates or agglomerates at the earlier stage of gelation, causing a very slow increase of viscosity while at the later stage; one can visually observe the formation of solid gel as the fluid viscosity undergoes a rapid/accelerated increase.

A gelled silica nanoparticle can be dehydrated to form a glass-like material. Figures 3a to 3c shows the conversion of a low viscosity nanosilica and an activator solution into a glass-like material. Figure 3a shows the mixture of nanosilica and an activator, at room temperature with a low viscosity — < 5 cP. The low viscosity mixture can assist in placing a nanosilica-based shut-off fluid deeper inside the formation. After placement, the low viscous mixture converts to a gel to plug the pore space over time, using the natural temperature of the reservoir. The time when the mobility/flowability of the fluid is totally lost can be considered as “gelation time” for the nanosilica fluid. Figure 3b shows the silica nanoparticles as a solid gel after the gelation step. To demonstrate the formation of glass-like material, the silica nanoparticle solid gel was dehydrated, Fig. 3c. Gas flow inside the reservoir can dehydrate solid silica gel inside pore spaces to form in situ glass-like material for permanent pore plugging.

Fig. 3 Formation of glass-like material from the nanosilica-based fluid system gelation.



Gelation Time Study

The gelation time was optimized with varying an activator concentration to build the viscosity at 200 °F. The gelation time can be more precisely determined from the viscosity time curve derived from the rheology tests. The viscosity development of nanosilica shows a typical “hockey stick” shape. This means the first part of the viscosity curve has a rather constant and low viscosity while the second part shows a rapid increase in viscosity. Gelation time is pinned as the turning point of the curve, indicating the fluid transit from liquid to solid gel. It should be noted that after the gelation time point, the viscosity grows exponentially, and the strengthening and reinforcement of the chemical bonds continues. The complete gelation could be a very long process and is strongly temperature dependent.

Figure 4 shows the nanosilica-based fluid system gelation time curves at different activator concentrations at 200 °F. In this study, NaSil was used to optimize gelation time. With an increase in the activator concentration, a decrease in gelation time was observed. At a lower activator concentration of 21% to 23%, a decrease in the gelation time was less sensitive to the activator concentration while at higher activator concentrations, 24% and 25%, the gelation time was found to be more sensitive.

During some of the gelation time tests, the initial viscosity was recorded before gelation because of the viscometer’s limitation to read low viscosity. To account for this instrument error, viscosity above 50 cP at 10 1/s

is considered the gelation time. Table 1 lists the gelation time at different activator concentrations at 200 °F.

Figure 5 shows the gelation time plotted at different activator concentrations. The curve is a second-degree polynomial fit, which shows at higher activator concentrations — 24% and 25% — that the gelation time varied in a narrow range. Based on the gelation time study, 21.5 wt% NaSil activator concentration was formulated for a coreflooding study for further investigation.

Table 1 Gelation time at different activator concentrations at 200 °F.

Nanosilica Concentration (wt%)	Activator, NaSil Concentration (wt%)	Gelation Time (min) 50 cP at 10 1/s
79	21	490
78.5	21.5	391
78	22	252
77	23	210
76	24	129
75	25	125

Fig. 4 The gelation time at different activator concentrations at 200 °F.

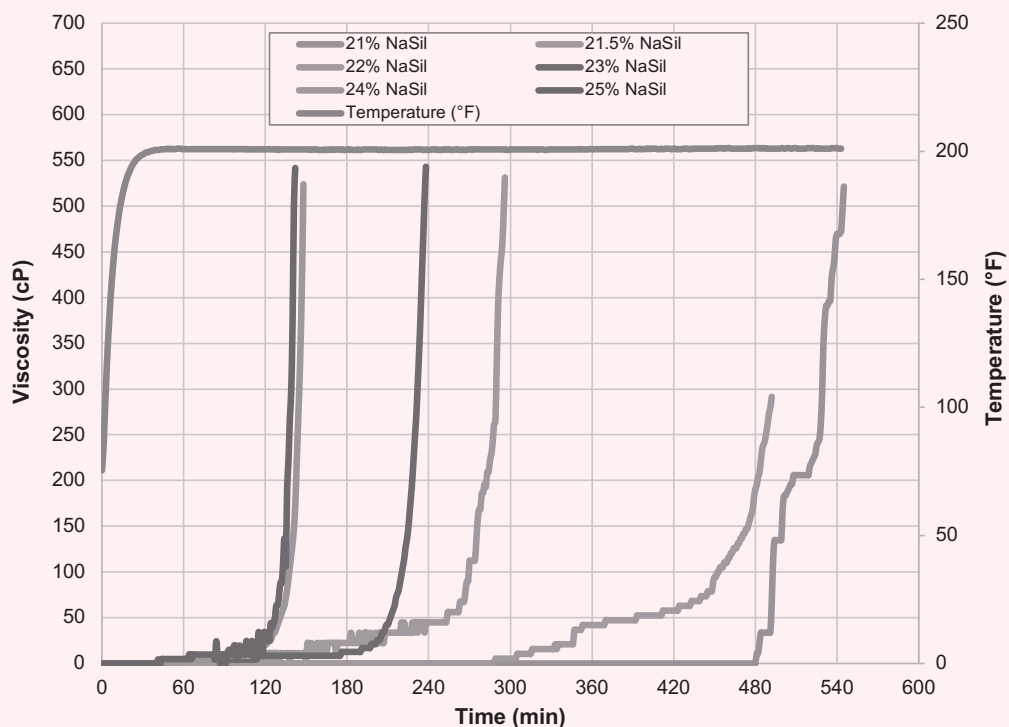
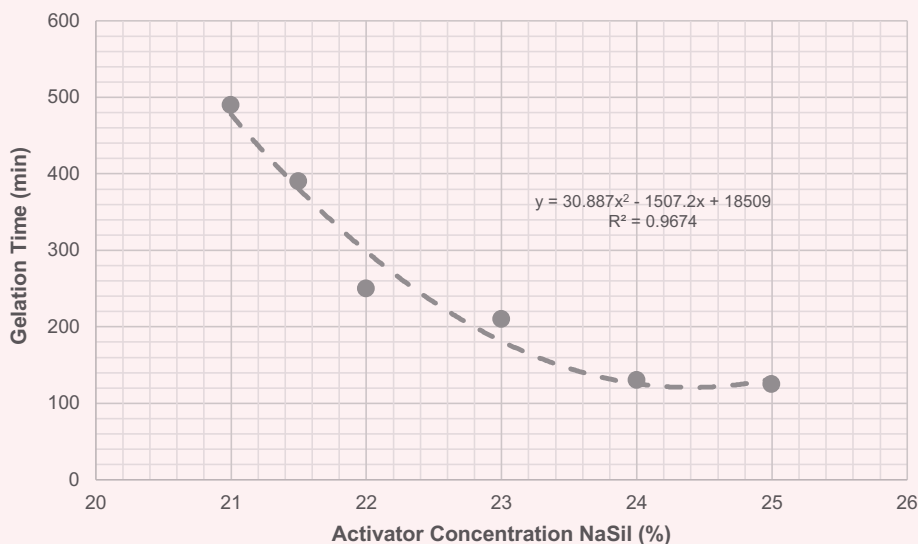


Fig. 5 The gelation time plotted at different activator concentrations at 200 °F.



Coreflooding Study

Coreflooding experiments were conducted to assess the injectivity of the treatment into the formation and the ability of the nanosilica-based fluid system for both water shut-off and gas shut-off applications. To accomplish that, the coreflooding experiments were run in different modes of operation. In the first stage, the base permeability was measured using N_2 gas and the preflush fluid containing the clay stabilizer and surfactant at a constant flow rate. This was followed with the main treatment injection containing the nanosilica-based fluid system with close monitoring of the pressure drop across the core. After that, the coreflooding was stopped to allow the chemical to cure and build the required mechanical strength for 24 hours.

The initial injectivity after the chemical curing is to assess the ability to shut off the treated matrix. This was followed with endurance testing by exposing the core plug to high differential pressure for an extended period to make sure that the shut-off material will not fatigue with time. The preflush fluid was used to measure initial injectivity and endurance testing after curing. In the last stage, N_2 gas was pumped to dehydrate the nanosilica-based fluid system to form in situ glass-like material for permanent pore plugging.

Figure 6 shows the coreflooding results using a nanosilica fluid system at 200 °F.

Initial Permeability

A Berea sandstone plug having 24% porosity was used in this work. The absolute permeability, pore volume (PV), and porosity of the core were determined by routine core analysis. The N_2 gas permeability, 370 md, was measured before preflushing the brine injection at 200 °F. The N_2 gas was injected at a different rate to measure the average gas permeability. After the N_2 gas initial permeability,

preflushing brine containing water, a surfactant at 0.2 vol%, and a clay control agent at 0.2 vol%, was injected at 2 ml/min and 1 ml/min rate and was measured as 190 md brine permeability. The differential pressure across the core plug was less than 0.5 psi under gas and brine injection, Fig. 6.

Chemical Injection

A nanosilica fluid system consisting of 0.2 vol% surfactant, 0.2 vol% clay control agent, 78.5 wt% nanosilica, and 21.5 wt% was injected at a rate of 1 ml/min at 200 °F. During this stage, 5 PV of chemical was injected in 2 hours. In Fig. 6, a small plot was inserted to zoom pressure response during the chemical injection. During the chemical injection, only a 10-psi increase in pressure was observed with 5 PV injection.

This slight increase in pressure was expected due to a slight increase in viscosity of the nanosilica fluid system. It is also expected that Ca^{+} from the sandstone core can cause in situ gelation. After chemical injection, the coreflooding experiment was stopped for 24 hours shut-in time. This was to allow the nanosilica fluid system to gel and build the required mechanical strength inside the pore structure. Before shut-in, all the lines, except lines going through core holder, were flushed with brine to avoid gelling of the nanosilica fluid system in the tubulars.

Endurance Testing

To test the robustness of the nanosilica fluid system, brine was pumped from the injection side of the core under a constant rate 1 ml/min rate. A sudden increase in differential pressure 1,400 psi was observed, Fig. 6, this shows complete pore plugging. To measure the durability of the shut-off treatment, the bypass back pressure regulator was adjusted to 2,500 psi and continued pumping with 1 ml/min from the injection side for 8 hours.

Fig. 6 The coreflooding results using a nanosilica fluid system at 200 °F.

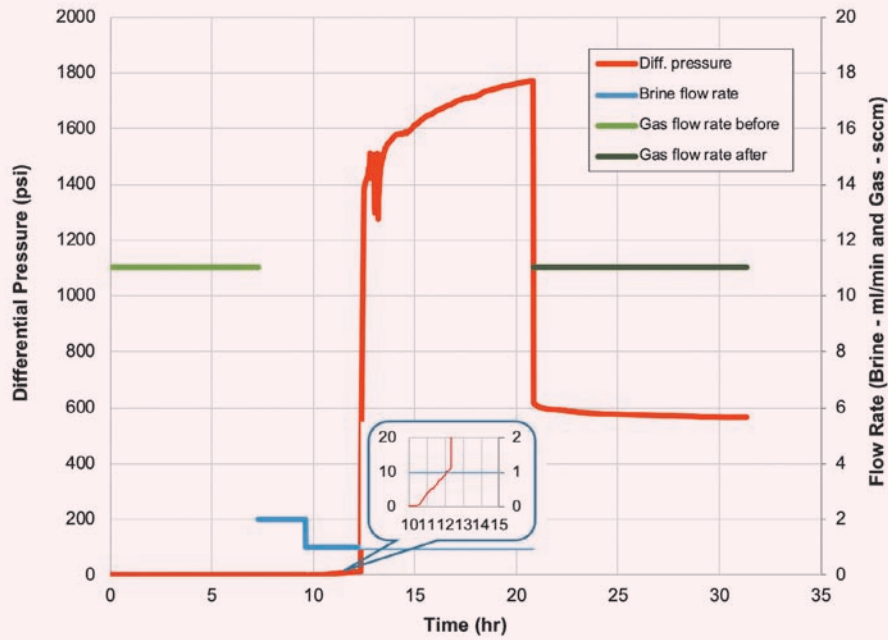
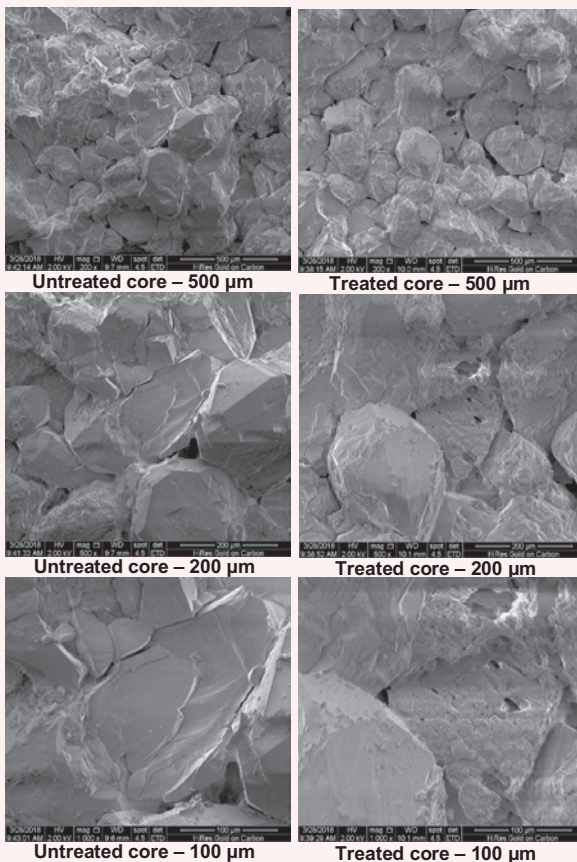


Fig. 7 SEM images of the untreated and treated core surface at different resolutions; the treated core showed formation of glass-like material.



On the other side of the core holder, zero brine flow or zero weight gain on balance confirms that the complete pore was packed with the nanosilica fluid system. This shows that the nanosilica fluid system can be used for water shut-off applications. Moreover, to explore the usability of the nanosilica fluid system for gas shut-off application, N_2 gas was flowed after brine injection. The injection side pressure of 600 psi was maintained using the bypass back pressure regulator. N_2 gas was bypassed for 10 hours, and no gas flow was observed on the other side of the core holder.

Characterizing In Situ Glass-like Material

Many published authors have used a SEM in characterizing the petrophysical properties of rock²⁵⁻²⁷. After the coreflooding tests, the core plug was broken down and the surface of the pore structure was imaged by using a SEM. The glass-like material was prepared by batch mixing for the nanosilica fluid system, while a similar material was seen inside the pore structure of the treated core plug. An untreated core was utilized from the same core block to compare the formation of in situ glass-like material.

Figure 7 shows SEM images of the untreated and treated core surface at different resolutions — 500 μm , 200 μm , and 100 μm . The untreated core surface looks smooth and shiny, while the treated core surface looks rough; showing the formation of glass-like material at all three resolutions.

Conclusions

The nanosilica-based fluid system was effectively investigated for a gas shut-off application. It possesses low viscosity and can penetrate deeper into the formation

matrix before transforming into a gel. Undesirable gas flow can dehydrate nanosilica gel to form in situ glass-like material inside the matrix for permanent sealing. The following conclusions can be drawn based on this investigation:

- Based on the gelation time study, the viscosity of the nanosilica-based fluid system grows exponentially with the continuation of strengthening and reinforcement of covalent bonds — O-Si-O.
- During the treatment design, the gelation time must be optimized for safe pumping operation of the fluid through the tubular and into the target zone. In this study, with different activator concentrations, gelation time was optimized from 125 to 490 minutes.
- The coreflooding experiment evaluates the injectivity and water shut-off and gas shut-off ability of the nanosilica-based fluid system. A low viscous nanosilica-based fluid system showed only a 10-psi increase in pressure with an injection of 5 PV. After shut-in, both brine and N₂ gas could not flow through the core plug, showing complete core plugging.
- The SEM images of the broken core surface showed the presence of glass-like material inside the core matrix.

Acknowledgments

The authors would like to thank the management of Saudi Aramco for their support and permission to publish this article. The authors would also like to thank Tamim Shehri for conducting the lab experiments and Wengang Li for conducting the SEM analysis.

This article was accepted for presentation at the Abu Dhabi International Petroleum Exhibition and Conference, Abu Dhabi, UAE, November 11-14, 2019.

References

1. Ahmed, T.: "Gas and Water Coning," in *Reservoir Engineering Handbook*, Chapter 9, 4th edition, Gulf Professional Publishing, January 2010, 1472 p.
2. Al-Dhafaeri, A.M., Nasr-El-Din, H.A., Al-Mubarak, H.K. and Al-Ghamdi, J.: "Gas Shut-off Treatment in Carbonate Reservoir for Oil Wells in Saudi Arabia," SPE paper 114323, presented at the SPE Annual Technical Conference and Exhibition, Denver, Colorado, September 21-24, 2008.
3. Joseph, A. and Ajiienka, J.A.: "A Review of Water Shut-off Treatment Strategies in Oil Fields," SPE paper 136969, presented at the Nigeria Annual International Conference and Exhibition, Tinapa-Calabar, Nigeria, July 31-August 7, 2010.
4. Flores, J.G., Elphick, J.J., Lopez, F. and Espinel, P.: "The Integrated Approach to Formation Water Management: From Reservoir Management to the Protection of the Environment," SPE paper 116218, presented at SPE Annual Technical Conference and Exhibition, Denver, Colorado, September 21-24, 2008.
5. Seright, R.S., Lane, R.H. and Sydansk, R.D.: "A Strategy for Attacking Excess Water Production," *SPE Production & Facilities*, Vol. 18, Issue 3, August 2003, pp. 158-169.
6. Kabir, A.H., Bakar, M.A., Salim, M.A., Othman, M., et al.: "Water/Gas Shut-off Candidates Selection," SPE paper 54357, presented at the SPE Asia Pacific Oil and Gas Conference and Exhibition, Jakarta, Indonesia, April 20-22, 1999.
7. Thomas, F.B., Bennion, D.B., Anderson, G. and Meldrum, G.: "Water Shut-off Treatments — Reduce Water and Accelerate Oil Production," PETSOC paper 98-47, presented at the Annual Technical Meeting, Calgary, Alberta, Canada, June 8-10, 1998.
8. Kabir, A.H.: "Chemical Water and Gas Shut-off Technology — An Overview," SPE paper 72119, presented at the SPE Asia Pacific Improved Oil Recovery Conference, Kuala Lumpur, Malaysia, October 6-9, 2001.
9. Hardy, M., van Batenburg, D. and Botermans, W.: "Improvements in the Design of Water Shut-off Treatments," SPE paper 38562, presented at the Offshore Europe Conference, Aberdeen, U.K., September 9-12, 1997.
10. Bai, B., Wei, M. and Liu, Y.: "Field and Lab Experience with a Successful Preformed Particle Gel Conformance Control Technology," SPE paper 164511, presented at the SPE Production and Operations Symposium, Oklahoma City, Oklahoma, March 23-26, 2013.
11. Almohsin, A.M., Bai, B., Imqam, A.H., Wei, M., et al.: "Transport of Nanogel through Porous Media and Its Resistance to Water Flow," SPE paper 169078, presented at the SPE Improved Oil Recovery Symposium, Tulsa, Oklahoma, April 12-16, 2014.
12. Bai, B., Liu, Y., Coste, J.-P. and Li, L.: "Preformed Particle Gel for Conformance Control: Transport Mechanism through Porous Media," SPE paper 89468, presented at the SPE/DOE Symposium on Improved Oil Recovery, Tulsa, Oklahoma, April 17-21, 2004.
13. Al-Anazi, H.A. and Sharma, M.M.: "Use of a pH Sensitive Polymer for Conformance Control," SPE paper 73782, presented at the International Symposium and Exhibition on Formation Damage Control, Lafayette, Louisiana, February 20-21, 2002.
14. Huh, C., Choi, S.K. and Sharma, M.M.: "A Rheological Model for pH-Sensitive Ionic Polymer Solutions for Optimal Mobility Control Applications," SPE paper 96914, presented at the SPE Annual Technical Conference and Exhibition, Dallas, Texas, October 9-12, 2005.
15. Pritchett, J., Frampton, H., Brinkman, J., Cheung, S., et al.: "Field Application of a New In-Depth Waterflood Conformance Improvement Tool," SPE paper 84897, presented at the SPE International Improved Oil Recovery Conference in Asia Pacific, Kuala Lumpur, Malaysia, October 20-21, 2003.
16. Frampton, H., Morgan, J.C., Cheung, S.K., Munson, L., et al.: "Development of a Novel Waterflood Conformance Control System," SPE paper 89391, presented at the SPE/DOE Symposium on Improved Oil Recovery, Tulsa, Oklahoma, April 17-21, 2004.
17. Zaitoun, A., Tabary, R., Rousseau, D., Pichery, T.R., et al.: "Using Microgels to Shut off Water in a Gas Storage Well," SPE paper 106042, presented at the International Symposium on Oil Field Chemistry, Houston, Texas, February 28-March 2, 2007.
18. Jain, P., Sharma, V., Raju, A.V. and Patra, S.K.: "Polymer Gel Squeeze for Gas Shut-off, Water Shut-off and Injection Profile Improvement in Bombay High Pilot Wells," SPE paper 64437, presented at the SPE Asia Pacific Oil and Gas Conference and Exhibition, Brisbane, Australia, October 16-18, 2000.
19. Cocuzza, M., Pirri, F., Rocca, V. and Verga, F.: "Is the Oil Industry Ready for Nanotechnologies?" paper presented at the Offshore Mediterranean Conference and Exhibition, Ravenna, Italy, March 23-25, 2011.

20. Lau, H.C., Yu, M. and Nguyen, Q.P.: "Nanotechnology for Oil Field Applications: Challenges and Impact," SPE paper 183301, presented at the Abu Dhabi International Petroleum Exhibition and Conference, Abu Dhabi, UAE, November 7-10, 2016.
21. Hendraningrat, L., Li, S. and Torsater, O.: "Effect of Some Parameters Influencing Enhanced Oil Recovery Process Using Silica Nanoparticles: An Experimental Investigation," SPE paper 165955, presented at the SPE Reservoir Characterization and Simulation Conference and Exhibition, Abu Dhabi, UAE, September 16-18, 2013.
22. Almohsin, A.M., Alabdulmohsen, Z., Bai, B. and Neogi, P.: "Experimental Study of Crude Oil Emulsion Stability by Surfactant and Nanoparticles," SPE paper 190440, presented at the SPE EOR Conference at Oil and Gas West Asia, Muscat, Oman, March 26-28, 2018.
23. Huang, J., Al-Mohsin, A.M., Bataweel, M., Karadkar, P., et al.: "Systematic Approach to Develop a Colloidal Silica-based Gel System for Water Shut-off," SPE paper 183942, presented at the SPE Middle East Oil and Gas Show and Conference, Manama, Kingdom of Bahrain, March 6-9, 2017.
24. Almohsin, A., Huang, H., Karadkar, P. and Bataweel, M.: "Nanosilica-based Fluid System for Water Shut-off," WPC paper 22-0468, presented at the 22nd World Petroleum Congress, Istanbul, Turkey, July 9-13, 2017.
25. Suri, Y.: "Predicting Petrophysical Properties Using SEM Image," SPE paper 144434, presented at the SPE Reservoir Characterization and Simulation Conference and Exhibition, Abu Dhabi, UAE, October 9-11, 2011.
26. Bonnie, J.H.M. and Fens, T.W.: "Porosity and Permeability from SEM-based Image Analysis of Core Material," SPE paper 23619, presented at SPE Latin America Petroleum Engineering Conference, Caracas, Venezuela, March 8-11, 1992.
27. Robin, M., Combes, R. and Rosenberg, E.: "Cryo-SEM and ESEM: New Techniques to Investigate Phase Interactions within Reservoir Rocks," SPE paper 56829, presented at the SPE Annual Technical Conference and Exhibition, Houston, Texas, October 3-6, 1999.

About the Authors

Prasad B. Karadkar

*M.S. in Chemical Engineering,
Nagpur University*

Prasad B. Karadkar is a Petroleum Engineer with the Production Technology Team of Saudi Aramco's Exploration and Petroleum Engineering Center – Advanced Research Center (EXPEC ARC). Prior to joining Saudi Aramco in April 2016, he worked as a Senior Technical Professional for Halliburton for 9 years. Prasad's areas of expertise include developing new fluid systems in the area of hydraulic fracturing,

acidizing, diversion, and water shutoff.

He has authored and coauthored 16 papers, published one patent, and has several patent applications in process.

In 2003, Prasad received his B.S. degree in Chemical Engineering from Shivaji University, Kolhapur, India, and in 2007, he received his M.S. degree in Chemical Engineering from Nagpur University, Nagpur, India.

Dr. Ayman M. Al-Mohsin

*Ph.D. in Petroleum Engineering,
Missouri University of Science
and Technology*

Dr. Ayman M. Al-Mohsin has worked with Saudi Aramco since 2014 as a Research Engineer. His research focuses on developing materials to prevent/reduce excess water and gas production during oil recovery.

Ayman received his B.S. degree in Mechanical

Engineering from the University of New Haven, West Haven, CT; his M.S. degree in Petroleum Engineering from New Mexico Tech, Socorro, NM; and his Ph.D. degree in Petroleum Engineering from Missouri University of Science and Technology, Rolla, MO.

Dr. Mohammed A. Bataweel

*Ph.D. in Petroleum Engineering,
Texas A&M University*

Dr. Mohammed A. Bataweel is a Champion for the Smart Fluid focus area in the Production Technology Division of Saudi Aramco's Exploration and Petroleum Engineering Center – Advanced Research Center (EXPEC ARC). He has led his team in the development and deployment of several in-house technologies in Saudi Aramco fields. Throughout his career, Mohammed has represented his department on several field development, asset, and multidisciplinary teams. His research interests include formation damage due to drilling and completion fluids, investigation and mitigation of injectivity decline, conformance control, sand production prediction, special core analysis, chemical enhanced oil recovery, productivity enhancement technologies, visualization of fluid flow

in porous media, and oil field chemicals.

Mohammed is an active member of the Society of Petroleum Engineers (SPE) where he has served on several conferences. He initiated and co-chaired several SPE advanced technical workshop series in the region. Mohammed has published more than 40 SPE papers in local and international conferences and refereed journals.

He received his B.S. degree in Mechanical Engineering from King Fahd University of Petroleum and Minerals (KFUPM), Dhahran, Saudi Arabia, and his M.S. degree in Petroleum Engineering from Harriot-Watt University, Edinburgh, U.K. Mohammed received his Ph.D. degree in Petroleum Engineering from Texas A&M University, College Station, TX.

Dr. Jin Huang

*Ph.D. in Inorganic Chemistry,
University of Houston*

Dr. Jin Huang is a Petroleum Scientist working with the Production Technology Division of Saudi Aramco's Exploration and Petroleum Engineering Center – Advanced Research Center (EXPEC ARC). Her current research interests are water management related oil field chemistry.

Prior to joining Saudi Aramco in 2015, Jin worked as with Weatherford Laboratories Inc. and Intertek Westport Technology Center in Houston, Texas. She was intensively involved in reservoir fluids analysis,

drilling fluid analysis and water chemistry. Jin also worked at GTC Technology Inc. in Houston as a Process Chemist, and worked as a postdoctoral researcher at Texas A&M University, College Station, Texas.

In 1994, Jin received her B.S. degree in Polymer Chemistry from Tianjin University, Tianjin, China; and in 2004, she received her Ph.D. degree in Inorganic Chemistry from the University of Houston, Houston, Texas.

Integrated NMR Fluid Characterization Guides Stimulation in Tight Sand Reservoirs

Endurance Oziegbe Ighodalo, Dr. Gabor G. Hursan, John McCrossan, and Ali R. Al-Balawi

Abstract /

Unconventional tight reservoir sands have low porosity and very low permeability (mostly less than 0.1 md) due to their fine grain size and poor grain sorting that is often exacerbated by extensive diagenetic effects such as cementation and compaction. Petrophysical evaluation in these formations is very challenging. Conventional downhole logs such as density, neutron, sonic, gamma ray, and resistivity measurements provide limited information on pore size variations and often miss key geological features, especially at the early stages of reservoir development. Fluid characterization at the earliest possible stage is paramount to guide the development of these reservoirs where tight well spacing, stimulation (fracturing) and or horizontal well completion is usually required.

The main objective of this article is to show a process of fluid characterization in unconventional tight sand that guides reservoir stimulation.

Porosity partitioning using nuclear magnetic resonance (NMR) logging data helps address these challenges in three distinct steps. First, the one-dimensional NMR T_2 spectrum quantifies the amount of bound and free fluids pore space and reveals reservoir quality with unique sensitivity. In this step, the NMR fluid substitution method was utilized to ensure consistency between NMR logs in oil-based mud (OBM) and water-based mud (WBM) systems. Second, the free fluids are further subdivided into hydrocarbon and water phases using a two-dimensional (2D) NMR T_1/T_2 processing technique. Third, the hydrocarbon phase is subdivided again into liquid and gas phases where a gas flag is turned on whenever the NMR gas signal significantly exceeds measurement uncertainty. This enables the detection of live hydrocarbons with a high gas-oil ratio (GOR).

This article presents the integration of NMR analysis into petrophysical evaluation of an unconventional tight sand reservoir. The evaluation helped optimize the best interval for stimulation. Fluid samples acquired with the formation tester correlated very well with the NMR log-based fluid prediction.

Integrated NMR analysis, including bound fluid vs. free fluid analysis and 2D NMR-based fluid characterization, including a gas indicator flag, was applied to establish the presence and type of hydrocarbon in tight sands and select the best representative interval for stimulation. The continuous reservoir quality and fluid distribution profiles provided by these logs were beneficial for the geological understanding and complex formation testing operations in this challenging reservoir.

Introduction

Tight reservoir sands described in this article have very low permeability; mostly less than 0.1 md. The low permeability was owing to cementation, compaction, poor sorting, and fine to very fine grained rock. In these formations, tight well spacing, stimulation (fracturing) or horizontal well completion are usually required. To better assist subsequent rig operations and field development design, having an accurate understanding of the fluid properties and reservoir rock quality at the earliest possible time is very important.

Conventional downhole logs generally provide limited petrophysical information in these reservoirs. Wireline formation testing (WFT) pressure measurements and sampling have limited success in tight sands, which are also mostly beyond the capabilities of conventional drillstem tests.

Additional petrophysical details are provided by nuclear magnetic resonance (NMR) logging tools¹⁻⁴. The main outputs for evaluating the reservoir discussed in this article include rock properties such as lithology independent porosity, pore size partitioning with the estimation of bound/free fluid porosities and permeability, as well as reservoir fluid characterization using simultaneous analysis of the NMR T_1 and T_2 relaxation properties.

In this article, a multiple step workflow is presented, which integrates NMR logs with core data, formation testing results, and fluid evaluation. For rock quality evaluation, a cutoff-based NMR bound fluid model is constructed and subsequently calibrated to core permeability. Within this step, the option of correcting for the effect of oil-based mud filtrate (OBMF) invasion is discussed in detail. The NMR log evaluation is completed with reservoir fluid characterization using a simple gas detection flag based on a two-dimensional (2D) NMR T_1 and T_2 analysis.

Limitations of Conventional Log Analysis in Tight Sands

Figure 1 shows conventional log data acquired in a tight sand reservoir. Natural gamma ray is plotted in track 1, and the borehole profile is shown in track 3. The density and neutron results (DENS and NEUT) are displayed in track 4, and the resistivity logs (RDEEP, RMED, RSHAL) are presented in track 5. Tight sands usually have low gamma ray readings indicating the absence of clays and minor variations in formation lithology that do not correlate with reservoir quality. Calculation of pore space from bulk measurements such as density, neutron, and sonic log measurements are prone to mathematical uncertainties in tight reservoirs. For the same reason, the neutron/density cross-over interpretation for fluid type becomes impractical. Additionally, formation resistivity is relatively high due to low porosity and pore geometry variations. This poses a challenge to the quantification of hydrocarbons using resistivity logs.

In these formations, additional log measurements are required to improve sensitivity pore size variations, and determine formation fluids independently from resistivity-based approaches.

Integrated NMR-based Petrophysical Analysis

The process of fluid characterization with the integration of NMR data applied in this article for tight sands includes the following steps:

- Data acquisition
- Data quality check
- NMR fluid substitution for wells drilled with oil-based mud (OBM)
- Permeability calibration
- Fluid typing

- Fluid contact identification

Data Acquisition

Well-A was drilled with water-based mud (WBM) across a tight sand reservoir. Data acquired across the reservoir includes Quad combo data — gamma ray, resistivity, neutron, density and sonic logs (and with spectral gamma ray called Penta Combo wireline logs, mud logging data, core data, formation tester for pressure/samples and special (NMR) logs. Conventional core data was also acquired and plugged for core analysis. There was no valid pressure data acquired. Four sample stations were also attempted with only one being successful. Light oil was acquired from this one successful station. Data acquired in Well-A is plotted in Fig. 2. The Quad combo logs are plotted in tracks 1, 3, and 4, followed by pressure and sampling points. The mud logging data is plotted in tracks 6 and 7. The NMR data is plotted in tracks 8-10. The core gamma ray is also plotted in track 1, and the core permeability is plotted in track 7.

The NMR data was acquired with a multifrequency NMR tool acquiring a data set of multiple echo trains with seven different wait times, Table 1. The purpose of this activation is a simultaneous inversion for T_1 and T_2 distribution for basic rock typing and advanced fluid characterization.

Well-B was drilled with OBM across a tight sand reservoir. The Quad combo and spectral gamma ray logs, mud logging data, core data, and NMR logs were acquired across the reservoir. Unlike Well-A, pressure and sampling were not attempted. Figure 3 is a plot of data acquired in Well-B. The Quad combo logs are plotted in tracks 1, 3, and 4. The mud logging lithology and gases are plotted in tracks 5 and 6. The NMR data is plotted in tracks 7-9. The core gamma ray logs are also plotted in track 1, and the core permeability is plotted in track 7.

This well was also logged with a multifrequency NMR tool by a different vendor. The multiple wait time acquisition parameters for this data set are as shown in Table 2.

Figure 4 shows the NMR interpretation model for porosity and bound fluid analysis, for Well-A, which is the same as that described by Hursan et al. (2015)⁴. The T_2 cutoff for bound fluid is 100 milliseconds.

Data Quality Check

Due to a conductive WBM, special care was taken to minimize environmental noise by selecting a side looking NMR tool. Log quality was checked by standard data repeatability histograms displaying the statistics of the difference between the main and repeat passes for porosity and bound fluid volume, Figs. 5a and 5b. Data quality is acceptable if: (a) the mean of the difference is close to zero (less than 0.5 porosity units (pu)), (b) the standard deviation remains below 1.4 pu, and (c) the histograms look like Gaussian distributions⁴. The NMR logs in this well comfortably satisfied all of these criteria.

NMR Fluid Substitution

Diagenetically altered sandstone — tight sands — pore systems are possibly subject to OBM invasion. While it is relatively easier to evaluate and correct for the effect

Fig. 1 Conventional log data acquired in a tight sand formation. Gamma ray is plotted in track 1; borehole profile is plotted in track 3; density and neutron (DENS and NEUT) are plotted in track 4; and resistivity logs (RDEEP, RMED, RSHAL) are plotted in track 5.

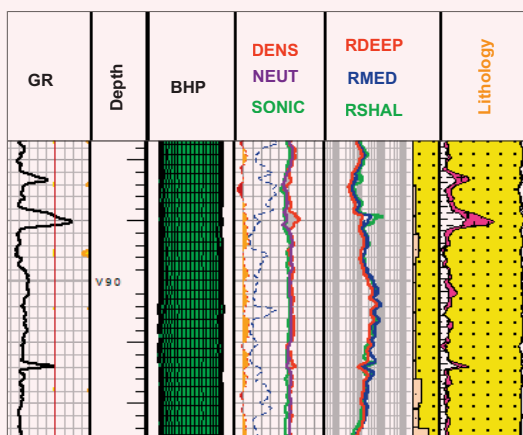
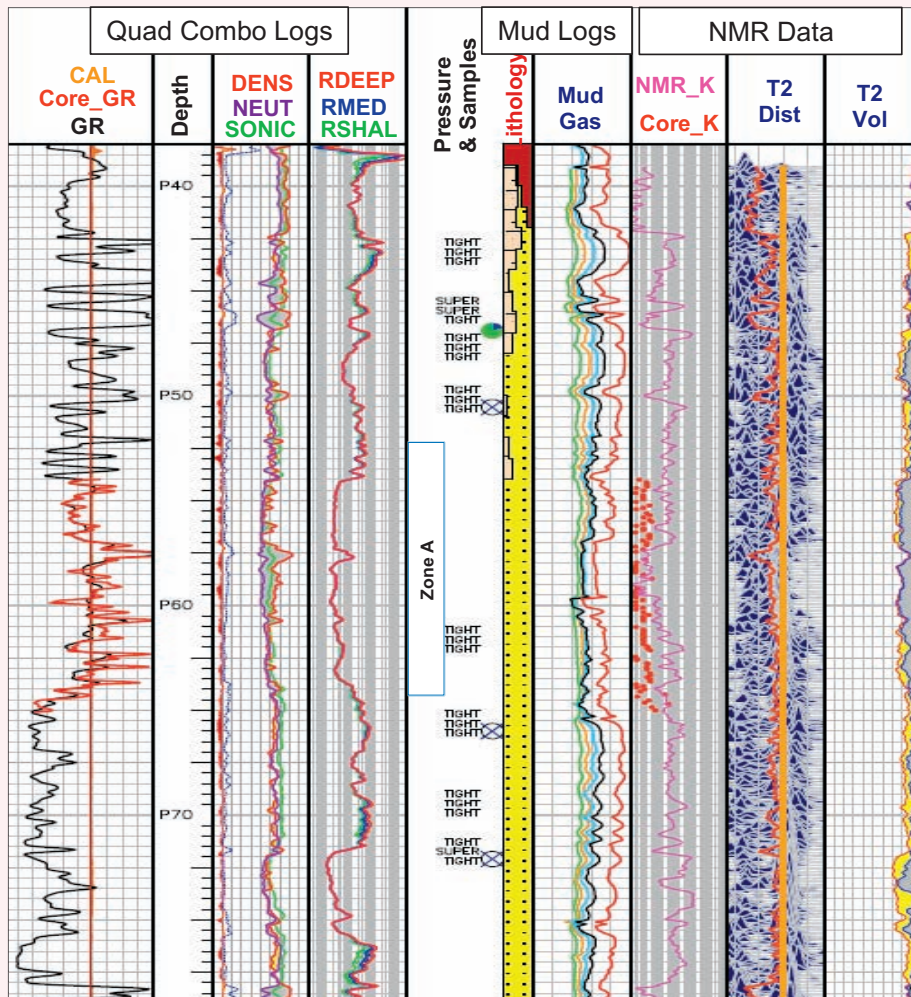


Fig. 2 Data acquired in Well-A. The Quad combo logs are plotted in tracks 1, 3, and 4, followed by pressure and sampling points. The mud logging data are plotted in tracks 6 and 7. The NMR data is plotted in tracks 8-10. The core gamma ray is also plotted in track 1, and the core permeability is plotted in track 7.



of filtrate invasion in basic logs, special care must be taken for advanced logging techniques such as NMR⁵. In Well-B, the NMR spectrum is affected by a significant OBMF invasion, particularly in Zone C, Fig. 3. The OBMF signal is the peak with a slow relaxation time (exceeding 1 second), probably caused by prolonged invasion due to slow mud cake build up in the low permeability rocks. This poses potential problems as most NMR petrophysical models are developed based on mostly water saturated rocks. In this well, for example, for an untrained eye the amount of “free fluids” due to the OBMF signal indicates a high quality reservoir, which is contrary to prior expectations, and more importantly, permeability data measured on core samples.

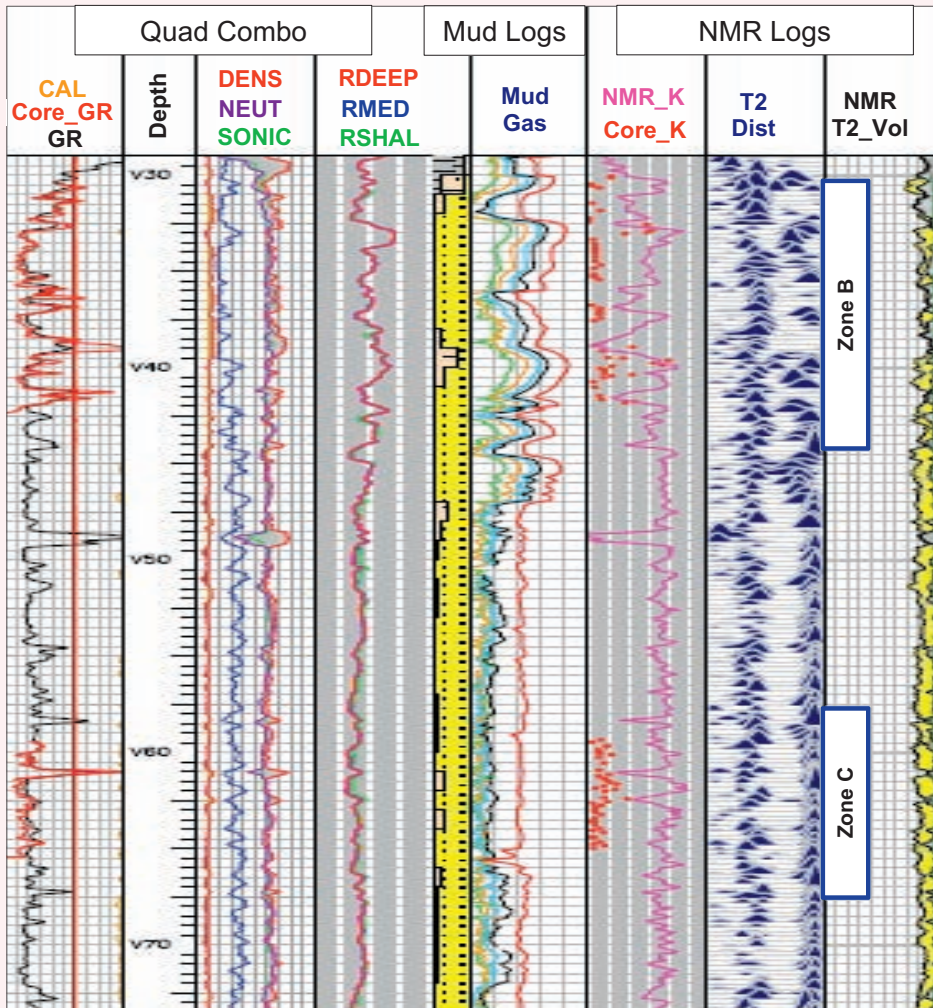
This is not a new phenomenon and the principles of NMR responses in partially saturated rocks has been studied extensively since the advent of NMR logging^{6, 7}. Based on these principles, a log processing technique commonly known as fluid substitution has been developed^{8, 9}. This technique restores the theoretical

Table 1 NMR activation parameters in Well-A.

ID	TW (ms)	TE (ms)	NE
A	12,000	0.9	800
B	3,300	0.9	100
C	10	0.6	50
D	1,000	0.9	100
E	30	0.6	50
F	100	0.6	100
G	300	0.6	100

NMR spectrum of a fully water saturated rock from the NMR logs acquired across a partially saturated reservoir.

Fig. 3 Data acquired in Well-B. The Quad combo logs are plotted in tracks 1, 3, and 4. The mud logging lithology and gases are plotted in tracks 5 and 6. The NMR data is plotted in tracks 7 to 9. The core gamma ray log is also plotted in track 1, and the core permeability is plotted in track 7.



The fluid substitution workflow is presented in Fig. 6. First, the T_2 spectra of oil and water (P_{o, SX_0} and P_{w, SX_0} , respectively) are isolated. Second, the flushed zone total water saturation is calculated as the ratio of the water signal and the total NMR signal. Third, the oil spectrum is removed from the T_2 spectrum. Fourth, the reduction of the water T_2 value due to the NMR surface-to-volume ratio effect is compensated. Fifth, the water spectrum is amplified to match the original NMR total porosity, i.e., substituting the oil signal.

Figure 7 demonstrates the effect of this procedure for Well-B. From left to right, the observed NMR T_2 spectrum and the volumetric analysis are displayed in the first two tracks, and the NMR logs after fluid substitution in the last two tracks. At the left side of the last track, the free fluid estimation is displayed for clarity.

Permeability Calibration

Four methods to calculate permeability have been tried as follows, Fig. 8:

Table 2 NMR activation parameters in Well-B.

ID	TW (ms)	TE (ms)	NE
A	13,000	0.9	690
B	1,000	0.9	690
C	300	0.6	25
D	100	0.9	25
E	50	0.6	25
G	20	0.4	25

- Calibration of core permeability with conventional porosity/permeability model.
- Uncalibrated NMR log-based permeability, utilizing

Fig. 4 Basic NMR interpretation models for porosity and bound fluid analysis for Well-A⁴.

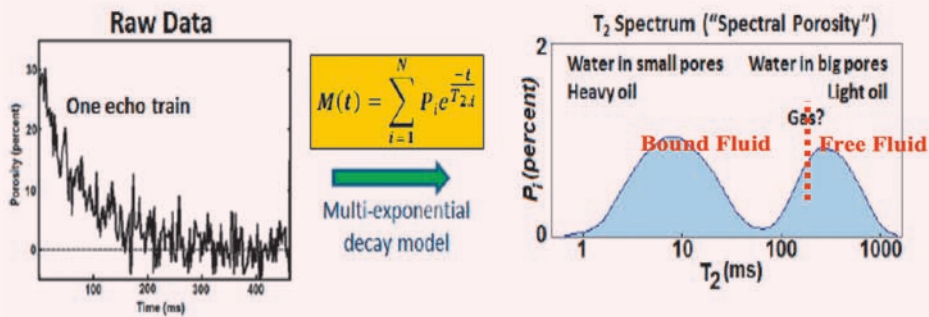


Fig. 5 The histogram plots of the difference in bound fluid volume (left), and porosity (right) between the main and repeat passes with their mean and standard deviation within the acceptable range of ± 0.1 pu for mean and ± 0.4 pu for standard deviation.

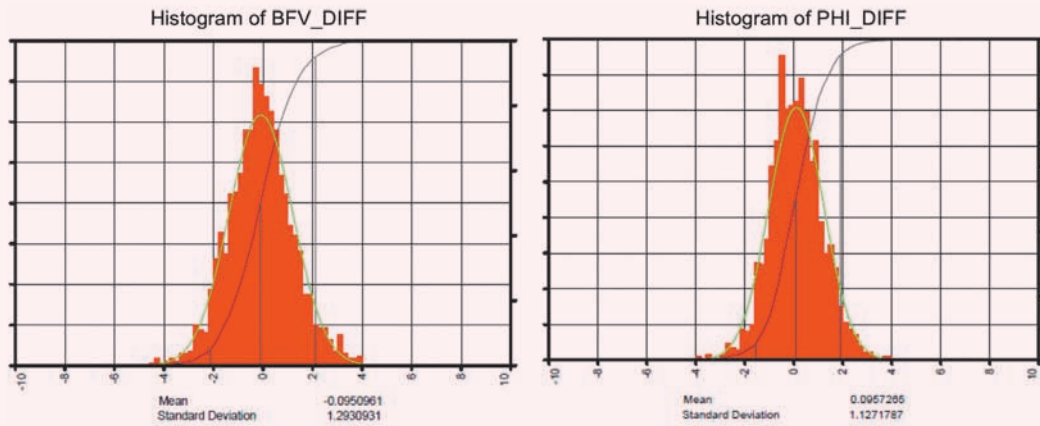
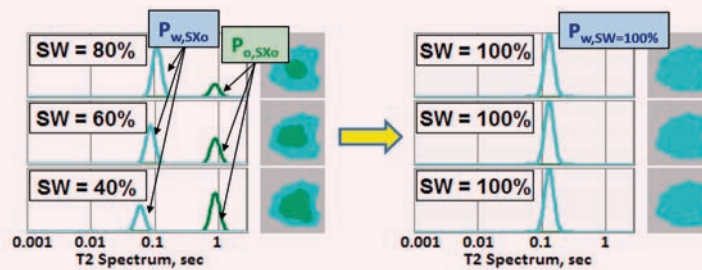


Fig. 6 Fluid substitution workflow.



1. Find Oil and Water T2 Spectra $P_{o,SXo}$ and $P_{w,SXo}$

2. Calculate SXo

$$SXo = \frac{\int_{T_2} P_{w,SXo}(T_2) dT_2}{\int_{T_2} P_{w,SXo}(T_2) dT_2 + \int_{T_2} P_{o,SXo}(T_2) dT_2}$$

3. Remove Oil spectrum P_o

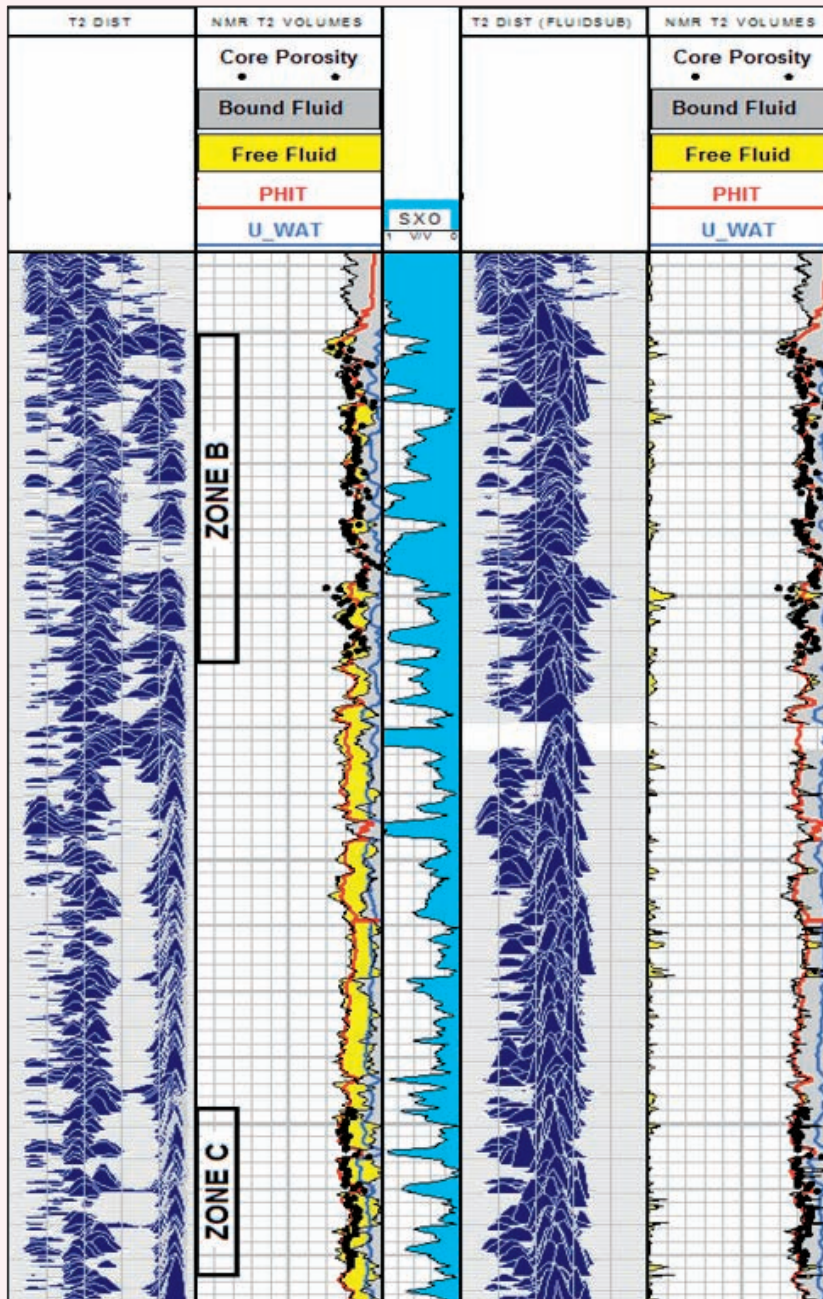
4. Shift T2 of water spectrum

$$T_{2,w,SW=1} = \frac{T_{2,w,SXo}}{SXo}$$

5. Amplify T2 water spectrum

$$P_{w,SW=100\%} = \frac{P_{w,SXo}}{S_w}$$

Fig. 7 Tracks 1 and 2: Observed NMR T_2 spectrum and fluid partitioning logs in Well-B, Track 3: SXO log, Tracks 4 and 5: NMR logs after fluid substitution. At the left side of the last track, the free fluid estimation is displayed for clarity.



the Coates' equation NMR logs, originally developed for conventional reservoirs.

- Coates permeability using as-measured NMR log that was calibrated in Zones A and B, which had WBM or no significant OBMF invasion.
- Coates permeability using as-measured NMR data in Well-A, and the fluid substituted NMR log in Well-B, calibrated in all zones (A, B, and C).

The conventional porosity log-based permeability

— Permeability A — correctly captures low permeability zones but it is unable to detect the high permeability streaks in Zone B. The uncalibrated NMR log-based Coates permeability — Permeability B — shows more sensitivity to permeability variations than Permeability A, however, in its unchanged form, it overestimates permeability in this reservoir. Following a standard procedure, the Coates coefficients have been calibrated to the measured NMR logs and the core data in Zones A and B — Permeability C.

Fig. 8 Core vs. log-based permeability estimates in Wells A and B.

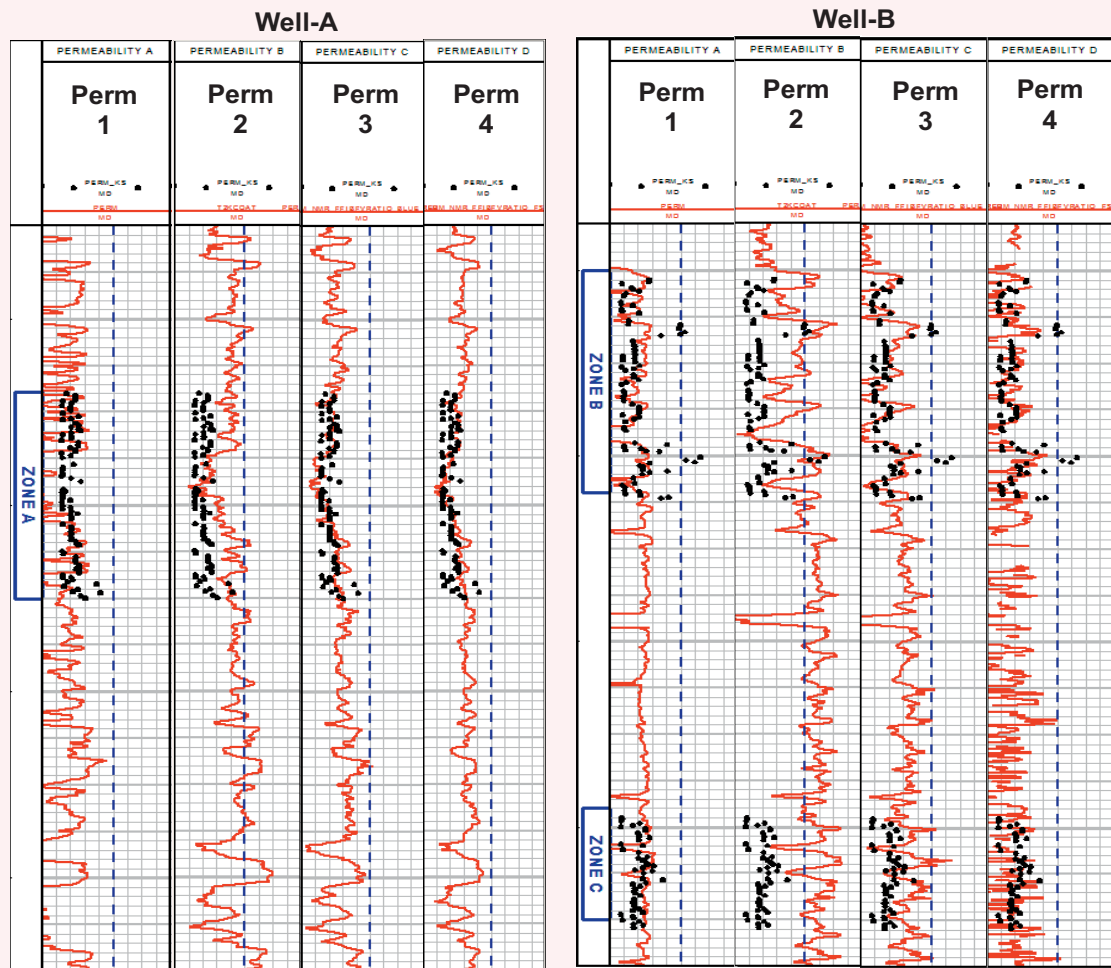
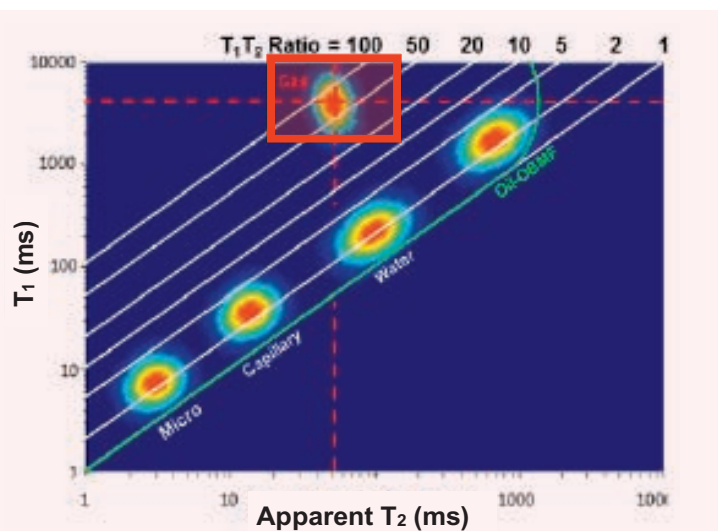


Fig. 9 A 2D cross-plot showing the simultaneous inversion of the T_2 vs. T_1 map for advanced fluid typing interpretation in Well-A.



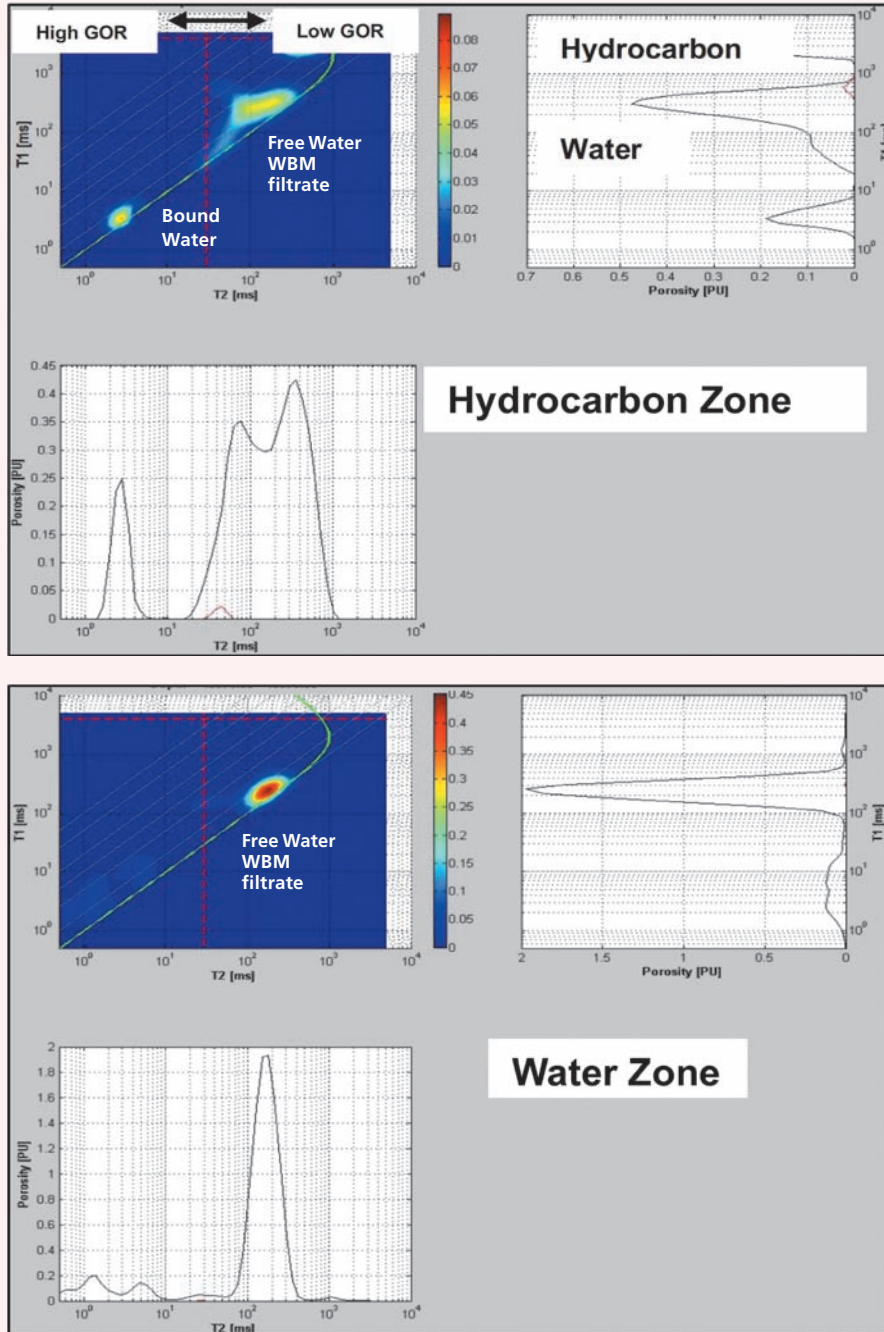
In this procedure, Zone C was not utilized due to the significant OBMF invasion effect on the NMR logs. Not surprisingly, Permeability C provides a good prediction for the zones with no OBMF invasion, including the sweet spots. It still overestimates the permeability in Zone C where the NMR log is affected by OBMF invasion. The final approach — Permeability D — begins with the fluid substitution in Well-B to correct for the OBMF invasion effect. Then, the Coates parameters are adjusted using the fluid substituted NMR log and the core data from all zones. This approach appears to increase the robustness in the presence of OBMF invasion.

Fluid Typing

For fluid typing interpretation in Well-A, a simultaneous inversion of T_1 and T_2 relaxation times using a 2D cross-plot has been utilized, Fig. 9. In these plots, water in different pore sizes, oil, and gas are uniquely positioned. In Well-A, a gas flag is constructed by quantifying the NMR signals falling into the “gas box,” drawn around the theoretical position of methane.

Figure 10 presents two 2D NMR “ T_1 - T_2 ” maps

Fig. 10 Two 2D NMR “ T_1 - T_2 ” maps from a hydrocarbon zone and a water zone in Well-A, respectively. The hydrocarbon signature, with T_1 above 1 sec, is present in the 2D plot for hydrocarbon and absent in the 2D plot for water.



from a hydrocarbon zone and a water zone in Well-A, respectively. The hydrocarbon signature, with T_1 above 1 sec is present in the 2D plot for hydrocarbon and absent in the 2D plot for water.

In Well-B, the 2D fluid typing model is somewhat different: instead of a T_1 vs. T_2 map, a T_2 vs. T_1/T_2 ratio cross-plot, also known as the “R- T_2 map,” is constructed, Fig. 11. Similarly, this model also enables the construction

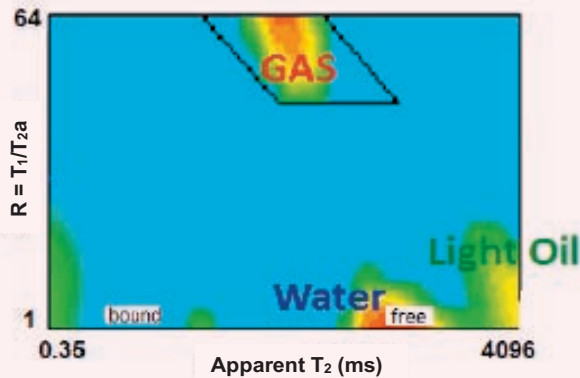
of the “gas box” and the gas flag interpretation.

Figure 12 presents two 2D NMR “R- T_2 ” maps from a hydrocarbon zone and a water zone in Well-B. The gas flag signature is evident on the plot in the hydrocarbon zone and absent on the plot from the water zone.

Fluid Contact Definition

In Well-A, the gas flag log generated (previously mentioned) was integrated into the analysis to define

Fig. 11 The 2D T_2 vs. $R = T_1/T_2$ ("R- T_2 ") map for fluid typing interpretation in Well-B.



the depth that hydrocarbon got to. Figure 13 shows the definition of the hydrocarbon down to a depth of ~P78 with the integration of the gas flag log, 2D NMR T_1 - T_2 plot, and is supported by the reduction in the mud gas readings below the depth of ~P78. A light oil sample was collected at a depth of P47 at the same location where the 2D NMR " T_1/T_1 " shows the presence of low gas-oil ratio (GOR) fluid. This confirms the fluid typing from NMR.

In Well-B, the gas flag log generated with the gas signal previously described was integrated with the 2D NMR " R - T_2 " to define the hydrocarbon-water contact. Figure 14 shows the definition of the hydrocarbon-water contact

with the integration of the gas flag log. The 2D NMR was supported by a drop in the mud gas readings below a depth of ~V47. The resistivity logs (track 3) are generally high through the section and there is not much difference between the hydrocarbon and water intervals. Since the water is saline in this reservoir, the high resistivity in the water interval could be attributed to the formation thickness. The 2D NMR map acquired at depths of V35 and V40 show the gas signature while the 2D map acquired at depth V48, which is below the proposed fluid contact, does not have the gas signal. Also, from the gas flag log (track 11), the gas flag was totally absent below the hydrocarbon-water contact.

Validation of NMR-based Petrophysical Analysis

In Well-A, the open hole logs were followed by a WFT program. The plan included a number of pressure tests and four samples across the reservoir. Overall, 95% of the formation pressure tests attempted were tight, and the other 5% were supercharged. Three out of the four sampling stations attempted were aborted owing to lack of flow. A light oil sample was collected at the 4th sampling station after continuous pumping for ~11 hours with a volume of ~200 liters pumped out. All of the non-tight pressure and sampling measurements occurred where the highest NMR-based permeability was observed. Also in the well, resistivity logs were high in most parts of the interval, posing uncertainties as to the determination of the possible hydrocarbon-water contact. After acquiring NMR T_1 and T_2 data, two station logs were acquired at the depth of P47 and P72. The presence of low GOR fluid

Fig. 12 Two 2D NMR " R - T_2 " maps from a hydrocarbon zone (left) and a water zone (right) in Well-B. The gas flag is on the plot in the hydrocarbon zone and not on the plot from the water zone.

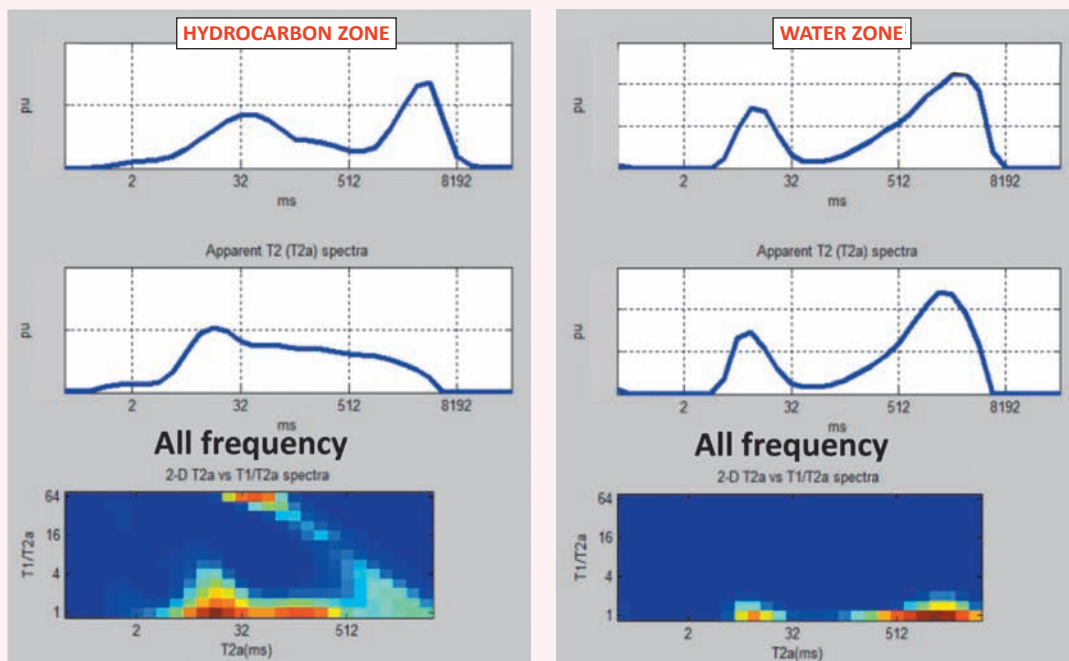
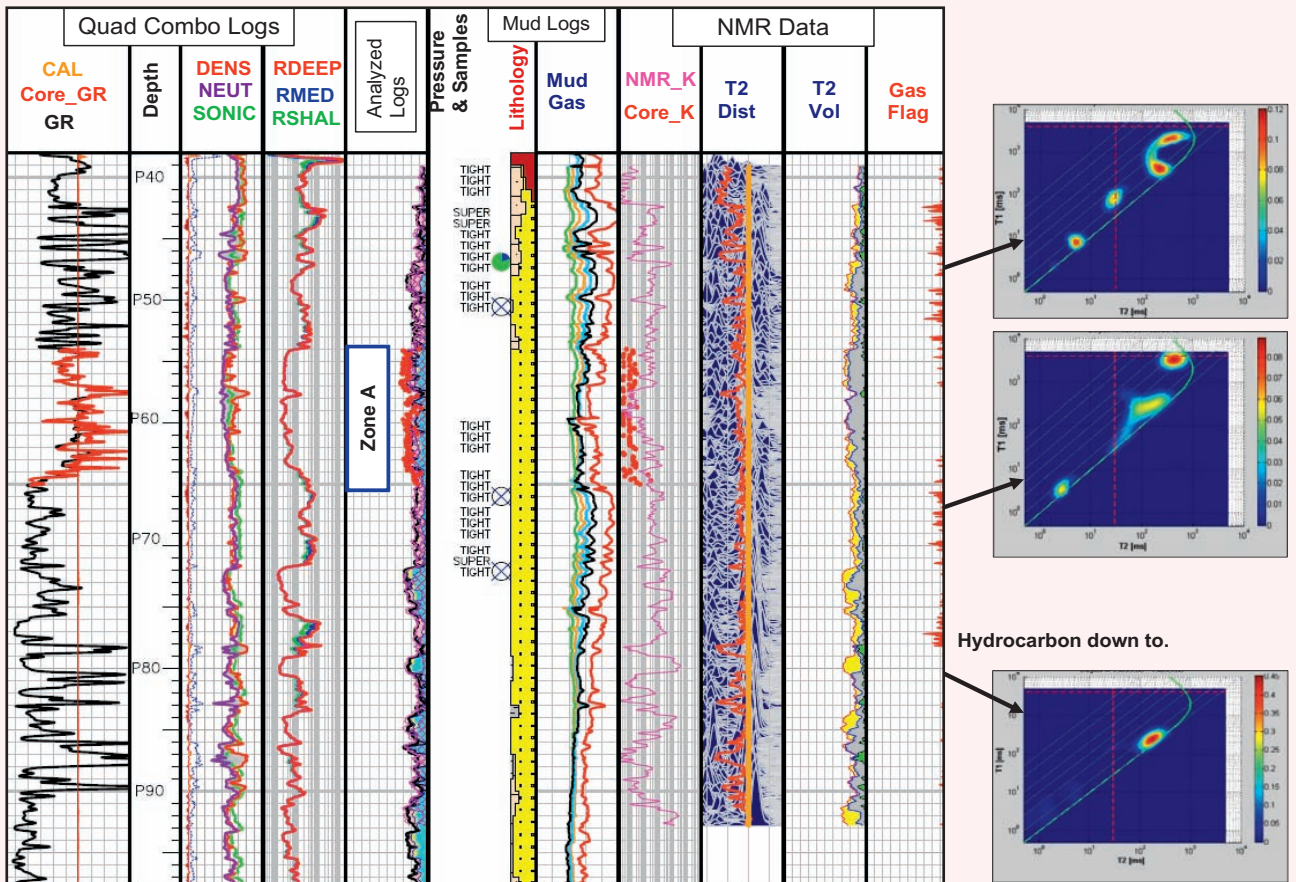


Fig. 13 Integrating the gas flag and 2D NMR supported by mud gas to confirm hydrocarbon down to a depth of ~P78. The gas flag is plotted in track 12, and mud gas is plotted in track 8. The 2D NMR plots are to the right of the log plot.



(oil) was established at both stations (2D plots above the fluid contact in Fig. 11). One of the station logs (depth P47) was collected at the same location where the oil sample was collected. Since the station log data is in conformity with the sample acquired at that location, the NMR data, including the other station logs, were applied to confirm the presence of hydrocarbon and the best interval for stimulation.

In Well-B, resistivity logs were relatively high across the section. Since the water in the location is saline, the high formation resistivity is interpreted as hydrocarbon-bearing. The resistivity logs do not present a clear-cut transition from hydrocarbon to the water-bearing reservoirs. Contrary to this, there is a sharp drop in the mud gas at a depth of V47. Since the formation pressure and sampling data were not acquired owing to formation properties, the 2D NMR-based and gas interpretation was utilized to propose the hydrocarbon-bearing interval for stimulation. The NMR gas flag coincides with the mud gas results, suggesting that the hydrocarbon-water transition to be around a depth of V47.

Limitations of NMR Logging

The main limitations of NMR log evaluation in this low

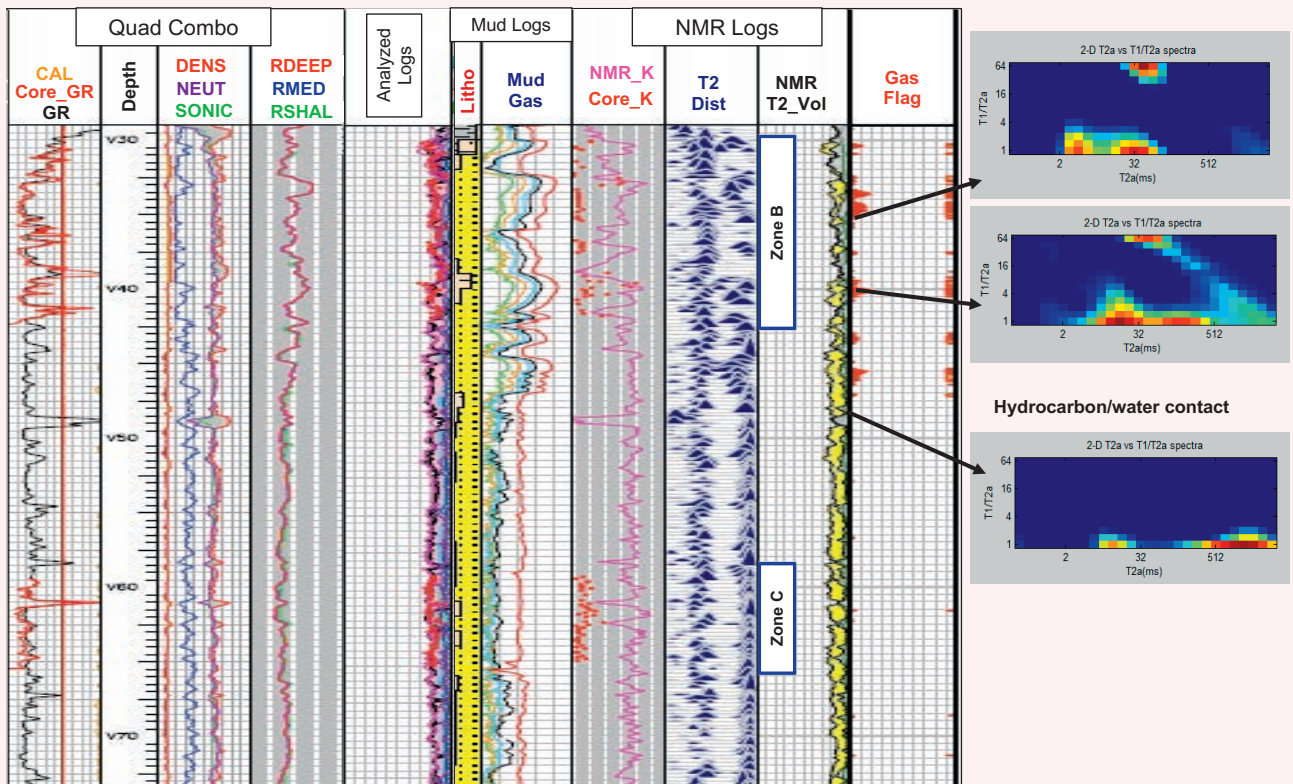
permeability reservoir stem from extensive mud filtrate invasion. Mud filtrates reduce the amount of native reservoir fluids in the shallow sensitive volume of the NMR tool. As a result, fluid characterization remains qualitative and it is limited to a “gas flag” evaluation. Excessive OBM invasion may increase the estimated free fluid volume. This effect can be mitigated using the fluid substitution technique. If the OBMF invasion is extreme, the procedure becomes unstable due to weakness of the remaining water signal. The authors feel that such zones exist in the vicinity of Zone C in Well-B.

Finally, although the NMR log-based permeability has better sensitivity than that of the conventional logs, the standard Coates formula is unable to fully predict the magnitude of permeability variations in Zone B. Possible ways to improve this include customized nonlinear models, or integrated permeability calculations using neural network-type approaches.

Conclusions and Recommendations

This article summarizes the lessons learned from an integrated NMR petrophysical analysis across a tight sand reservoir. The logs were acquired in two different mud systems. Although this posed difficulties in the

Fig. 14 Integrating the gas flag and 2D NMR supported by mud gas to confirm hydrocarbon water contact. The 2D NMR map acquired at a depth of V35 and V40 show the gas signature while the 2D map acquired at a depth of V48, which is below the contact, does not have the gas signal. Also, from the gas flag log (track 11), the gas flag was totally absent below the hydrocarbon water contact.



initial interpretation, significant value was added by the development of a robust workflow for NMR analysis in both OBM and WBM. In this workflow, the NMR data in OBM is corrected using the fluid substitution method. This corrected NMR data is comparable with that acquired with WBM. The workflow also includes a 2D NMR-based “gas flag” that was found to be useful in detecting the hydrocarbon contact where resistivity-based analysis shows limited sensitivity. In one of the wells, WFT data confirmed the NMR-based fluid and rock quality analysis.

The following workflow is proposed for NMR acquisitions and petrophysical analysis in these tight sands:

- Acquire high-quality multiple wait time NMR data that allows simultaneous T_1 and T_2 analyses based on a 2D NMR processing algorithm.
- If significant amounts of hydrocarbons exist in the flushed zone, e.g., the well is drilled with OBM, the NMR data needs to be corrected using the fluid substitution technique.
- The NMR-based permeability and fluid characterization (fluid typing and contact definition) data should be used for optimizing WFT and/or well testing operations.

- Additional core permeability measurements are recommended for additional improvement of the permeability model and enable advanced permeability modeling.

Acknowledgments

The authors would like to thank the management of Saudi Aramco for their support and permission to publish this article. The authors would also like to thank Yasir Farooq of Halliburton, Sadiq S. Nasser, Ahmed Abouzaid, and Hasan Kesserwan of Baker Hughes for their contributions to this article.

This article was presented at the SPE Middle East Oil and Gas Show and Conference, Manama, Kingdom of Bahrain, March 18-21, 2019.

References

1. Allen, D., Crary, S., Freeman, B., Andreani, M., et al.: “How to Use Borehole Nuclear Magnetic Resonance,” *Oilfield Review*, Vol. 9, No. 2, June 1997, pp. 34-37.
2. Coates, G.R., Xiao, L. and Prammer, M.G.: *NMR Logging Principles and Applications*, Halliburton Energy Services Publication H02308, 1999, 251 p.
3. Meridji, Y., Hursan, G.G., Eid, M. and Balliet, R.: “Fluid Identification in Complex Clastic Reservoirs Using 2D NMR Maps: A Case Study of Saudi Arabia,” SPE paper 168073, presented at the SPE Saudi Arabia Section Technical

- Symposium and Exhibition, al-Khobar, Saudi Arabia, May 19-22, 2013.
4. Hursan, G.G., Deering, J.S. and Kelly, F.N.: "NMR Logs Help Formation Testing and Evaluation," SPE paper 177974, presented at the SPE Saudi Arabia Section Annual Technical Symposium and Exhibition, al-Khobar, Saudi Arabia, April 21-23, 2015.
 5. Hursan, G.G., Ma, S.M., Valori, A. and Sauerer, B.: "Study of OBM Invasion on NMR Logging — Mechanisms and Applications," SPE paper 192218, presented at the SPE Kingdom of Saudi Arabia Annual Technical Symposium and Exhibition, Dammam, Saudi Arabia, April 23-26, 2018.
 6. Straley, C., Morriss, C.E., Kenyon, W.E. and Howard, J.J.: "NMR in Partially Saturated Rocks: Laboratory Insights on Free Fluid Index and Comparison with Borehole Logs," *The Log Analyst*, Vol. 36, No. 1, January-February 1995, pp. 40-56.
 7. Hofman, J., Slijkermail, W., Looyestijn, W. and Volokitin, Y.: "Constructing Capillary Pressure Curves from NMR Log Data in the Presence of Hydrocarbons," paper presented at the SPWLA 40th Annual Logging Symposium, Oslo, Norway, May 30-June 3, 1999.
 8. Christensen, S.A., Thern, H.F. and Vejbaek, O.: "NMR Fluid Substitution Method for Reservoir Characterization and Drilling Optimization in Low-Porosity Chalk," paper presented at the SPWLA 56th Annual Logging Symposium, Long Beach, California, July 18-22, 2015.
 9. Minh, C.C., Jain, V., Griffiths, R. and Maggs, D.: "NMR T₂ Fluids Substitution," paper presented at the SPWLA 57th Annual Logging Symposium, Reykjavik, Iceland, June 25-29, 2016.

About the Authors

Endurance Oziegbe Ighodalo

M.S. in Petroleum Geoscience,
Oxford Brookes University

Endurance Oziegbe Ighodalo is a Petrophysicist working with the Northern Area Petrophysics Team in the Reservoir Description Division of the Reservoir Description & Simulation Department. He joined Saudi Aramco in December 2014.

Prior to this, Endurance worked as a Senior Petrophysicist with Total E&P in Nigeria. While in Total, he worked in both Operations and study teams in onshore, offshore, and deep offshore environments.

Endurance has previously published conference papers on the subject of electrofacies and permeability modeling in clastics reservoirs, and in advanced mudlogging.

In 2000, he received his B. Tech. degree in Geology from the Federal University of Technology, Owerri, Nigeria, and in 2003, Endurance received his M.S. degree in Petroleum Geoscience from Oxford Brookes University, Oxford, U.K.

Dr. Gabor G. Hursan

Ph.D. in Geophysics, University of Utah

Dr. Gabor G. Hursan is a Petrophysicist in Saudi Aramco's Reservoir Description and Simulation Department. He is Saudi Aramco's focal point for nuclear magnetic resonance (NMR) well logging and formation evaluation. Previously, Gabor worked as a Scientist and Project Leader on NMR technology development at Baker Hughes for 10 years.

He has published several papers and patents,

teaches classes in NMR logging and is a reviewer for technical publications. Gabor is a member of the Society of Petroleum Engineers (SPE) and the Society of Petrophysicists and Well Log Analysts (SPWLA).

He received his M.S. degree in Geophysical Engineering from the University of Miskolc, Miskolc, Hungary, and his Ph.D. degree in Geophysics from the University of Utah, Salt Lake City, UT.

John McCrossan

B.S. in Geological Engineering,
Queens University

John McCrossan was a Senior Geological Consultant (Petrophysicist), working in Saudi Aramco's South Ghawar Exploration and Development Department prior to his recent retirement.

He joined Saudi Aramco in 2009, after a stint with

Schlumberger (in the U.S. and Canada), Suncor Energy, ConocoPhillips, and Husky Energy.

In 1984, John received his B.S. degree with Honors in Geological Engineering from Queens University, Kingston, Ontario, Canada.

Ali R. Al-Balawi

B.S. in Petroleum Engineering,
King Saud University

Ali R. Al-Balawi joined Saudi Aramco in August 1989 as a Petroleum Engineer. In his early career, he spent many years in Well Testing, where he was responsible for testing many exploratory wells throughout Saudi Arabia. Ali has also done extensive and various petrophysical work in different exploration and development areas. During his extensive career, Ali has worked in several different departments, including

Drilling Engineering and Reservoir Management, where he was the Supervisor of the North 'Uthmaniyah Reservoir Management Unit.

Currently, Ali is the Supervisor of the Exploration Petrophysics Unit in the Reservoir Description Division.

He received his B.S. degree in Petroleum Engineering from King Saud University, Riyadh, Saudi Arabia.

Experimental Investigation into the Interactions between Three Types of Aqueous-based Fluids and Tight Organic-Rich Carbonate Source Rocks

Dr. Feng Liang, Jilin Zhang, Dr. Hui-Hai Liu, and Kirk M. Bartko

Abstract /

Hydraulic fracturing has been widely used for unconventional reservoirs, including organic-rich carbonate formations for oil and gas production. During hydraulic fracturing, massive amounts of fracturing fluids are pumped to crack open the formation, and only a small percentage of the fluids are recovered during the flow back process. The negative effects of the remaining fluid on the formation, such as clay swelling and reduction of rock mechanical properties, have been reported in the literature; however, effects of the fluids on source rock properties — especially on microstructures, porosity and permeability — are scarcely documented. In this study, microstructure and mineralogy changes induced in tight carbonate rocks by imbibed fluids and corresponding changes in permeability and porosity are reported.

Two sets of tight organic-rich carbonate source rock samples were examined. One sample set was sourced from a Middle East field and the other was an outcrop from the Eagle Ford Shale, which is considered to be similar to the one from the Middle East field in terms of mineralogy and organic content. Three types of aqueous-based fluids, namely 2% potassium chloride (KCl), 0.5 gpt slick water, and synthetic seawater, were used to treat the thin section of the source rock and core samples. Analytical techniques such as a scanning electron microscope (SEM) and energy dispersive spectroscopy (EDS) were used to investigate the source rock morphology and mineralogy changes prior to and after the fluid treatment at the micron-scale level. Permeability as a function of effective stress was quantified on core samples to investigate changes in flow properties due to fluid treatments.

The SEM and EDS results prior to and after fluid treatments on the rock samples showed the microstructural changes in all three fluids. For 2% KCl and slick water fluid, the reopening of some mineral filled natural fractures was observed. The enlargement of the aperture for preexisting microfractures was slightly more noticeable for samples treated with 2% KCl in comparison to slick water at the micron-scale level. Mineral precipitation of sodium chloride (NaCl) and new microfractures generation were observed for samples treated with synthetic seawater.

The formation of new microfractures and the dissolution of minerals could result in increases in both porosity and permeability, while the mineral deposition would result in a permeability decrease. The overall increase in absolute gas permeability was quantified by the experimental measurements under different effective stress for the core plug samples. This effect on absolute gas permeability increase may have an important implication for hydrocarbon recovery from unconventional reservoirs.

This study provides experimental evidence at different scales that an aqueous-based fracturing fluid may potentially have a positive effect on gas production from organic-rich carbonate source rock by increasing absolute gas permeability through mineral dissolution, and the generation of new or re-opening of the existing microfractures. This observation will be beneficial to the future usage of freshwater and seawater-based fluids in stimulating gas production for organic-rich carbonate formations.

Introduction

Studies on carbonate source rocks in the oil and gas industry are particularly important due to the fact that more than 60% of the world's oil and 40% of its gas reserves are trapped in carbonate fields¹. In the Middle East region, carbonate fields are dominant with around 70% of oil and 90% of gas reserves¹. Acid fracturing and matrix acidizing have been proven effective in stimulating conventional carbonate reservoirs due to its reactivity with acids². Subsequently, hydraulic fracturing is still the most effective stimulation technique used for stimulating unconventional organic-rich carbonate formations for oil and gas production, although recently, laboratory experiments have been conducted to explore the possibilities of using acid fracturing to stimulate carbonate-rich shale formations^{3,4}.

Compared to sandstone formations with high clay content, the effect of clay swelling or fines migration during production after the hydraulic fracturing process may not be so prominent in carbonate reservoirs, due to the relatively low amount of clay minerals. Moreover, the predominant mineral in carbonate reservoirs — calcite — is relatively reactive in terms of their solubility when in contact with certain aqueous fluids, especially with low pH fluids. For the conventional carbonate rocks, there are extensive studies on the interactions between injected water and pure calcium carbonate rocks that result in the alteration in the surface wettability, surface chemistry, and surface charge⁵⁻⁸, and on the interactions, which result in the alteration of flow characteristics, i.e., enlarging the permeability due to the dissolution of carbonate minerals⁹.

For tight organic-rich carbonate rocks, studies on mechanical property changes due to the imbibed fluids have been conducted. Akrad et al. (2011)¹⁰ documented the reduction in Young's moduli for organic-rich shales from the Middle Bakken and Eagle Ford formations after their exposure to friction reducer fluids. Lai et al. (2016)¹¹ investigated the mechanical property changes for six aqueous-based fracturing fluids on carbonate-rich Eagle Ford shale. Significant reductions in the ultimate compressive strength (UCS), Young's modulus and Brazilian tensile strength were observed for shale samples treated by fracturing fluids.

It is crucial to further improve our understanding on the effects of the imbibed fluid on the mechanical, morphological, and flow properties of tight organic-rich carbonate rocks, given the complexity of the carbonate source rocks, their high heterogeneity, and the effect on the production due to their interaction with fracturing fluids. Despite the extensive previous studies of the interaction between carbonate rocks and fracturing fluid, there are very few microscopic studies on the textural, including microfractures and mineralogic changes of the fluid and rock interaction.

Microfractures, the term in geologic parlance, refer to fractures which require a microscope to detect, having lengths of millimeters or less, and apertures less than 0.1 mm^{12, 13}. Gale et al. (2014)¹³ noted that sealed microfractures occur in shales but are uncommon, which might be due to the fact that the size of the microfractures could possibly be below the resolution of the imaging tools in the past studies, or they were not captured in the small volumes of rock analyzed. The authors also conclude that the role of microfractures in shale production is poorly understood and would merit further study.

Recently, Wu and Sharma (2017)⁴ conducted a thorough study on the changes of microstructures and pore structures for high carbonate Bakken shale, which was treated with diluted acids. Channels in carbonate-rich regions, cavities or grooves in carbonate islands or carbonate rings, and roughness in areas of scattered carbonate were observed after acid treatment due to the reactive nature of carbonates with diluted acids. The hardness of the shale fracture surface was reduced by 30% to 70% by acid treatment. Although, the contribution

of pore structure changes by acid treatment to the flow properties yet needs to be quantified.

Liang et al. (2017)¹⁴ presented the results of a microscopic study on the morphological and mineralogical changes on a sample surface when exposed to 2% potassium chloride (KCl) fluid — with neutral pH — for organic-rich tight carbonate source rocks and the associated changes in terms of porosity and permeability.

In this work, we present more studies of similar carbonate rock samples when exposed to various types of aqueous-based fluids, such as 2% KCl, 0.5 gpt slick water, and synthetic seawater (with neutral pH), focusing on the morphological and mineralogic changes as well as changes in permeability. The study is part of the research to find an approach to quantitatively relate all of the changes in morphology, mineralogy, and permeability using multiscale experiments to the optimization of hydrocarbon production in carbonate reservoirs.

Experimental Methods

Materials

Source Rock Samples. Two sets of tight organic-rich carbonate source rock samples were used in this study. One sample set was a highly laminated carbonate sample from a basin in the Middle East field, which was used for morphological and mineralogic studies. Three thin section samples with a dimension of 7.5 × 7.5 × 2.5 mm (length × width × thickness) were sliced using a trim saw and glued to a piece of fiberglass. The rock surface was then fine-trimmed using a Leica EM TXP trimmer and milled using a Leica EM TIC 3X broad ion beam mill. The total organic carbon (TOC) of the thin section sample was around 12.1 wt%. The mineral content of the thin section sample was determined by X-ray diffraction (XRD) technique and the main minerals are shown in Table 1.

The second sample set used for porosity and permeability study was an outcrop from the Eagle Ford Shale considered to be the analogous to the one from the Middle East field in terms of mineralogy. The TOC of this sample was around 5 wt%. Table 2 lists the mineral content determined by XRD technique.

Treatment Fluids. Three aqueous-based fluids (2 wt%

Table 1 Mineralogy of organic-rich tight rock sample from the Middle East field measured by XRD.

Minerals	Weight %
Calcite	92
Dolomite	2
Quartz	3
Pyrite	< 1
Kaolinite	< 1
Illite	< 1

Table 2 Mineralogy of the outcrop Eagle Ford sample measured by XRD.

Minerals	Weight %
Calcite	66
Dolomite	1
Quartz	26
Gypsum	2
Pyrite	1
Kaolinite	3
Illite	1

KCl, 0.5 gpt slick water, and synthetic seawater) were used in this study for treatment of the rock samples. Fluid 1 was 2 wt% KCl (pH = 7.1). Fluid 2 was 0.5 gpt slick water solution. The slick water polymer used in this study was an acrylamide-based terpolymer and was formulated in a water-in-oil emulsion form with 30% active ingredient. The 0.5 gpt slick water fluid was prepared by hydrating 0.5 mL of acrylamide-based terpolymer (30% active) in 1 liter of deionized water then followed by the addition of 20 grams of KCl. Fluid 3 was synthetic seawater. The composition of the synthetic seawater was based on the water analysis of the representative seawater sample from one Middle East region, Table 3. The synthetic seawater

Table 3 Water analysis of the representative seawater sample from the Middle East.

Ions	Concentration (mg/L)
Barium	< 1
Calcium	618
Iron	< 1
Magnesium	2,108
Potassium	595
Sodium	18,451
Strontium	11
Chloride	30,694
Sulfate	4,142
Carbonate	< 1
Bicarbonate	150
TDS	56,800
Total Hardness	10,200
pH	8.1

was prepared with salts such as sodium chloride (NaCl), calcium chloride, magnesium chloride, sodium sulfate, and sodium bicarbonate.

Surface Characterization for Thin Section Rock Sample. The texture, microstructure, and elemental mapping of the thin section rock samples were analyzed based on scanning electron microscope (SEM) images (from a Zeiss Sigma HPVP SEM) coupled with energy dispersive spectroscopy (EDS) maps (from a Bruker XFlash 6130 EDS detector) prior to the fluid treatments. To capture the sample's morphological change before and after fluid treatment, SEM images and EDS mapping were taken at exactly the same locations after fluid imbibition and the drying process for a comparison. EDS was used to investigate the changes for distribution of various elements before and after fluid treatment.

Fluid Treatment for Thin Section Rock Sample.

Since the amount of mineral dissolution is related to the mass ratio of the treatment fluid and the rock sample, more mineral dissolution is expected with a larger fluid/rock ratio. For consistency, the ratio of fluid mass and rock mass in this study was chosen to be at 10:1. Each thin section rock sample was submerged in a treatment fluid for about 48 hours at ambient temperature then vacuum dried at 80 °C for 24 hours. Each core plug sample was submerged in the treatment fluid for about 72 hours at ambient temperature then vacuum dried at 80 °C for 24 hours.

Identification and Quantification of Dissolved Ions.

After the rock sample imbibition test, all three treatment fluids were analyzed using inductively coupled plasma (ICP) equipped with an optical emission spectrometer (OES) technique. The three original prepared treatment fluids were also tested as controls. Dissolved ions such as magnesium (Mg^{2+}), calcium (Ca^{2+}), and strontium (Sr^{2+}) were each quantified with their own standard solution with a five-point calibration curve, measured in mg/L (or ppm).

Fluid Treatment and Flow Characteristics Assessment for Core Plug Rock Sample.

To assess the impact of morphological change due to mineral dissolution and precipitation on flow parameters of rock samples, fluid treatment experiments for the core plugs were conducted. Due to the lack of the whole core sample of the same type of source rock as on the SEM images, three sister core plugs from the Eagle Ford outcrop, which were considered to be analogous to the one from the Middle East field, were used to conduct the absolute permeability measurement study.

The size of the core plugs used in this experiment was 1" in diameter and 1" in length. The absolute permeability for these core plugs was measured before and after fluid treatment. The methodology of the permeability measurement was based on the pulse decay method proposed by Jones (1997)¹⁵. The permeability was measured using an AP-608 automated porosimeter-permeameter from Coretest Systems.

Results

Surface Characterization of the Thin Section Polished Surface before Fluid Treatment. A large number of SEM images and EDS maps were acquired on the thin section polished surface (before fluid treatment) prepared from each tight carbonate rock sample from the Middle East field. Figure 1a is one example of the SEM image of the polished surface, and their magnified images from yellow-framed areas in sequence, Figs. 1b to 1d.

This sample was composed of two distinguished zones, an organic matter-rich zone, shown as a darker gray band in the middle of the image, and a calcite-rich zone, which is shown as light gray color in Fig. 1a. The calcite-rich

zone is mainly composed of calcite crystals. The organic matter-rich zone ranges from 400 μm to 500 μm in width. The composition of the organic matter-rich zone could be identified in the magnified images from Figs. 1b to 1d. In this particular sample, the organic matter-rich areas appeared as black stringers in layered structures, and intermixed with calcite, dolomite, pyrite, etc. Nanopore structures within the interior of the organic matter were observed in the higher magnification photomicrograph, Fig. 1d. The intra-organic pore is the dominant pore type.

Figure 2a shows the SEM image and the elemental maps of another representative organic matter-rich zone from the same thin section sample, Figs. 2c to 2e. Figure 2b

Fig. 1 SEM images of the thin section sample prepared from the tight carbonate rock sample from the Middle East field (a), and their sequential magnified images from yellow-framed areas (b) to (d).

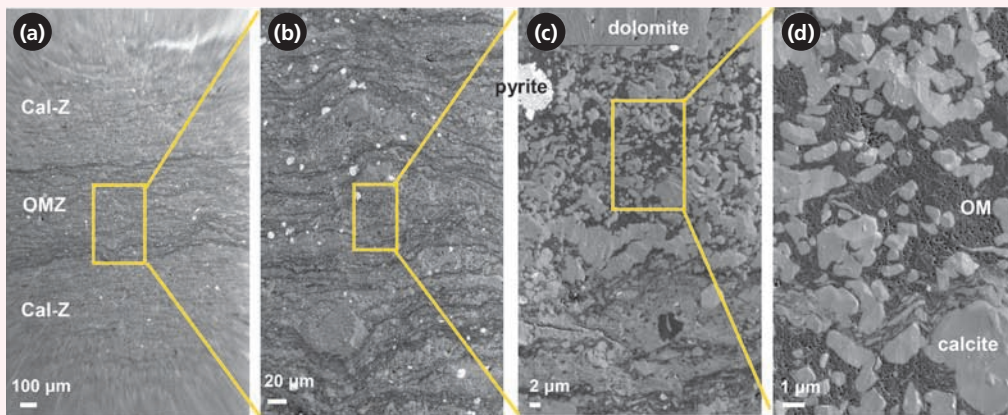
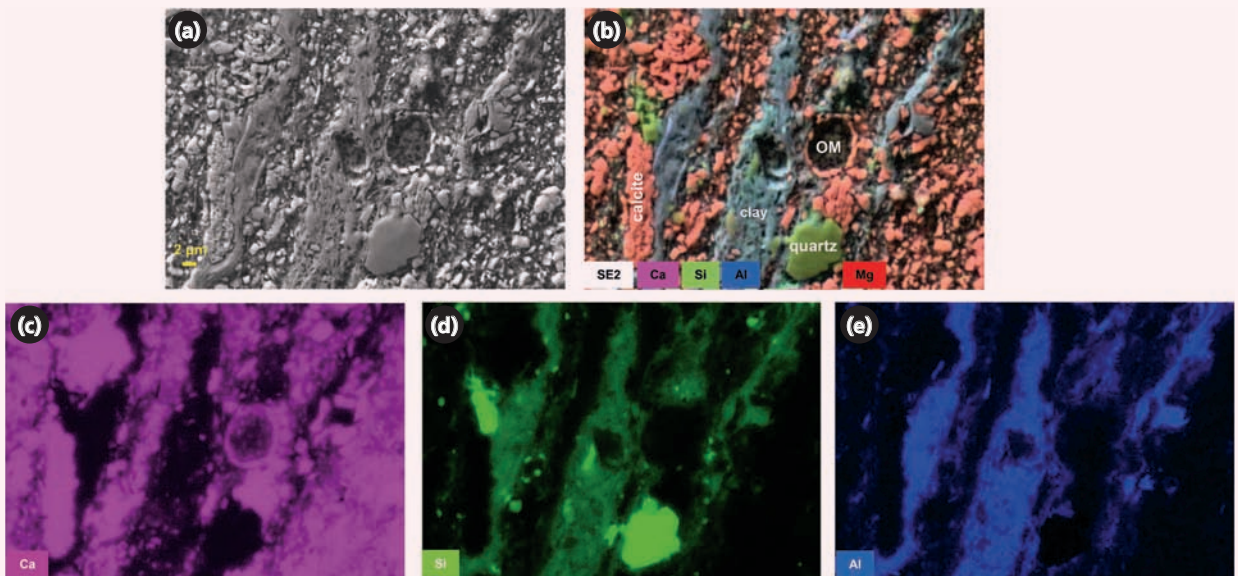


Fig. 2 SEM image and elemental maps from the EDS analysis for the thin section sample prepared from the tight carbonate rock sample from the Middle East field: (a) secondary electron SEM image, (b) pseudo color composite map from EDS analysis, (c) EDS mapping of Ca, (d) EDS mapping of Si, and (e) EDS mapping of Al.



is the pseudocolor composite map, which combines all detectable elements from Ca, silicon, aluminum, Mg, etc. The mineral compositions could be inferred and semi-quantified using the elemental map combination. In this case, Fig. 2b, calcite is shown in an orange color, while quartz is shown in a green color, and clay minerals are in a blue-gray color.

Surface Characterization of the Thin Section Polished Surface after Fluid Treatment. After the SEM microscopic study at the initial condition (as received), the three thin section samples were treated with three different fluids — 2% KCl, 0.5 gpt slick water, and synthetic seawater — for 48 hours at ambient temperature then vacuum dried at 80 °C for 24 hours.

Fluid 1: 2% KCl

Figures 3a and 3b are one pair of SEM images of an area in the organic matter-rich zone before and after 2% KCl treatment, respectively. In Fig. 3a, calcite crystals are shown in a light gray color, while pyrite crystals were shown as bright, nearly circular-shaped crystals. The upper portion of the image has more calcite present while the lower portion was dominated with a stringing featured, organic matter-rich gray area surrounding one euhedral rhomb-shaped dolomite crystal sized roughly $50 \mu\text{m} \times 50 \mu\text{m}$.

In Fig. 3b, the surface of the fluid treated sample was relatively rough, and appeared to be more porous in the calcite-rich zone. Many calcite crystals were dissolved in the 2% KCl solution, leaving cavities on the rock surface. In the lower portion of Fig. 3b, fewer cavities were observed, except that two dolomite crystals were detached from the surface. This is probably due to the fact that there is less calcite present in the lower portion zone, which was dominated by organic matter. No organic matter dissolution was observed in this imaged area.

One more feature associated with the 2% KCl fluid treatment observed in Fig. 3b was the creation and enlargement of microfractures and/or reopening filled fractures. After fluid treatment, a pronounced long fracture across the entire image was seen, Fig. 3b. This fracture was not quite as pronounced in image Fig. 3a, which was before the 2% KCl treatment. This might be due to mineral dissolution from the pre-filled fractures after the fluid treatment. Since the microfracture was in an irregular shape, the apertures of the microfracture in both images were measured at the direction perpendicular to the fracture, and the measurement was conducted at five different points using an image processing tool and then recorded, Table 4. Each individual point n' (1' to 5') in Fig. 3b was the corresponding spot of the point n (1

Fig. 3 SEM images from one organic matter-rich zone of source rock section sample before (a), and after the 2% KCl fluid treatment (b). Many small calcite crystals were dissolved; the euhedral dolomite crystals also have disappeared/dislodged.

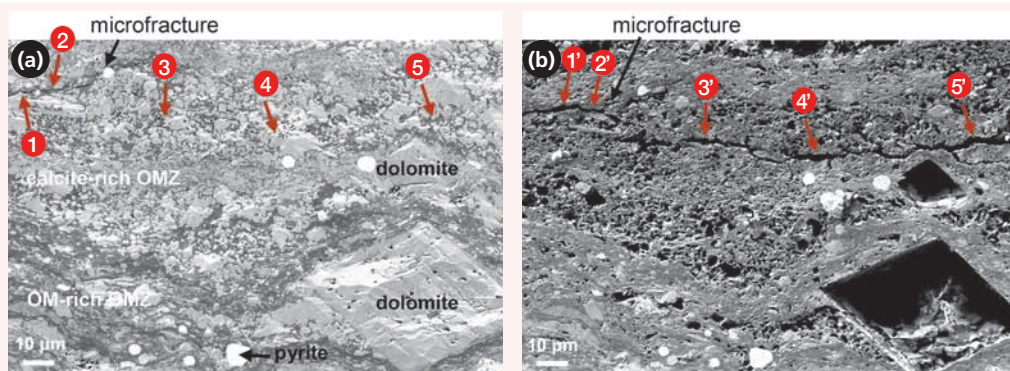


Table 4 The aperture sizes before and after the 2% KCl fluid treatment in Fig. 3.

Before 2% KCl Fluid Treatment		After 2% KCl Fluid Treatment	
#	Aperture (μm)	#	Aperture (μm)
1	0.24	1'	1.64
2	0.22	2'	0.59
3	0 (mineral filled)	3'	1.55
4	0 (mineral filled)	4'	1.93
5	0 (mineral filled)	5'	1.87

to 5) in image Fig. 3a. The apertures in the treated rock sample were measured to be 2 to 7 times larger than the ones in the preexisting microfracture — points 1 and 2. Microfracture across points 3' to 5' in the fluid treated sample was newly created due to the fluid treatment. The aperture of this newly created microfracture was in the range of 1 μm to 2 μm .

Figures 4a and 4b shows a second pair of SEM images on a different location in the organic matter-rich zone before and after 2% KCl treatment, respectively, yet with higher magnification than Figs. 3a and 3b. In this case, one clay-rich layer was located in the center of the organic matter-rich zone with one microfracture across the entire image, Fig. 4a. After the 2% KCl treatment, the calcite dissolution was more pronounced in the calcite-rich zone, while relatively less dissolution was observed in the clay-rich zone, Fig. 4b. The enlargement of the apertures for the preexisting microfracture was also observed after fluid treatment, Table 5. Similar to what was observed in Fig. 3, the apertures in the treated rock sample were measured to be about 2 to 7 times larger than the ones in the preexisting microfracture.

Fluid 2: 0.5 gpt Slick Water

Figures 5a and 5b are two SEM images with low

magnification of one area in the organic matter-rich zone before and after 0.5 gpt slick water treatment, respectively. At the initial condition, Fig. 5a, the sample was tight and pores were not quite visible in the low magnified SEM image with a scale bar of 20 μm . A partially filled fracture was observed in the diagonal direction of the image. After the slick water fluid treatment, the rock surface became more porous as indicated by the appearance of the empty spots, Fig. 5b. The aperture of the microfracture remains in the same range after the slick water fluid treatment, Table 6.

Figures 6a and 6b are another pair of SEM images with higher magnification than Figs. 5a and 5b for a calcite-rich zone before and after slick water treatment, respectively. There was a roughly 8 μm in diameter organic matter-rich mass (porous) shown on the top left side of the image in Fig. 6a, which was surrounded by calcite crystals. After the slick water fluid treatment, it can be seen that some relatively smaller sized calcite crystals — less than 5 μm — disappeared after fluid treatment, Fig. 6b, while the porous organic matter-rich area seemed to remain unchanged. Similar to what was observed in Fig. 5b, the aperture of the microfracture in Fig. 6b remains in the same range after fluid treatment, Table 7.

Fig. 4 SEM images from another organic matter-rich zone of the sample source rock section before (a), and after 2% KCl fluid treatment (b). Small calcite crystals were dissolved.

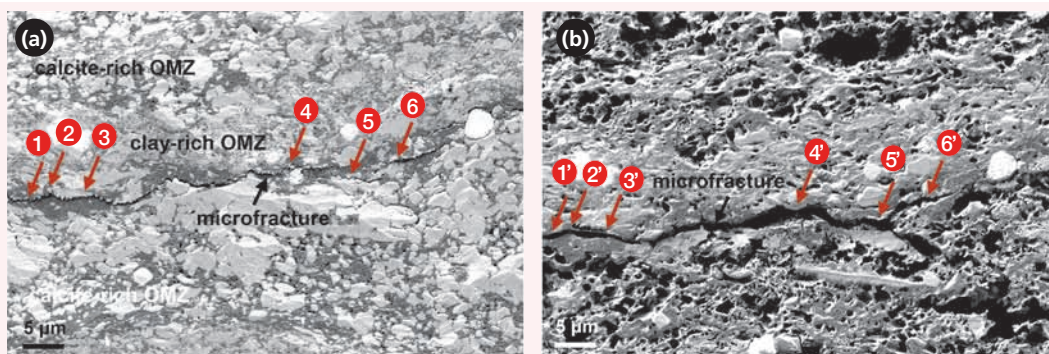


Table 5 The aperture sizes before and after the 2% KCl fluid treatment in Fig. 4.

Before 2% KCl Fluid Treatment		After 2% KCl Fluid Treatment	
#	Aperture (μm)	#	Aperture (μm)
1	0.22	1'	0.68
2	0.23	2'	0.40
3	0.22	3'	0.60
4	0.16	4'	1.39
5	0.13	5'	1.37
6	0.36	6'	0.55

Fig. 5 Low magnification pair of SEM images of the thin section sample before (a), and after 0.5 gpt slick water fluid treatment (b).

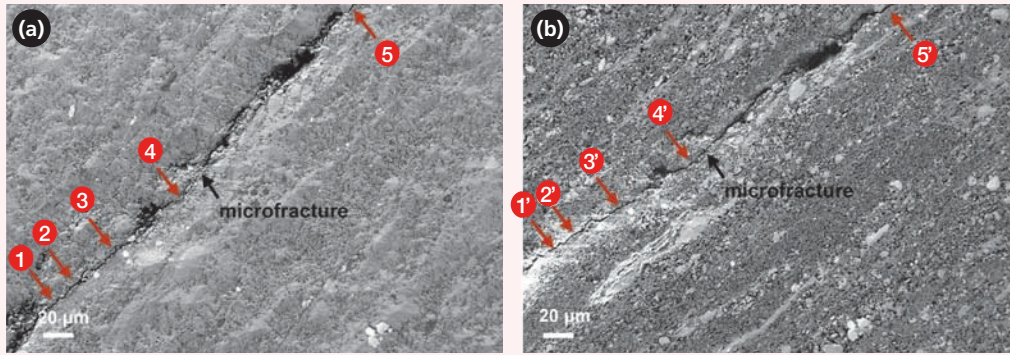
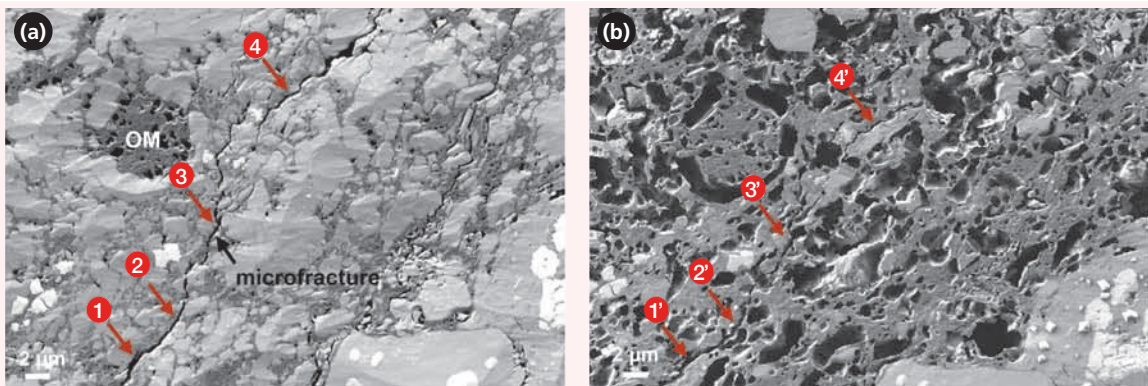


Table 6 The aperture sizes before and after the 0.5 gpt slick water (with 2% KCl) fluid treatment in Fig. 5.

Before Slick Water Fluid Treatment		After Slick Water Fluid Treatment	
#	Aperture (μm)	#	Aperture (μm)
1	1.13	1'	1.04
2	1.43	2'	1.62
3	1.09	3'	1.04
4	0.25	4'	0.44
5	0.72	5'	1.56

Fig. 6 High magnification SEM images of the thin section sample before (a), and after slick water fluid treatment (b).



Figures 7a and 7b are a third pair of high resolution SEM images for an area before and after slick water treatment, respectively. There was an intra-organic pore dominated organic matter mass size ($24 \mu\text{m} \times 6 \mu\text{m}$) located in the middle of the rock sample surface. In this case, besides the dissolution of the calcite crystals as observed in previous examples from Figs. 5 and 6, the dissolution or removal of one piece of the porous

organic matter was also observed.

Fluid 3: Synthetic Seawater

Figures 8a and 8b are one pair of SEM images of an area in the organic matter-rich zone before, and after synthetic seawater treatment, respectively. One open microfracture, which was parallel to the lamination direction, was observed in the as-received sample, Fig. 8a. Different from what was observed in the 2% KCl

and 0.5 gpt slick water fluid treatment samples, the rock surface after seawater fluid treatment does not contain many newly generated empty spots, which indicates that the mineral dissolution is very minimum. Also, the surface of the preexisting microfracture was covered with a significant amount of mineral precipitation.

The same observation of mineral precipitation was also captured in the SEM image of Fig. 9a. To investigate the composition of the mineral precipitates, EDS mapping

of Na, Cl, K, Ca, Mg, S, and O for the imaged area in Fig. 9a were conducted and are shown in Figs. 9b to 9h. As can be seen, the major elements that existed in the mineral precipitates were Na and Cl, which indicates that the precipitates were mainly NaCl.

Figures 10a and 10b are another pair of SEM images of one area from the organic matter-rich zone before and after the synthetic seawater treatment. One mineral filled microfracture and one barren fracture was seen in

Table 7 The aperture sizes before and after 0.5 gpt slick water (with 2% KCl) fluid treatment in Fig. 6.

Before Slick Water Fluid Treatment		After Slick Water Fluid Treatment	
#	Aperture (μm)	#	Aperture (μm)
1	0.49	1'	0.45
2	0.18	2'	0.25
3	0.22	3'	0.32
4	0.16	4'	0.22

Fig. 7 SEM images of the thin section sample before (a), and after slick water fluid treatment (b).

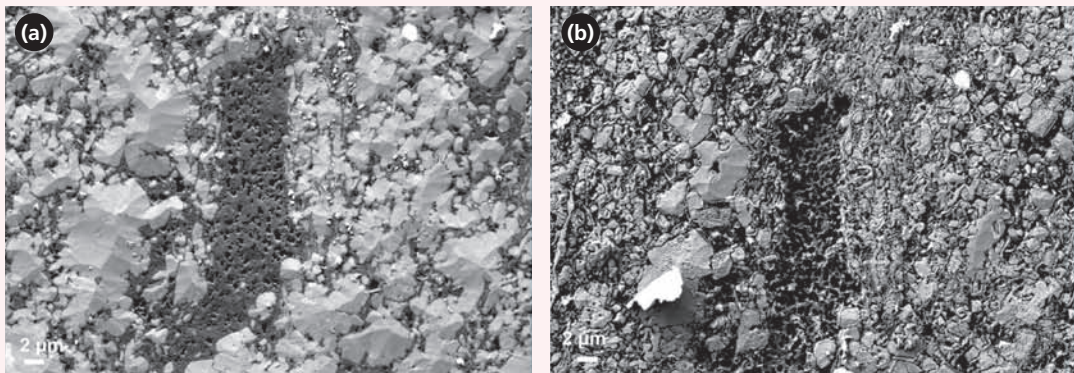


Fig. 8 SEM images of the thin section sample before (a), and after synthetic seawater fluid treatment (b).

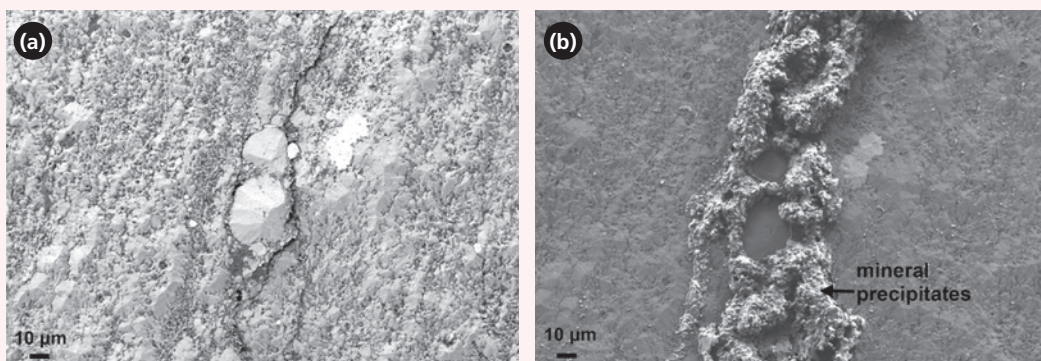
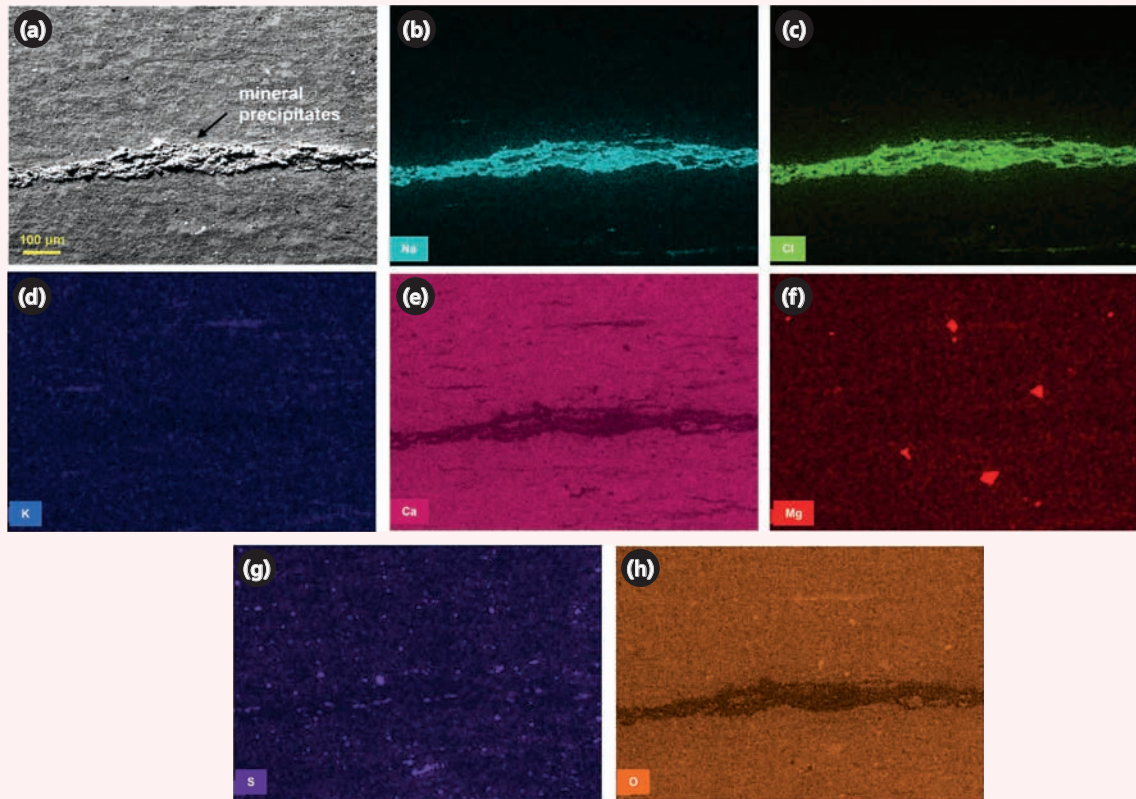


Fig. 9 SEM image and elemental maps from the EDS analysis for one area in the thin section sample after synthetic seawater fluid treatment: (a) secondary electron SEM image, (b) EDS mapping of Na, (c) EDS mapping of Cl, (d) EDS mapping of K, (e) EDS mapping of Ca, (f) EDS mapping of Mg, (g) EDS mapping of S, and (h) EDS mapping of O.



the yellow framed area in Fig. 10a, and was magnified in Fig. 10c. The tightly packed tubular-shaped crystal assets inside the filled microfracture (cross Point 1-3) were mainly gypsum minerals. After synthetic seawater fluid treatment, the filled gypsum inside the microfracture were dissolved and left an open microfracture (cross Point 1'-3'), Fig. 10d.

The aperture of this re-opened microfracture was changed from 0 μm (filled with minerals) to 0.2 μm , while the aperture of the adjacent barren fracture (across points 4-6) was slightly decreased, Table 8. Similar to what was observed in Figs. 8a and 8b, the rock surface after seawater fluid treatment does not contain much newly generated empty spots, indicating that the calcite dissolution is very minimum. A slight mineral precipitation was observed on the rock surface as well.

Identification and Quantification of Dissolved Ions. Since the major minerals from the Middle East field were calcite and dolomite, Table 1, the expected major changes of the ions in the treatment fluids were Ca^{2+} , and Mg^{2+} along with other commonly observed cations in carbonate rocks, such as Sr^{2+} . The concentrations of these three cation ions for the original fluids and the fluids after treatment were analyzed by ICP-OES. Then, the changes of these three cations for all three fluids after rock treatment were normalized as μg dissolution

per gram of rock sample for a better comparison, Table 9. The pH of the 2% KCl and slick water fluid after treatment were slightly increased, which was caused by the dissolution of calcite minerals.

Flow Characteristics Assessment. Table 10 shows the absolute permeability measurement under different effective stresses for three Eagle Ford outcrop core plugs before and after fluid treatment. Data has been plotted in Fig. 11 as well. As can be seen, the absolute permeability under different stress conditions has been significantly enhanced after fluid treatment.

Discussion

Three aqueous-based fluids were selected in this study to investigate the interactions between the fluids and the tight organic-rich carbonate source rocks. Fluid 1 was 2 wt% KCl (pH = 7.1), which does not contain any polymers. Fluid 2 was a solution of 0.5 gpt slick water. This fluid was selected because of the common practice of using slick water fracturing in stimulating the unconventional fields. Fluid 3 was the synthetic seawater. The reason for selecting seawater as one of the fluids in this study was because seawater has been considered as a preferred base fluid for making fracturing fluid for offshore stimulation jobs, or in some areas where there is a freshwater shortage issue.

Consequently, there are some other concerns of using seawater as a fracturing fluid because of the potential negative impact to the reservoir formation such as mineral precipitation, corrosion, and scale formation. A comprehensive study on the impact of seawater to the formation from microscopic imaging and a flow characteristic standpoint is needed.

Surface Morphology Changes after Fluids Treatment. From the mineralogy analysis previously listed in Table 1, the main minerals existing in the Middle

East sample were calcite, dolomite, quartz, and minor amounts of pyrite, kaolinite, and illitic clay. Among these minerals, calcite has the highest solubility in water.

Consistently, calcite dissolution on the rock surface has been observed in all three treatment fluids, while the phenomena varies to some extent according to the amount of the newly generated voids on the rock surface for the fluids' treated rock sample. A significant amount of calcite dissolution was observed for the 2% KCl and the 0.5 gpt slick water fluids' treated samples; much more

Fig. 10 SEM images of the thin section sample before (a), and after synthetic seawater fluid treatment (b); (c) the magnified area from the yellow framed region in (a), and (d) the magnified area from the yellow framed region in (b).

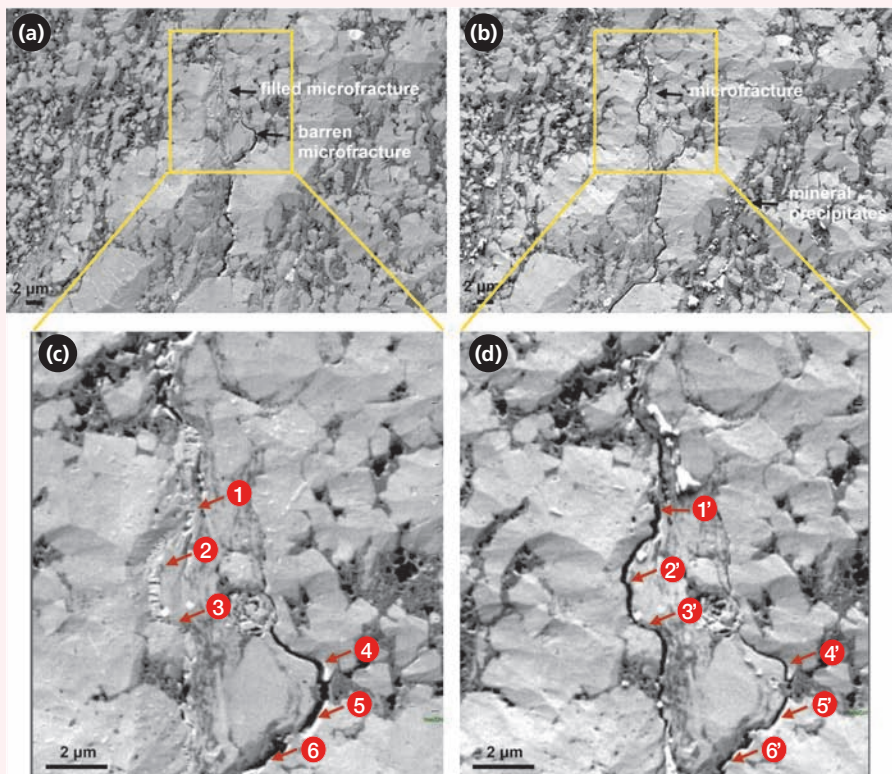


Table 8 The aperture sizes before and after synthetic seawater treatment in Fig. 10.

Before Slick Water Fluid Treatment		After Slick Water Fluid Treatment	
#	Aperture (µm)	#	Aperture (µm)
1	0 (mineral filled)	1'	0.29
2	0 (mineral filled)	2'	0.24
3	0 (mineral filled)	3'	0.19
4	0.29	4'	0.18
5	0.34	5'	0.20
6	0.30	6'	0.24

Table 9 The cation dissolution in treatment fluids (normalized as μg dissolution per gram of rock) and changes of pH values.

		Cations Dissolution ($\mu\text{g}/\text{g}$ of rock)		
		2% KCl	0.5 gpt Slick Water	Synthetic Seawater
Elements	Mg ²⁺	35.8	34.2	0.0
	Ca ²⁺	700.9	522.7	111.2
	Sr ²⁺	13.6	11.6	9.6
pH	Initial	7.1	7.0	8.0
	After treatment	7.3	8.1	8.0

Table 10 The absolute permeability measurement for three Eagle Ford outcrop core plugs before and after fluid treatment.

Treatment Fluid	Effective Stress (psi)	Absolute Permeability (md)		Permeability Improvement (Treated/Initial)
		Before Fluid Treatment (Initial)	After Fluid Treatment (Treated)	
2% KCl	500	0.024	0.923	38
	1,000	0.02	0.773	39
	2,000	0.019	0.502	26
Slick Water	500	0.016	0.363	23
	1,000	0.012	0.276	23
	2,000	0.01	0.21	21
Synthetic Seawater	500	0.195	2.306	12
	1,000	0.159	1.48	9
	2,000	0.122	0.731	6

than the synthetic seawater treated sample, which might be due to the fact that the synthetic seawater contains relatively high concentrations of Ca²⁺ and Mg²⁺, which causes the solubility of calcite to decrease. Smaller sized calcite crystals — less than 5 μm — tends to dissolve faster than relatively larger sized calcite or dolomite particles — larger than 5 μm . For the larger sized calcite particles, the dissolution started from the edge and the surface of the particles. Dissolution or dislocation of dolomite was also observed in the 2% KCl fluid treated rock sample, Fig. 3.

In general, other minerals such as quartz, and a majority of organic matter, remain undissolved in all three aqueous-based fluids, however, interestingly, dissolution or dislocation of a piece of porous organic matter was observed in the slick water fluid treatment, Fig. 7. This might be due to the additional chemical components that exists in the slick water fluids, because it was prepared with an emulsion-based polymeric material, and the emulsion contains additional base oil and surfactants.

The ICP analysis for fluids after rock treatment further confirms the observation of the mineral dissolution phenomenon from the surface morphology studies. It also quantifies the dissolution power difference among these three fluids. As can be seen from Table 9, the change of Ca²⁺ dissolution was higher in the 2% KCl than it was in the slick water treatment fluid. Around 700.9 μg of Ca²⁺ per gram of rock was dissolved in the 2% KCl, and around 522.7 μg of Ca²⁺ per gram of rock was dissolved in the 0.5 gpt slick water treatment fluids. Around 35 μg of Mg²⁺ per gram of rock was dissolved in these two fluids. The ion concentration increase in Ca²⁺ and Mg²⁺ confirms the calcite and dolomite crystals dissolution. The dissolution of calcite in seawater was lower than in the 2% KCl and slick water, which is also consistent with our observation from the surface morphology study. Small increases — less than 14 μg per gram of rock — of Sr²⁺ were also observed in all three treatment fluids as well. Minor or trace amounts of strontium carbonate or sulfate occurs quite often with other diagenetic minerals

in the evaporate suite of rocks.

Besides the mineral dissolution phenomenon, mineral precipitation was noticed in the seawater treated samples, Figs. 8 to 10. Precipitation was identified to be mainly NaCl based on the EDS mapping. The precipitation might be due to the evaporation in the lab environment, which may or may not happen under downhole conditions since the precipitation mainly happens after the fluid was over-saturated.

Aperture Changes for Microfractures after Fluids Treatment. As mentioned earlier, the rock samples used in this study were prepared with extra caution to minimize the damage to the rock sample, however, there was no guarantee that there was no induced damage to the prepared sample. Even some of the microfractures — especially the barren fractures — may be induced during the sample preparation steps. The studies on the aperture changes of microfractures with fluid treatment are still worthwhile since during or after hydraulic fracturing — especially the slick water treatment — numerous microfractures could be generated.

It is important to have accurate aperture measurements for the microfractures for this study. Ortega et al. (2006)¹⁶ introduced a logarithmically graduated comparator along with a hand lens, which allows us to measure the fracture apertures as small as approximately 0.05 mm. The aperture sizes captured in our study were mainly below 2 μm . An imaging processing tool was used to measure the aperture size. Also, since the microfractures observed were mainly in irregular shapes, aperture measurements for multiple points were conducted to achieve a relatively fair comparison.

As noticed from the treatment study of all three fluids, significant calcite dissolution was observed for both the 2% KCl and the 0.5 gpt slick water fluid treatments.

The aperture size of the existing barren microfractures for the 2% KCl were enhanced by approximately 2 to 7 times, while with the 0.5 gpt slick water fluid treated rocks, the microfractures remain in a similar range. The generation of new microfractures was also captured in the 2% KCl fluid treatment. Similar to the slick water treatment, the synthetic seawater treatment does not change the aperture size for barren microfractures much either. Consequently, the dissolution of gypsum in sealed microfractures was also captured in the synthetic seawater treated rock sample.

The generation of new microfractures or re-opening of the sealed fractures will largely increase the porosity. If newly generated fractures were interconnected with the existing porosities, the permeability for the rock sample will increase accordingly. The enlargement of the existing microfractures is expected to contribute to the permeability increase as well.

Changes in Flow Characteristics. The absolute permeability increase indicated in Fig. 11 after fluid-rock interaction under different stress conditions is aligned with our expectation that the mineral dissolution, generating new microfractures or the re-opening of sealed fractures could result in the permeability increase. As noticed in Table 10, the 2% KCl fluid treatment causes the increase of permeability about 35 times under our testing conditions. Figure 11 also indicates that the change/increase in the absolute permeability resulted from mineral dissolution, and enlargement of the microfractures becomes more sensitive to the stress. The stress sensitivity is characterized by the slope of permeability vs. effective stress curves, Fig. 12. In the case of the 2% KCl fluid treatment, the permeability after the 2% KCl treatment has a sensitivity factor of 4×10^{-4} (psi^{-1}), whereas the permeability before the 2% KCl treatment shows a sensitivity factor of 1×10^{-4} (psi^{-1}).

Fig. 11 The absolute permeability measurement under different effective stresses for three Eagle Ford outcrop core plugs before and after fluid treatment.

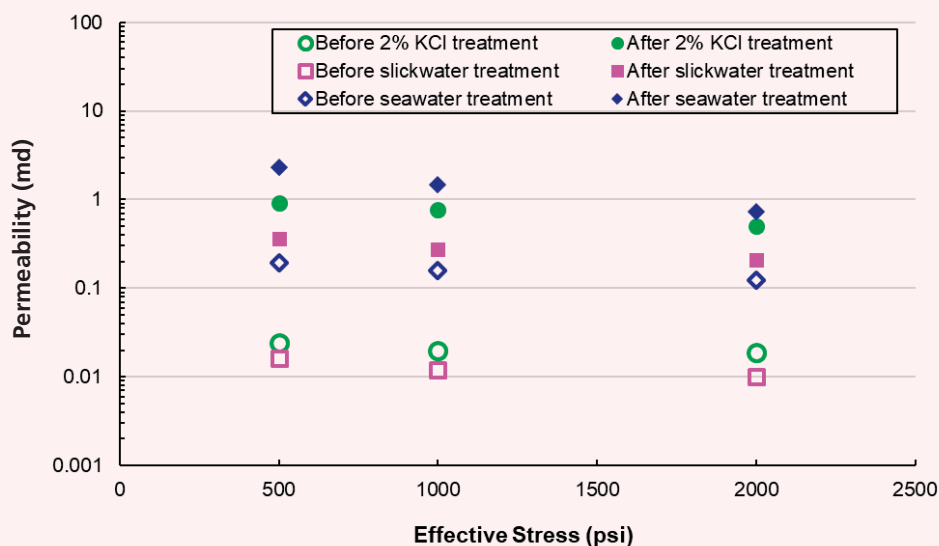
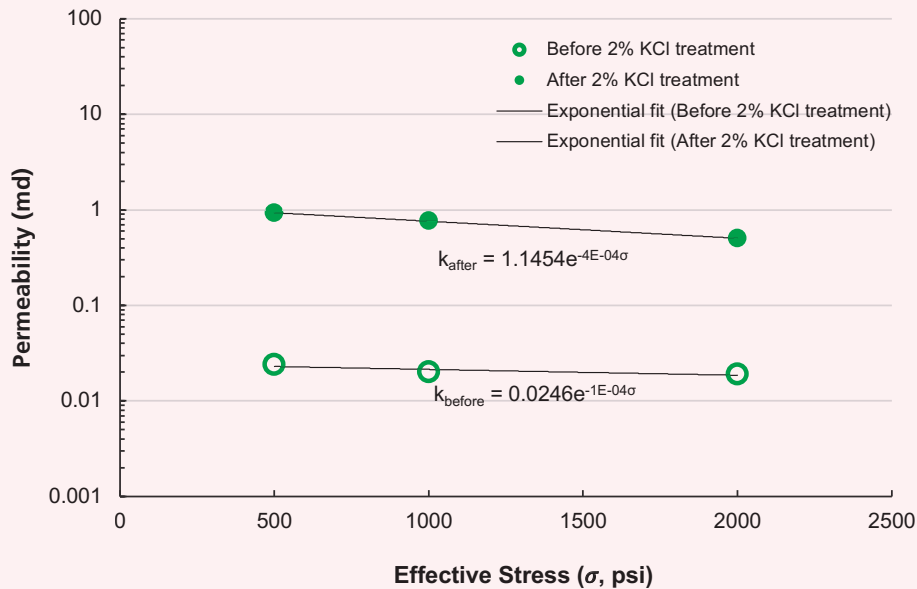


Fig. 12 The absolute permeability measurement (k) under different effective stress (σ) for the Eagle Ford outcrop core plugs before and after the 2% KCl fluid treatment, with stress sensitivity factors of permeability calculated from measurements.



The sensitivity factor corresponds to the slope of a curve in Fig. 12. The fluid treatment increases the sensitivity by four times in this case.

This observed stress sensitivity is consistent with the fact that the permeability of open/barren microfractures are alike, rather than sealed/cemented microfractures¹⁷, which are relatively stress sensitive¹⁸. We need to emphasize that the observed absolute permeability enhancement considerably depends on test conditions, e.g., rock and fluid chemical compositions, temperature, fluid pressures, volumetric solid-fluid ratio and others, while the test conditions for this work has been carefully documented. Therefore, caution should be taken when applying the observed values for permeability enhancement to different conditions.

Conclusions

A significant amount of fracturing fluids remains in the unconventional formations after the flow back. The impacts of the remaining fluids on hydrocarbon production are not fully understood. They are likely reservoir specific and depend on the reservoir conditions. This study attacked this issue for the carbonate source rocks through laboratory investigations on the microscopic scale. The SEM and EDS results for the fluid treated source rock samples show that: (1) Significant calcite dissolution has been observed in the 2% KCl and the slick water fluid treated samples; (2) In the 2% KCl and the slick water fluid, re-opening of some mineral filled natural fractures was observed; (3) The enlargement of microfractures was slightly more noticeable for samples treated with 2% KCl (2 to 7 times) in comparison to the slick water at the micron-scale level; (4) In one sample, dissolution of organic matters was captured in the

slick water fluid treated rock sample; (5) Some NaCl precipitation and new microfractures generation were observed for samples treated with seawater.

The ICP test results confirmed that a significant amount of calcite has been dissolved after the treatment of all three fluids since the concentration of Ca^{2+} of the treatment fluids increased significantly. The absolute permeability increases significantly after 72 hours when treated in the 2% KCl and the slick water fluid treatment, unlike the synthetic seawater treatment. While more studies are needed under different test conditions, this study provides experimental evidence that aqueous-based fracturing fluid may potentially have a positive effect on gas production from organic-rich carbonate source rock. This observation will be beneficial to the future usage of freshwater and seawater-based fluids in stimulating gas production for organic-rich carbonate formations.

Acknowledgments

The authors would like to thank the management of Aramco Services Company in Houston for their support and permission to publish this article. The authors would also like to thank Brent Cooper for the ICP analysis.

This article was presented at the SPE Kingdom of Saudi Arabia Annual Technical Symposium and Exhibition, Dammam, Saudi Arabia, April 23-26, 2018.

References

- O'Brien, P., Onyia, D. and Astarita, G.: "Middle East Bucking the Trend in Drive for New EOR Technology," *Exploration & Production*, August 2015, <https://www.epmag.com/middle-east-bucking-trend-drive-new-eor-technology-812011>.
- McLeod, H.O.: "Matrix Acidizing," *Journal of Petroleum Technology*, Vol. 36, Issue 12, December 1984, pp. 2055-2069.

3. Cash, R., Zhu, D. and Hill, A.D.: "Acid Fracturing Carbonate-Rich Shale: A Feasibility Investigation of Eagle Ford Formation," SPE paper 181805, presented at the SPE Asia Pacific Hydraulic Fracturing Conference, Beijing, China, August 24-26, 2016.
4. Wu, W. and Sharma, M.M.: "Acid Fracturing in Shales: Effect of Dilute Acid on Properties and Pore Structure of Shale," *SPE Production & Operations*, Vol. 32, Issue 1, February 2017, pp. 51-63.
5. Strand, S., Høgenesen, E.J. and Austad, T.: "Wettability Alteration of Carbonates — Effects of Potential Determining Ions (Ca^{2+} and SO_4^{2-}) and Temperature," *Colloids and Surfaces A: Physicochemical and Engineering Aspects*, Vol. 275, Issues 1-3, March 2006, pp. 1-10.
6. Zhang, P. and Austad, T.: "Wettability and Oil Recovery from Carbonates: Effects of Temperature and Potential Determining Ions," *Colloids and Surfaces A: Physicochemical and Engineering Aspects*, Vol. 279, Issues 1-3, May 2006, pp. 179-187.
7. Hiorth, A., Cathles, L.M. and Madland, M.V.: "The Impact of Pore Water Chemistry on Carbonate Surface Charge and Oil Wettability," *Transport in Porous Media*, Vol. 85, Issue 1, October 2010, pp. 1-21.
8. Yousef, A.A., Al-Saleh, S., Al-Kaabi, A.U. and Al-Jawfi, M.S.: "Laboratory Investigation of Novel Oil Recovery Method for Carbonate Reservoirs," SPE paper 137634, presented at the Canadian Unconventional Resources and International Petroleum Conference, Calgary, Alberta, Canada, October 19-21, 2010.
9. Ross, G.D., Todd, A.C., Tweedie, J.A. and Will, A.G.S.: "The Dissolution Effects of CO_2 -Brine Systems on the Permeability of U.K. and North Sea Calcareous Sandstones," SPE paper 10685, presented at the SPE Enhanced Oil Recovery Symposium, Tulsa, Oklahoma, April 4-7, 1982.
10. Akrad, O.M., Miskimins, J.L. and Prasad, M.: "The Effects of Fracturing Fluids on Shale Rock Mechanical Properties and Proppant Embedment," SPE paper 146658, presented at the SPE Annual Technical Conference and Exhibition, Denver, Colorado, October 30-November 2, 2011.
11. Lai, B., Liang, F., Zhang, J., Li, L., et al.: "Fracturing Fluids Effects on Mechanical Properties of Organic Rich Shale," ARMA paper 2016-180, presented at the 50th U.S. Rock Mechanics/Geomechanics Symposium, Houston, Texas, June 26-29, 2016.
12. Anders, M.H., Laubach, S.E. and Scholz, C.H.: "Microfractures: A Review," *Journal of Structural Geology*, Vol. 69, Part B, December 2014, pp. 377-394.
13. Gale, J.F.W., Laubach, S.E., Olson, J.E., Eichhubl, P., et al.: "Natural Fractures in Shale: A Review and New Observations," *AAPG Bulletin*, Vol. 98, Issue 11, November 2014, pp. 2165-2216.
14. Liang, F., Lai, B., Zhang, J., Liu, H.-H., et al.: "An Experimental Study on Interactions between Imbibed Fracturing Fluid and Organic-Rich Tight Carbonate Source Rocks," SPE paper 188338, presented at the Abu Dhabi International Petroleum Exhibition and Conference, Abu Dhabi, UAE, November 13-16, 2017.
15. Jones, S.C.: "A Technique for Faster Pulse-Decay Permeability Measurements in Tight Rocks," *SPE Formation Evaluation*, Vol. 12, Issue 1, March 1997, pp. 19-26.
16. Ortega, O.J., Marrett, R.A. and Laubach, S.E.: "A Scale-Independent Approach to Fracture Intensity and Average Spacing Measurement," *AAPG Bulletin*, Vol. 90, Issue 2, February 2006, pp. 193-208.
17. Laubach, S.E., Olson, J.E. and Gale, J.F.W.: "Are Open Fractures Necessarily Aligned with Maximum Horizontal Stress?" *Earth and Planetary Science Letters*, Vol. 222, Issue 1, May 2004, pp. 191-195.
18. Khan, M. and Teufel, L.W.: "The Effect of Geological and Geomechanical Parameters on Reservoir Stress Path and Its Importance in Studying Permeability Anisotropy," *SPE Reservoir Evaluation & Engineering*, Vol. 3, Issue 5, October 2000, pp. 394-400.

About the Authors

Dr. Feng Liang

*Ph.D. in Organic Chemistry,
Rice University*

Dr. Feng Liang is currently a Research Science Specialist at the Aramco Services Company, Aramco Research Center-Houston. She has now been with the company for over five years.

Prior to joining the Aramco Research Center, Feng was a Principal Scientist at Halliburton for nearly eight years. Her research interests are the new materials and product development in fracturing fluid, advanced fluid additives, waterless fracturing technologies, bio-degradable diversion materials, sand control products, cement additives and nanomaterials reinforced elastomers.

Feng is a contributor to many patents and technical papers. She holds 38 issued U.S. patents and 30 additional published patent applications. Feng is the author and coauthor of more than 60 technical papers,

with a few in very high impact factor journals such as the *Journal of the American Chemical Society* and also *Nano Letters*. She has also coauthored two book chapters as well. Feng's publications have received over 3,000 citations.

She is a member of the Society of Petroleum Engineers (SPE) and the American Chemical Society (ACS). Feng received the 2017 SPE Production and Operations Award for the Gulf Coast North American Region. She also received the 2017 Effective Publication Award from Saudi Aramco's Exploration and Petroleum Engineering Center – Advanced Research Center (EXPEC ARC).

Feng received her Ph.D. degree in Organic Chemistry from Rice University, Houston, TX.

Jilin Zhang

*M.S. in Geology,
University of Houston*

Jilin Zhang joined the Aramco Services Company, Aramco Research Center-Houston, in 2013 as a Petroleum Engineer.

Prior to this, he was a Petrophysical Consultant at Formation and Reservoir Services of Halliburton; a Petrophysicist/Senior Geoscientist at Baker Hughes, a Manager of Geology with Ellington & Associates, an X-ray Powder Diffraction Petrographer with OMNI Labs, and also held several positions in China from

1985 to 1994.

Jilin received his M.S. degree in Geology from the University of Houston, Houston, TX, majoring in carbonate petrography and diagenesis. He also received an M.S. degree in Marine Geology from the Ocean University of China, Qingdao, China, focusing on modern sedimentation of clastic rocks.

Jilin's expertise is in mineralogy in general, and petrophysics in shale and carbonate rocks.

Dr. Hui-Hai Liu

*Ph.D. in Soil Physics,
Auburn University*

Dr. Hui-Hai Liu is a Senior Petroleum Engineering Consultant at the Aramco Research Center in Houston. Before joining Aramco in 2014, he was a Staff Scientist and the Head of the Hydrogeology and Reservoir Dynamics Department at Lawrence Berkeley National Laboratory (LBNL) and an Adjunct Distinguished Professor at the China University of Mining and Technology in Beijing.

Hui-Hai has more than 25 years of experience in developing models for subsurface fluid flow and coupled hydromechanical processes, and in applying them to shale gas recovery, carbon dioxide geological sequestration, enhanced coalbed methane recovery, geological disposal of high-level nuclear waste, and groundwater flow and transport. Since joining Aramco, he has focused on research activities related to reservoir property measurement and production

prediction for unconventional reservoirs.

Hui-Hai's work has been documented in one book, more than 130 peer-reviewed journal articles, and numerous patents. He has received several awards for his research and achievements, including the Society of Petroleum Engineers (SPE) Distinguished Membership, the LBNL Director's Award for Exceptional Achievement, Fellowship of the Geological Society of America, and the Emil Truog Research Award from the Soil Science Society of America.

Hui-Hai received his B.S. in Mechanical Engineering from Beijing Agricultural Engineering University, Beijing, China, his M.S. degree in Applied Fluid Mechanics from Huazhong University of Science and Technology, Wuhan, China, and a Ph.D. degree in Soil Physics (Multiphase Flow in Porous Media) from Auburn University, Auburn, AL.

Kirk M. Bartko

*B.S. in Petroleum Engineering,
University of Wyoming*

Kirk M. Bartko was a Senior Petroleum Engineering Consultant with Saudi Aramco's Well Completion Operations & Production Engineering Department, where he was in the Technical Support Unit on stimulation and completion development for unconventional gas operations prior to his recent retirement.

Kirk joined Saudi Aramco in 2000, where he worked to support hydraulic fracturing and completion technologies across all Saudi Arabia operations. Kirk's experience includes 19 years with ARCO with various

global assignments in locations including Texas, Alaska, Algeria, and the Research Technology Center supporting U.S. and international operations.

He has authored and coauthored more than 50 technical papers on well stimulation and is a recipient of four U.S. granted patents. Kirk has been actively involved in the Society of Petroleum Engineers (SPE) since 1977.

He received his B.S. degree in Petroleum Engineering from the University of Wyoming, Laramie, WY.

Got an article you would like to publish? Here are our guidelines.

These guidelines are designed to simplify and help standardize submissions. They need not be followed rigorously. If you have any questions, please call us.

Length

Average of 2,500-4,000 words, plus illustrations/photos and captions. Maximum length should be 5,000 words. Articles in excess will be shortened.

What to send

Send text in Microsoft Word format via email plus one hard copy. Send illustrations/photos and captions separately but concurrently, both as email and as hard-copy (see file format section for more information).

Procedure

Notification of acceptance is usually within three weeks after the submission deadline. The article will be edited for style and clarity and returned to the author for review. All articles are subject to the company's normal review. No paper can be published without a signature at the manager level or above.

Format

No single article need include all of the following parts. The type of article and subject covered will determine which parts to include.

Working Title

Lorem Ipsum here.

Abstract

Usually 150-300 words to summarize the main points.

Introduction

Different from the abstract in that it sets the stage for the content of the article, rather than telling the reader what it is about.

Main body

May incorporate subtitles, artwork, photos, etc.

Conclusion/Summary

Assessment of results or restatement of points in introduction.

Endnotes/References/Bibliography

Use only when essential. Use author/date citation method in the main body. Numbered footnotes or endnotes will be converted. Include complete publication information. Standard is *The Associated Press Stylebook*, 52nd ed. and *Webster's New World College Dictionary*, 5th ed.

Acknowledgments

Use to thank those who helped make the article possible.

Illustration/Tables/Photos and explanatory text

Submit these separately. Do not place in text. Positioning in the text may be indicated with placeholders. Initial submission may include copies of originals; however, publication will require the originals. When possible, submit both electronic versions and printouts. Color is preferable.

File Format

Illustration files with .EPS extensions work best. Other acceptable extensions are .TIFF/.JPEG/.PICT.

Permission(s) to reprint, if appropriate

Previously published articles are acceptable but can be published only with written permission from the copyright holder.

Author(s)/Contributor(s)

Please include a brief biographical statement.

Submission/Acceptance Procedures

Papers are submitted on a competitive basis and are evaluated by an editorial review board comprised of various department managers and subject matter experts. Following initial selection, authors whose papers have been accepted for publication will be notified by email.

Papers submitted for a particular issue but not accepted for that issue may be carried forward as submissions for subsequent issues, unless the author specifically requests in writing that there be no further consideration.

Submit articles to:

Editor
The Saudi Aramco Journal of Technology
C-11B, Room AN-1080
North Admin Building #175
Dhahran 31311, Saudi Arabia
Tel: +966-013-876-0498
Email: william.bradshaw.1@aramco.com.sa

Submission deadlines

Issue	Paper submission deadline	Release date
Spring 2020	November 12, 2019	March 31, 2020
Summer 2020	February 11, 2020	June 30, 2020
Fall 2020	May 12, 2020	September 30, 2020
Winter 2020	August 13, 2020	December 31, 2020

There is more.

A New Approach to Measure the Wettability of Porous Media under Different Saturation Conditions by Temperature Sensitivity of Nuclear Magnetic Resonance Relaxation Time

Dr. Hyung T. Kwak, Jun Gao, and Dr. Ahmad M. Al-Harbi

Abstract / The wettability — specifically the wettability of the porous structure within rocks — is one of the key parameters that determine fluid flow, which determines the potential oil producibility from reservoirs. The oil wetting preference on the pore surface of reservoir rock influences the reservoir performance in various steps of oil production, such as waterflooding and enhanced oil recovery.

Unleash Unconventional Resources with the Power of Light-Laser Technology

Dr. Sameeh I. Batarseh, Abdullah M. Al-Harith, Dr. Haitham A. Othman, and Dr. Hameed H. Al-Badairy

Abstract / The objective of this work is to establish communications between the tight hydrocarbon-bearing formation and the wellbore by using high power laser technology. This article presents different methods of utilizing the energy of the laser to enhance and improve the flow in unconventional reservoirs, including tight formations. The successful results are used for field deployment strategy.

New Understanding on Calcium Carbonate Scaling Kinetics

Dr. Qiwei Wang, Faez H. Al-Dawood, and Dr. Tao Chen

Abstract / Calcium carbonate (CaCO_3) is the predominate type of mineral scale formed in many industrial water processes, including oil and gas production. Comprehensive and accurate knowledge on the CaCO_3 scaling mechanism is critical for effective scale management. Extensive studies have been carried out on CaCO_3 formation process and prevention under various conditions of temperature, saturation state, pH, and additives. The effect of pressure is considered in scaling tendency calculation, but its potential impact on scaling kinetics has been neglected.

Wettability and Residual Oil Effects on Polymer Retention Estimates

Dr. Jinxun Wang and Dr. Abdulkarim M. Al-Sofi

Abstract / Polymer flooding is one of the most mature enhanced oil recovery methods. In such projects, polymer consumption — a requirement — depends heavily on polymer retention. Retention is commonly measured through single-phase displacement experiments. Often, clean cores, i.e., not preserved nor restored, are used in such experiments. Recent studies in sandstones suggest that neglecting residual oil affects the polymer retention estimates, which are substantially exaggerated. Moreover, the effects of wettability on retention estimates have not been addressed.



Aramco
Journal
of Technology

Liked this issue? Sign up. It's free.

To begin receiving the *Aramco Journal of Technology* please complete this form, scan and send by email to **william.bradshaw.1@aramco.com**.

Got questions?

Just give us a call at +966-013-876-0498 and we'll be happy to help!



Scan the QR code to go straight to your email and attach the form!

Subscription Form

Name

Title

Organization

Address

City

State/Province

Postal code

Country

Email address

Number of copies

